UNIVERSITÉ DE SHERBROOKE
Faculté de génie
Département de génie chimique et de génie biotechnologique

MODÈLES FORTEMENT COUPLÉS POUR LA PRÉDICTION DES PERFORMANCES DES RÉACTEURS ÉLECTROCHIMIQUES

STRONGLY COUPLED MODELS FOR THE PREDICTION OF ELECTROCHEMICAL REACTORS PERFORMANCES

Thèse de doctorat
Specialité : génie chimique

Giuliana LITRICO

Jury: Prof. Pierre PROULX (directeur)
Prof. Martin Désilets
Prof. Gessie Brisard
Prof. Sébastien Poncet
Dr. Ing. Gaetan Lantagne

Sherbrooke (Québec) Canada Décembre 2017

A te Luca,
che sei la parte migliore di me.

RÉSUMÉ

La modélisation mathématique des systèmes électrochimiques, et en général la modélisation des systèmes fluidiques réactifs en présence de champs électriques, est un problème d'une complexité telle que des solutions analytiques n'existent que dans des cas très simplifiés et la solution numérique est, malgré toute la puissance de calcul moderne, encore très difficile. À ce jour, les avancées dans la modélisation au niveau des modèles d'écoulement sont majeures, mais la modélisation couplée de l'écoulement, avec le champ électrique en présence de solutions concentrées demeure encore un défi de taille. Le couplage des différents champs décrits par les modèles mathématiques devient critique dans les régions où ont lieu les réactions hétérogènes aux interfaces chargées modélisées par l'équation non linéaire de Butler-Volmer.

Les logiciels commerciaux modernes commencent à permettre de coupler les modules d'électrochimie avec la mécanique des fluides numérique (CFD), mais l' impossibilité d'accéder au code source ne permet pas au chercheur de modifier à volonté la formulation des modèles. Par conséquent, le projet de recherche actuel vise le développement d'une plate-forme logicielle ouverte (open-source) comme OpenFOAM, qui peut garantir une complète accessibilité au code-source, la liberté des utilisateurs à faire des modifications, la transparence des détails des modèles, et tous les autres développements qui sont requis pour chaque problème rencontré par les chercheurs.

Le développement de modèles reposant sur des lois physiques établies permettra la modélisation des systèmes électrochimiques complexes, et la compréhension des phénomènes qui s'y déroulent. Il vise la modélisation du transfert de masse d'une cellule où l'écoulement de la solution concentrée (molten salt) est turbulent, biphasique et incompressible, et les réactions électrochimiques de surface sont calculées en utilisant une distribution tertiaire de densité de courant. Le principal enjeu sur le plan scientifique, dans le cadre de ce projet, demeure donc de développer un modèle qui soit bien calé sur le problème technologique visé afin qu'il puisse reproduire de façon réaliste les systèmes électrochimiques. Il vise également à amener la modélisation à un point où l'outil pourra être utilisé comme instrument de prédiction et de validation de nouveaux concepts des systèmes électrochimiques.

Mots-clés : Réacteur électrochimique, Couplage, Butler-Volmer, Distribution de courant tertiaire, Turbulence, Flux biphasé , OpenFOAM

ABSTRACT

The modeling of electrochemical systems, and in general the modeling of reacting flows exposed to electric field, is a complex problem to the point that analytic solutions exist only for simplified cases despite the increasing computer power. The state of art shows major improvements in the fluid-dynamics of electrochemical reactors; but the full coupling of the flow with the electric field in presence of concentrated electrolytic solutions still needs to be properly investigated. The coupling gets even more critical along the charged interfaces where heterogeneous reactions are modeled through the non-linear Butler-Volmer equation.

Commercial software are slowly try to connect electrochemical modules to the well validated CFDs, but most of the time costly licenses, and poor accessibility to the source code, do not allow a deep integration between the two. Instead, this research study proposes an open-source code implemented in OpenFOAM, that guarantees full accessibility to the source code, user's modifications, full transparency of the model's details, and any possible further developments required by the specificity of the problem.

The final code implements the mass transfer of a cell where the concentrated solution (molten salt) is a two-phase turbulent incompressible flow and the electrochemical surface reactions consider tertiary current distributions. The aim of this work is to create an open source platform to predict and analyze industrial reactor's performances. The advanced modeling can be later exploited and used as a validation instrument for new electrochemical concepts.

Keywords: Electrochemical reactor, Coupling, Butler-Volmer, Tertiary current distribution, Turbulence, Two-phase flow, OpenFOAM

ACKNOWLEDGEMENTS

They say *it never gets easy, but you can always get better*. True, but incomplete. Sometimes to get better you also need the right frame of people around you.

I would like to thank Pierre, and maybe everybody else should do the same. Thanks to him the dictionary has an extra verb: to Pierre. Pierring somebody's results means finding the bright side even in the most unsuccessful presentation of all times! Thanks Pierre for betting on me.

I would like to thank Martin for always finding the time to be annoyed by my project. Thanks to the several meetings we had, I finally know where you keep your food stocks.

Talking about food, I would like to thank Camila for bringing in our office the tradition of covering the central table with delicious patisserie. Thanks to you, everybody in the office got 10 pounds! Thanks to you I also got light in my dark moments, and happiness in my sad days. I hope to cross you again, somewhere in the world.

I would like to thank Elaheh. We started this adventure together and we went through lots of things. Good and bad, but mostly good. Thanks for introducing me to your culture, but above all thank you for showing me how a strong woman looks like.

Thanks to Kevin for being my SoS french aid, and my sporty-octopus fellow

Thanks to Jamie for teaching me how Friday nights should be spent: let's doooo it!

Thanks to my buddy Raj, you've been witnessing all the important moments of this trip of mine. I hope it'll be the same for the others ahead!

Grazie a Luigi per avermi ricordato la bellezza delle cose, a Claudia per avermi dato il coraggio che mi mancava, ed ad Ari per avermi fatta entrare nel suo mondo.

Grazie a Toti, a Carlotta, a Tommaso e alla futura Matilde, per avermi fatto godere della bellezza della loro famiglia.

Casa MaPa, Mista & Bobbi senza di voi in Canada mi sarebbe mancata la dolcezza, ma forse avrei visto meno serie tv ed avrei mangiato di meno!

Alla lista vorrei aggiungere chi ancora non riesce a sbarazzarsi di me neanche dopo circa 20 anni. Grazie Ire per essere sempre a "portata di telefono", il tuo buonumore continua ad essere contagioso. E grazie a te Pao neo mamma, per essere tra le poche genuine persone capaci di dare senza secondi fini. Come te non ne ho piú trovate in giro per il mondo.

Grazie a Chiari, perché finalmente quest'anno per la prima volta in assoluto nella storia, sei riuscita a riunirci tutti allo stesso tavolo!

Grazie alla piccola anima innocente di casa, Enri. Grazie per esserci stata... prima, durante e dopo. Non riesco mai veramente ad arrabbiarmi con te!

Non possono mancare mamma e papá. A voi il grazie piú grande per aver accettato le mie sempre piú difficili scelte di vita.

TABLE OF CONTENTS

LIST OF FIGURES

LIST OF TABLES

CHAPTER 1

INTRODUCTION

In the electrochemical industry, controlling the various phenomena occurring simultaneously is a relevant issue. The analysis of their role on reactor's design can lead to more efficient apparatus inducing consistent amount of money savings. A must for all companies. Mathematical modeling of the electrochemical systems, and more in general of reactive flow systems in presence of electric field, represents a complex task that can be solved only through simplified solutions despite the increasing power of modern computers. The need of commercial software to face these extremely complex problems is unquestionable. However, it cannot be ignored that such softwares are mostly restricted to well-defined applications, so it is difficult, and sometimes impossible, to adapt them to research and advanced targets. From this, arises the necessity to create a numerical model that does not limit its use to specific cases, and that can be employed on a wider range of applications. The design of electrochemical reactors requires predicting such quantities as the current and the potential distributions, the energy efficiency for multiple electrode reactions, the conversion pace of the reactant or the product, and the selectivity of a desired product. In short, designers have to ensure that the reaction occurs with the highest efficiency towards the desired output product, requiring the cheapest operative solution. Special care has to be provided to obtain a uniform reaction rate along the active surfaces. In this way electrodes are consumed homogeneously, and stagnant zones, as well as flow re-circulation are avoided. Meanwhile, the model has to guarantee the correct interpretation of the physics. If on one side approximations and simplifications are needed to solve the multidisciplinary problem, on the other side a fair representation of the reality must be achieved. For this reason the modeling of turbulence is integrated in this study, capturing the right flow patterns to access the correct mass transfer distribution.

This research is placed within this frame. The project is ambitious, but the presence of industrial expertise on one side and academics on the other, aspires to most exploit all the available resources. The intent is to develop, validate and apply a mathematical model to electrochemical technologies.

The project is decomposed into intermediate objectives.

The first assembles the skeleton of the numerical model. The equations of continuity, and momentum are solved alongside the conservation of charges and the transport of ions. A moving mesh is also embedded to predict the geometry deformations due to material deposition and metal corrosion. Thanks to this, it is possible to estimate the cell life time. This first model is applied to a parallel plate electrochemical reactor (PPER), in which chemical reactions are facilitated through electrical energy. A PPER is basically a vessel where an anode and a cathode are assembled on parallel slabs. They are physically separated by an electrolyte medium containing reactants and products. The electrolyte is injected in the reactor with a certain known velocity, and it reacts as soon as it comes in touch with the active plates. Inside the cell two half-sides are identified. Species from one half-cell lose electrons (oxidation), while species from the other half-cell gain electrons (reduction).

The second objective introduces the modeling of turbulence. For this purpose, the modeling is applied to a different geometry, where turbulence plays a significant role. The prototype *FM01-LC* is a filter-press cell on a laboratory-scale patented by the Imperial Chemical Industries, ICI [20]. It is a scaled-down version of the *FM21-SP* cell which is used in the chloralkali production [68], but also in fundamental studies of several electrochemical process, such as electro-synthesis [56], water treatment [41], and energy storage processes [69]. Its low cost yet extremely versatile electrolyser is adopted in over 45 plants worldwide with a chlorine production capacity in excess of 1 million tonnes per year. This makes the *FM01-LC* the most representative test-case to investigate.

The third objective opens up the application range of the model to all those electrochemical reactors where the presence of a second phase in the electrolyte affects significantly the flow field. Indeed, heterogeneous reactions occurring at the electrodes, might release gas products in the electrolyte, changing completely the dynamics of the cell. This part of the project is driven by the increasing interest of industries in exploiting Lithium's characteristics, such as lightness and high reduction potential. To satisfy the market needs, a standard cell for the production of lithium by electrolysis of $LiCl$ is selected. Single sized bubbles are injected at the anode with a certain distribution, and induce a convective mechanism in the bulk of the cell otherwise acting as a batch reactor.

Therefore, the final OpenFOAM code models a two-phase turbulent flow, where mass transfer in concentrated solutions (molten salt) is solved along with electrochemical surface reactions considering a tertiary current density distribution.

CHAPTER 2

Electroplating of copper in a rectangular cell

2.1 Avant-propos

Auteurs et affiliation:

- Giuliana Litrico: étudiante au doctorat*
- Camila B. Vieira: étudiante au post-doctorat*
- Ehsan M. Askari: étudiant au doctorat*
- Pierre Proulx: professeur*

* Université de Sherbrooke, Faculté de génie, Département de génie chimique et de génie biotechnologique

Date d'acceptation: 16 Décembre 2016

État de l'acceptation: version finale publiée

Revue: Chemical Engineering Science

Titre français:
Modèle fortement couplé pour la prédiction des performances d'un réacteur électrochimique

Contribution au document:
Cet article contribue à la thèse en développant un modèle mathématique capable de résoudre le fort couplage entre la dynamique des fluides, le transport d'ions et la conservation des charges électriques.

Résumé français:
Un modèle mathématique a été développé afin d'étudier et de prédire les performances de réacteurs électrochimiques. Le modèle est résolu numériquement en utilisant la méthode des volumes finis et en utilisant la librairie ouverte de mécanique des fluides numériques OpenFOAM. Le code développé, nommé POTisoFOAM traite le complexe ensemble d'équations

et de conditions aux limites qui représentent un système de déposition électrochimique de cuivre. Le code développé utilise l'algorithme PISO pour le traitement de l'écoulement incompressible transitoire. Une seconde séquence de prédicteur-correcteur combine les équations de transfert de masse, de potentiel électrique et de densité de courant. Elle considère la convection, la migration et la diffusion en faisant l'hypothèse de solution diluée et complète le système avec la conservation de la masse et l'électroneutralité. La solution de la conservation des charges électriques donne comme résultat le champ électrique ce qui permet de trouver la distribution de densité de courant tertiaire. Aux électrodes, la présence de la double couche électrochimique affecte le comportement de l'électrolyte avoisinant. Cette interaction est modélisée avec les équations de Butler-Volmer et ses approximations souvent utilisées: linéaire et logarithmique. De plus, la mécanique des fluides et la modélisation électrochimique sont couplées avec les changements de géométrie associés à la déposition et à la consommation des électrodes par une méthode de modification dymanique du maillage de volumes finis, ce qui intensifie le couplage entre les champs du modèle. Les résultats sont présentés et analysés.

2.2 Strongly coupled model for the prediction of the performances of an electrochemical reactor

A mathematical model is developed to investigate and predict the performances of electrochemical reactors. It is implemented with a finite volume method, and solved by means of the open source package OpenFOAM. The new solver, named *POTisoFOAM*, deals with an intricate set of equations and boundary conditions which describe an electrochemical copper deposition system. The code uses the PISO algorithm for the transient incompressible flow field. A second predictor-corrector sequence combines mole fraction, electric potential and current density. It considers the convection, migration and diffusion mechanisms under the assumption of a dilute solution, mass conservation, and local electro-neutrality. The conservation of charges provides the electrical field which in turn allows the reconstruction of the tertiary current density distribution. At the electrodes, the presence of a charged double layer affects the behavior of the neighbor electrolyte. The effect of this interaction is modeled through the Butler-Volmer equation or its two commonly used simplifications: linear and logarithmic. Furthermore the fluid dynamic and the electrochemical modeling are coupled with the geometric changes of the active plates due to either material deposition or consumption of the electrodes. A dynamic mesh method has been integrated, increasing yet the level of coupling between electrical, chemical and fluid dynamic fields. Results are here presented and analyzed.

2.2.1 Introduction

Electrochemical reactors and in general electrochemical systems nowadays, have a leading role in a wide range of applications: from batteries to fuel cells, from electroplating to water treatments. The main physical characteristic of an electrochemical system, as viewed through the eyes of engineers and scientists, is indeed the simultaneous treatment of many complex and interacting phenomena [5, 42]. To overcome the issue, several simplifications are commonly used with the intent to decrease the level of coupling. They provide satisfactory estimation of the solution, but cut down the generality of the problem and restrict the solution's domain to very specific cases. Alternatively, commercial software use specific packages for electrochemical reactors, presenting "black-box" solutions that allow little insight into the mathematical and numerical difficulties of the model. Therefore, it is of interest for research engineers the need to operate with a tool having a penetrable architecture such as *OpenFOAM* (OF). This is a free, open source software package, specialized in Computational Fluid Dynamics (CFD) with a large user base across most

areas of engineering and science, offering complete freedom to customize and extend its existing functionality. For this reason the present work aims to set up, implement and develop a numerical model that can investigate and predict the productivity of general electrochemical reactor system by means of *OpenFOAM*.

2.2.2 Geometry and mesh

A Parallel Plate Electrochemical Reactors (PPER), is a vessel which facilitates chemical reactions through the introduction of electrical energy, where an anode and a cathode are assembled on parallel slabs [70]. The electrodes are physically separated by an electrolyte medium containing reactants and products. The electrolyte is injected in the reactor with a certain known velocity, and it reacts with the active electrodes. Inside the cell two half-sides are identified. Species are oxidized in one half-cell (anode), while in the other half-cell (cathode) species are reduced.
In this work the parallel plate configuration is used as a test-case. The full cell is represented by a rectangular geometry. Table 2.1 provides its dimensions and the number of grid elements for both the active plates (read anode and cathode), and the inactive ones. It can be noticed that the flow is 2D (1 grid element in the y-direction), and it is discretized with a total number of 22,750 elements for the entire reactor. Figure 2.1 shows a simplified sketch of it.

	Dimensions [cm]		**Number of elements**	
Plates	*inactive*	*active*	*inactive*	*active*
x-direction [L]	70	35	140	175
y-direction [W]	10	10	1	1
z-direction [H]	1	1	50	50

Table 2.1 Geometry and mesh characteristics.

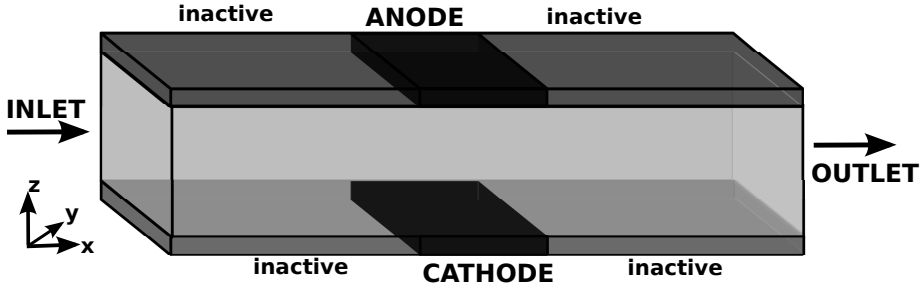

Figure 2.1 Sketch of the geometry.

2.2.3 Mathematical and numerical formulation

This work simulates a copper depletion system. The electrolyte is modeled as a plug flow, with a mixture of [0.002 M] $CuSO_4$ + [0.1 M] H_2SO_4. Once the electrolysis starts, the anode releases cupric ions while the cathode captures and transforms them into solid copper. The same reaction (Eq. 2.1) occurs at both the electrodes, reducing cupric ions at the cathodic side (left to right), and oxidizing them at the anode (right to left). No secondary reactions are taken into account.

$$Cu^{2+} + 2e^- \underset{anode}{\overset{cathode}{\rightleftharpoons}} Cu(s) \tag{2.1}$$

Previous works [18, 19, 25, 73] have investigated a similar electrochemical process in a rotating disk electrode configuration, implying a multi-ion deposition model and partial dissociation of HSO_4^-. In the present study the low dissociation of the acidic bath was not included into the model as suggested in [15], since the diffusivity of HSO_4^- and SO_4^{2-} in dilute media is almost identical; therefore the electrolyte is only made of Cu^{2+}, SO_4^{2-}, and H^+ species. For further details Table 2.2 presents the composition of the electrolytic solution, and Table 2.3 provides the input parameters to start the simulation and tune the electrode kinetics. The electrolyte is injected with the same composition for the entire simulation time.

Species	$\boldsymbol{Y_{Cu^{2+}}}$	$\boldsymbol{Y_{SO_4^{2-}}}$	$\boldsymbol{Y_{H^+}}$
Initial Y_s	0.013	0.33	0.657
Diffusivity 10^{-9} $[m^2/s]$	0.610	1.065	9.312

Table 2.2 Electrolytic solution properties.

Input	**Values**	**Units**
ΔE_{cell}	0.4	V
U_x	1	ms^{-1}
$i_{0,anode}$	18.42	$A\,m\,(kg\text{-}mol)^{-1}$
$i_{0,cathode}$	133.88	$A\,m\,(kg\text{-}mol)^{-1}$
α_{anode}	0.5	-
$\alpha_{cathode}$	0.21	-

Table 2.3 Input paramenters [16].

In this work, the authors have also implemented the changes in the geometry due to the amount of deposited copper at the cathode and the consumption of the anode.

The equations are implemented with finite volume method in OpenFOAM. The solver is named *POTisoFOAM*, it has a tree-structure where each branch is responsible for the modeling of a field so that everything is interconnected through the central trunk, but still independently accessible.

Pressure and velocity fields

The solver *POTisoFOAM* starts by solving the pressure p, and velocity $\boldsymbol{U}$ fields. It considers the continuity Eq. 2.2 and the Navier-Stokes Eq. 2.3:

$$\nabla \cdot (\boldsymbol{U}) = 0 \tag{2.2}$$

$$\frac{\partial \boldsymbol{U}}{\partial t} + \boldsymbol{U} \cdot \nabla \boldsymbol{U} = -\frac{\nabla P}{\rho} + \nu \nabla^2 \boldsymbol{U} \tag{2.3}$$

The two equations are solved together inside a PISO algorithm (Pressure Implicit with Splitting of Operators [12, 21–23, 45]), which helps the handling of the non linearity in Eq. 2.3. It basically splits the operators into an implicit predictor and multiple explicit corrector steps. The predictor uses the pressure values from the previous time step to discretize the equation of motion and estimate a first guess velocity which is non-divergence free. At this point the coefficient matrix of the system is decomposed into two matrices: the first containing just the diagonal terms, and the second all the off-diagonals. Next, with Eq. 2.2 a predicted value of pressure is estimated, and it is used in an explicit scheme to correct the velocity, which this time results to be divergence-free. The number of pressure updates and velocity corrections can vary depending on the desired accuracy. The advantage of using this algorithm lies on the splitting operators. Thanks to it in the corrector loops the solution is provided by inverting a diagonal matrix instead of a full one. Therefore storing and accessing matrices is faster, and the CPU time required decreases. In short the *PISO-loop*:

- imposes an initial p
- predicts $\boldsymbol{U}$ (Eq. 2.3)
- evaluates p (Eq. 2.2)
- corrects $\boldsymbol{U}$ (Eq. 2.3)

Mole transport

The mole transport equation Eq. 2.4, models the transport of ions within the cell:

$$\frac{\partial Y_s}{\partial t} = -\nabla \cdot \left[- D_s \, \nabla Y_s \; - \; \left(\frac{F}{RT} z_s D_s Y_s \right) \nabla E \; + \; \boldsymbol{U} Y_s \right] + S_r \tag{2.4}$$

In Eq. 2.4 the mole fraction is defined as $Y_s = C_s/C_{TOT}$, and the subscript s identifies the species. Each species has its own diffusion coefficient D_s, and its own charge number z_s indicating the sign and the number of charges carried by each species, $z < 0$ for anions and $z > 0$ for cations. The Faraday's constant is F, while R is the universal gas constant, and T the flow average temperature. The equation presents a transient term on the left hand side. On the right side within the squared brackets there is the flux of ions (see Eq. 2.8), which consists of three contributions. The first is the diffusion, which is driven by the concentration gradients (∇Y_s) and points towards small concentrations. The second is the migration and it is led by the gradient of the electric potential (∇E) pushing positive ions to the negative electrode and vice versa. Finally the third share is the convection mechanism, and moves ions with the flow velocity ($\boldsymbol{U}$). The last term outside the brackets (S_r) represents the rate of homogeneous chemical reaction in the solution that produces or consumes the species under investigation. It might be seen as a source or sink term according to which side reaction occurs. In this work, as previously mentioned, no side reactions are considered, hence this term is null. To ensure mole conservation, Eq. 2.5 is added to the system. Further details on the strength of the coupling are given in the next section.

$$\sum_s Y_s = 1 \tag{2.5}$$

Electrochemistry

Inside the electrolyte Eq. 2.6 makes sure that the total current density is maintained divergence-free.

$$\nabla \cdot \boldsymbol{i} = 0 \tag{2.6}$$

where $\boldsymbol{i}$ is the sum of the single currents carried by each species as shown in Eq. 2.7

$$\boldsymbol{i} = F \sum_s z_s \boldsymbol{N}_s \tag{2.7}$$

and $\boldsymbol{N}_s$ is the flux as expressed in Eq. 2.8, where the s-th ions are transported by diffusion, migration, and convection.

$$\boldsymbol{N}_s = \; -D_s \, \nabla Y_s \; - \left(\frac{F}{RT} z_s D_s Y_s \right) \nabla E \; + \boldsymbol{U} Y_s \tag{2.8}$$

Now Eq.2.7 and Eq. 2.8 can be combined together transforming Eq. 2.6 into an equivalent equation (Eq. 2.9) where the tertiary current density distribution seems to disappear in favor of the electric potential E. This manipulation permits a straightforward coupling with the mole transport Eq. 2.4 without passing through the total current density.

$$\nabla^2\Big(\frac{F^2}{RT}\sum_s z_s^2 D_s^2 Y_s \;\; E\Big) + \nabla^2\Big(F\sum_s z_s D_s \;\; Y_s\Big) = 0 \tag{2.9}$$

It can be noticed that in Eq. 2.9 there are only two contributions, the first coming from the migration transport and the second from the diffusive mechanism. The missing term is related to the convection. Its absence is caused by the electroneutrality Eq. 2.10, which states that it cannot exist any significant unbalance of positive and negative ions in the solution.

$$\sum_s z_s Y_s = 0 \tag{2.10}$$

Due to the strong coupling between the mole fractions and the electric potential, the two cannot be split and solved independently. Therefore, the strategy of solution is to use another predictor-corrector loop counting 4 unknowns ($Y_{Cu^{2+}}, Y_{SO_4^{2-}}, Y_{H^+}, E$), and 4 equations (Eqs. 2.4, 2.5, 2.10, 2.9). Eq. 2.4 models the distribution of cupric ions, using the electric potential at the previous time step. Subsequently the other two mole fractions of SO_4^{2-} and H^+ are estimated by means of Eq. 2.5 and Eq. 2.10. Finally, the electric potential field is corrected and updated through Eq. 2.9, so that also the three species can be re-calculated. The loop is repeated until the desired accuracy of the solution is reached.

Boundary conditions

In an electrochemical cell, the interface between the bulk solution and the solid metal plate presents a Double Layer (DL). It plays an important role linking simultaneously electric potential, surface tension, composition of the bulk solution, and surface concentrations of various species [42]. The complexity of this physical-chemical system, does not allow an easy solution for the closure of the PDEs system. Nevertheless, a set of boundary

conditions have to be defined (Eqs.2.11). Boundaries are named after Figure 2.1.

$$\begin{array}{ccc} \textit{Inlet} & \textit{Inactive walls} & \textit{Outlet} \\ \begin{cases} \boldsymbol{U} & = \boldsymbol{U}_{in} \\ \nabla p & = 0 \\ Y_s & = Y_s^b \\ \partial_n E & = 0 \end{cases} & \begin{cases} \boldsymbol{U} \cdot \boldsymbol{n} & = 0 \\ \nabla p & = 0 \\ \partial_n Y_s & = 0 \\ \partial_n E & = 0 \end{cases} & \begin{cases} \nabla \cdot \boldsymbol{U} & = 0 \\ p & = p_{atm} \\ \nabla \cdot Y_s & = 0 \\ \nabla \cdot E & = 0 \end{cases} \end{array} \tag{2.11}$$

Assuming that the electrodes' metal surfaces are impenetrable, the boundary conditions on the velocity and pressure are the same for all the active and inactive walls. This is not the case for the mole factions (Eq. 2.12). At the electrodes depending on the species reactivity the conditions become:

$$\textit{Active walls} \quad \begin{cases} \boldsymbol{N}_s \cdot \boldsymbol{n} = \pm \sum_i \dfrac{st_{sq} \boldsymbol{i}_q \cdot \boldsymbol{n}}{n_q F} & s = Y_{Cu^{2+}} \\ \boldsymbol{N}_s \cdot \boldsymbol{n} = 0 & s = Y_{SO_4^{2-}}, Y_{H^+} \end{cases} \tag{2.12}$$

where st_{sq} is the stoichiometric coefficient of the s-th species in the q-th reaction, and n is the number of electrons exchanged in the specific reaction. This work only considers the reaction in Eq. 2.1, so the subscription q can be omitted. The sign $\pm$ depends whether the reaction is occurring at the anode or at the cathode. The modeling of the product $\boldsymbol{i} \cdot \boldsymbol{n} = i_n$, hides the exponential bounding of the current density with the the surface overpotential as expressed in Eq. 2.13.

$$i_n = i_{0,el} \left[\frac{Y_{red}^{surf}}{Y_{red}^b} exp \left\{ \alpha_{sym} \ \frac{nF}{RT} \eta \right\} - \frac{Y_{ox}^{surf}}{Y_{ox}^b} exp \left\{ -(1 - \alpha_{sym}) \frac{nF}{RT} \eta \right\} \right] \tag{2.13}$$

Here $i_{0,el}$ is the exchange current density associated to the null potential, α is the symmetry factor also known as the charge transfer coefficient, the subscripts ox and red stand respectively for oxidant and reductant components, while the superscripts $surf$ and b indicate whether the mole fractions are respectively at the surface or in the bulk. The surface electrode over-potential η is a function of the measured electrode potential V_{el}, the calculated equilibrium potential E^{∞}, and the solution potential close to the surface E^{surf} as shown in Eq. 2.14, [14].

$$\eta = V_{el} - E^{surf} - E^{\infty} \tag{2.14}$$

where the equilibrium potential is expressed as in Eq. 2.15. (see Nomenclature)

$$E^{\infty} = E^{0} - E^{0}_{RE} - \frac{RT}{nF} ln \left\{ \Pi_s \left(\frac{Y^b_s}{\rho} \right)^{st_{sq}} \right\} + \frac{RT}{nF} ln \left\{ \Pi_s \left(\frac{Y_{s,RE}}{\rho} \right)^{st_{sq,RE}} \right\} \tag{2.15}$$

The non-linear Eq. 2.13 can degenerate into one of the 3 following formulations:

- *No mass transfer effects.*
  If the solution is well mixed, or currents are low such that concentrations at the surfaces and at the bulk are indistinguishable, Eq. 2.13 turns into the well known Butler-Volmer (BV) formulation Eq. 2.16

$$i_n = i_{0,el} \left[exp \left\{ \alpha_{sym} \frac{nF}{RT} \eta \right\} - exp \left\{ -(1 - \alpha_{sym}) \frac{nF}{RT} \eta \right\} \right] \tag{2.16}$$

- *Small* $|\eta|$
  For small value of η the current is linearly related to the overpotential, where the charge transfer resistance R_{ct} is introduced

$$i_n = \frac{\eta}{R_{ct}} \qquad , \qquad R_{ct} = \frac{RT}{i_{0,el}\, F} \tag{2.17}$$

- *High* $|\eta|$
  For high values of the overpotential, one of the exponential terms becomes negligible with respect to the other, leading to a much easier formulation of the BV equation also known as Tafel equation

$$i_n = \begin{cases} i_{0,el} \left[exp \left\{ \alpha_{sym} \frac{nF}{RT} \eta \right\} \right] & \eta >> 0 \\ \\ i_{0,el} \left[exp \left\{ -(1 - \alpha_{sym}) \frac{nF}{RT} \eta \right\} \right] & \eta << 0 \end{cases} \tag{2.18}$$

To complete the Eqs. 2.11 it is still necessary to impose a constraint on E affected by the presence of the DL as well. This is done by making explicit E^{surf} from Eq. 2.14 :

$$\begin{cases} \textit{Active walls} \\ E^{surf} = V_{el} - \eta - E^{\infty} \end{cases} \tag{2.19}$$

The overpotential η is provided by the inversion of Eq. 2.16 or 2.17, or 2.18. While the manipulation of the latter two can be easily done, the BV equation requires a particular attention. First the current density is estimated at the boundaries, then the overpotential and in turns the E^{surf} are calculated by using the Ridders' method [49]. It is a false position method for exponential functions, which requires two initial values lying on different sides of the root being sought. The function to be inverted $f(x)$ is then evaluated at those initial values, and it is transformed into a straight line $g(x)$ thanks to the linearisation in Eq. 2.20

$$g(x) = f(x)\, e^{(x-x_1)Q} \tag{2.20}$$

This method can be seen as a non-linear regula-falsi method, and a sequence of evaluations of $g(x)$ are performed until the roots η are found.
In short the *POTiso-loop*:

- imposes an initial E and η
- predicts $Y_{Cu^{2+}}$ (Eq. 2.4)
- predicts $Y_{SO_4^{2-}}$ (Eq. 2.5)
- predicts Y_{H^+} (Eq. 2.10)
- evaluates E (Eq. 2.9)
- reconstructs $\boldsymbol{i}$ (Eq. 2.7)
- inverts i_n to get η (Eqs. 3.23, 2.17 or 2.18)
- updates boundary conditions (Eqs. 2.12 and 2.19)
- corrects the mole fractions

and iterates until reaching the desired tolerance.

Geometry changes

The electrochemical reactions occurring inside the cell, cause small changes in the geometry of the active plates. At the cathode the deposition of pure solid copper confines the flow in a smaller channel volume. On the contrary at the anode a corrosive mechanism takes place releasing cupric ions and increasing the original electrolyte channel volume, as shown in Figure 2.2.

In this study a dynamic mesh is used to reproduce the stretching and squeezing of the original grid. The reactor shape is preserved, and no topological changes arise. The mesh manipulation model solves the grid motion equation (Eq.2.21) written in terms of the laplacian of the displacement:

$$\nabla \cdot (\gamma \nabla \boldsymbol{d}) = 0 \tag{2.21}$$

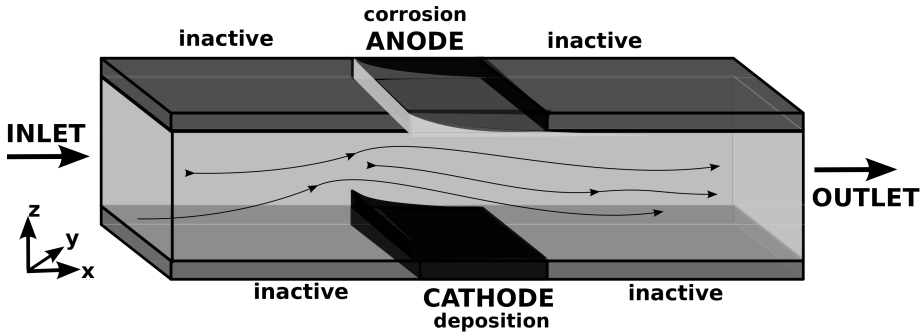

Figure 2.2 Sketch of the geometry changes.

The displacement $\boldsymbol{d}$ represents a point vector field, while γ is the diffusion coefficient propagating the grid motion information all over the geometry, which is modeled with an inverse distance method in its quadratic form (Eq. 2.22)

$$\gamma \sim \frac{1}{l^2} \tag{2.22}$$

At each time iteration a routine updates the mesh grid by:

- identifying the electrodes
- finding the link between the local and global reference systems
- getting the point vector field of the selected electrode
- interpolating the quantities from the grid-faces to the points
- shifting the grid-points by an imposed time-dependent displacement d_{imp}
- updating the mesh

The vector d_{imp} previously mentioned, imposes the desired displacement to the surfaces where the impingement is occurring (Eq. 2.23). It is proportional to the flux of cupric ions which approaches the electroactive plates, and it varies linearly with time t. Only its z-component is tracked since it is the largest and consequently the limiting one.

$$d_{imp} = (\boldsymbol{N}_{\boldsymbol{Cu^{2+}}} \cdot \boldsymbol{n})t \tag{2.23}$$

The mesh manipulation routine is solved at the very last of each iteration because it requires the most updated values of the copper mole fraction. The way the active plates are changing their geometry gives a feedback on how unevenly the electrodes are consuming, providing information about the system life-time.

2.2.4 Results and discussions

Numerical results are presented and discussed in this section. All the graphs below report steady-state solutions along a simulation time of $2000s$. Before presenting the full set of results, it is necessary to spend few words about the numerical schemes used. The time derivative, although it does not represent a crucial point for this work, is implemented with a first order implicit Euler scheme. The gradient and the laplacian are discretized by a Gauss linear integration with central difference. Orthogonal corrections are required when the deformations of the active plates occur. A limited linear scheme is involved in the discretization of the divergence. It is a second order scheme bounded by a Sweby limiter [23].

Furthermore Table 2.4 shows the relaxation factors on pressure, velocity, and overpotential imposed to improve the stability and speed up the convergence of the solution. The mole fractions make use of a relaxation factor of 1 to reinforce and guarantee their matrix diagonal dominance.

Variable	**Relaxation factor**
p	0.3
$\boldsymbol{U}$	0.7
η	0.5
Y_i	1

Table 2.4 Relaxation factors used.

Mesh dependency study

A spatial grid convergence analysis is carried out. The discretization error is quantified by performing the simulation on three different grid sizes with a minimum grid refinement ratio of $r \geq 1.1$ [55]. The functional f is the mole fraction of copper integrated over the electrode length. Table 2.5 provides the information about each mesh.

Grid ID	**Tot cells**	f
1	91,000	0.0161
2	22,750	0.0160
3	5700	0.0158

Table 2.5 Grids specifics.

The order of convergence of the solution is estimated as in Eq. 2.24, where f_i is the functional related to the i-th grid ID:

$$m = ln\Big(\frac{f_3 - f_2}{f_2 - f_1}\Big)\frac{1}{ln(r)} \tag{2.24}$$

To estimate the "real" solution, Richardson extrapolation predicts what is the value of the functional if a zero grid spacing would be applied (Eq. 2.25) [51]:

$$f_0 = f_1 + \frac{(f_1 - f_2)}{r^m - 1} \tag{2.25}$$

The generalized theory of Richardson extrapolation makes use of the two finest grid resolutions and requires the calculation of a Grid Convergence Index (GCI) as expressed in Eq. 2.26. It gives an indication on how much the solution would change with further refinement of the grid.

$$GCI_{ij} = \frac{Fs}{r^m - 1}\ \Big|\frac{(f_i - f_j)}{f_i}\Big|\ 100\% \tag{2.26}$$

where Fs is a security factor set to 1.25 [61]. Besides, an asymptotic range of convergence of 1, described in Eq. 2.27 is desired to assure that the solution is within the estimated error band [61].

$$asyR = \frac{GCI_{23}}{r^m\, GCI_{12}} \sim 1 \tag{2.27}$$

Table 2.6 shows the final details of this analysis, and indicates that the grid with **ID 2** has the best trade-off between accuracy and computational time.

r	**m**	$\boldsymbol{GCI_{12}}$	$\boldsymbol{GCI_{23}}$	$\boldsymbol{asyR}$
2	3.66	0.0164%	0.2081 %	1.0013

Table 2.6 Optimum mesh results.

POTisoFOAM

In this subsection the numerical performances of the new developed solver *POTisoFOAM* are examined. The cell geometry is configured according to Table 2.1, and the mesh in use has the **ID 2** in Table 2.5. Figure 2.3a presents the evolution of copper mole fraction along the anode. Cupric ions are released from the anode and pushed trough the electrolyte. At the entrance of the electrode it is observed that the production is lower than at its end. This is because the effect of the convective mechanism is stronger at the entrance of the electrode and it is decreasing with the electrode length where the migration effect is

becoming more important. To verify what just said, an additional test has been carried out. It reproduces the same scenario with the only difference being an extremely reduced velocity of the electrolyte (almost stagnant). In this way the convective mechanism is negligible, and the entire active surface reacts simultaneously driven just by the migration and the diffusive contributions. In order to investigate the contribution of the diffusive transport, the cupric mole fraction along the z-axis is shown in Figure 2.3b at different Peclet numbers, where Peclet is defined as $Pe = ULc/D$. By observing the graph, at high Peclet (red solid line) the convective contribution promotes a constant Y_{Cu}^{2+} along the bulk of the electrolyte ($0.1 < z/H < 0.9$). For $Pe = 1$ (blue dashed line) the sum of the migrative and diffusive mechanism becomes comparable to the convective share, and the range of uniformity in the bulk is reduced to $0.2 < z/H < 0.7$. Besides, it is remarkable that for both cases the concentration of copper at the top of the cell is higher than at the bottom. The reason is because at the cathode ($z/H = 0$) the reacting cupric ions produce solid copper, therefore they leave the cell and are not any more accounted in the modeling.

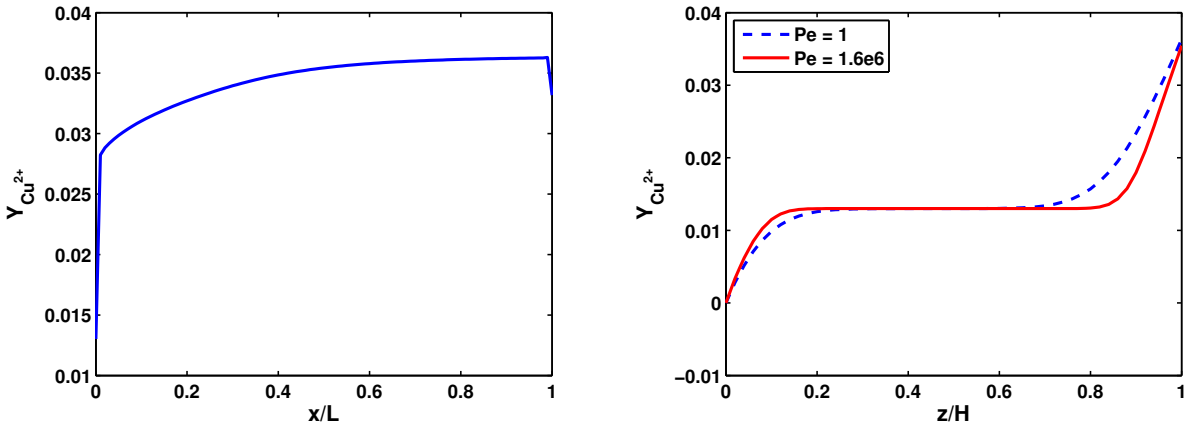

(a) Along the anode. (b) Along a vertical cut.

Figure 2.3 Mass fraction of cupric ions.

To better investigate this behavior close to the electrodes, the time evolution of the punctual mole fraction of copper is plotted. Figure 2.4a shows the decrease of $Y_{Cu^{2+}}$ close to the electrode ($z/H = 0.02$). The variation is of the order of 10^{-3}, as it was already anticipated in Figure 2.3b. It indicates that the limiting current density is reached, and that the electrode process is mass transfer controlled. On the contrary close to the anode

($z/H = 0.98$) the cupric mole fraction increases by time and is released into the electrolytic solution.

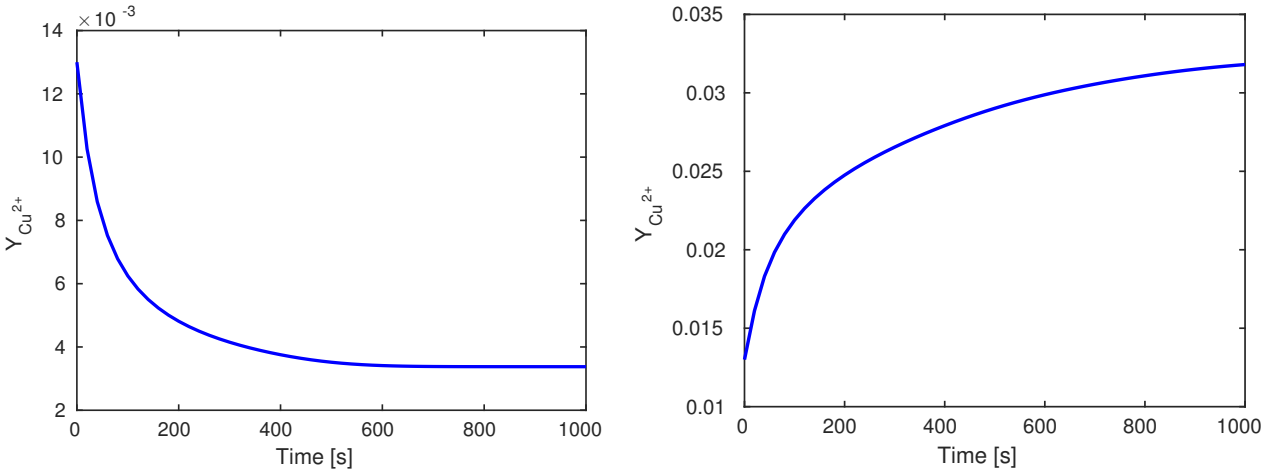

(a) Point close to the cathode.

(b) Point close to the anode.

Figure 2.4 Time evolution of the $Y_{Cu^{2+}}$ extrapolated from two different points.

Figure 2.5 plots the electric potential along a vertical cut at $x = L/2$. The plotted line has an angular coefficient of 0.4. The initial potential drop of the cell is set to -0.4 [V], and for simplicity purposes the anode is set to zero, so that the ΔE_{cell} coincides with the initial cathode potential. The vertical cut is extrapolated from Figure 2.6 where just the region including the active plates is reported.

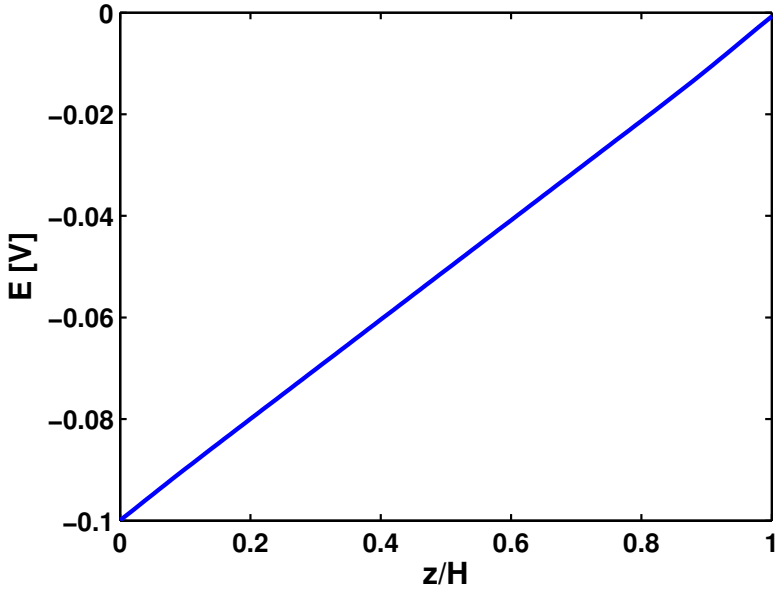

Figure 2.5 Electric potential along a vertical cut, at $x = L/2$.

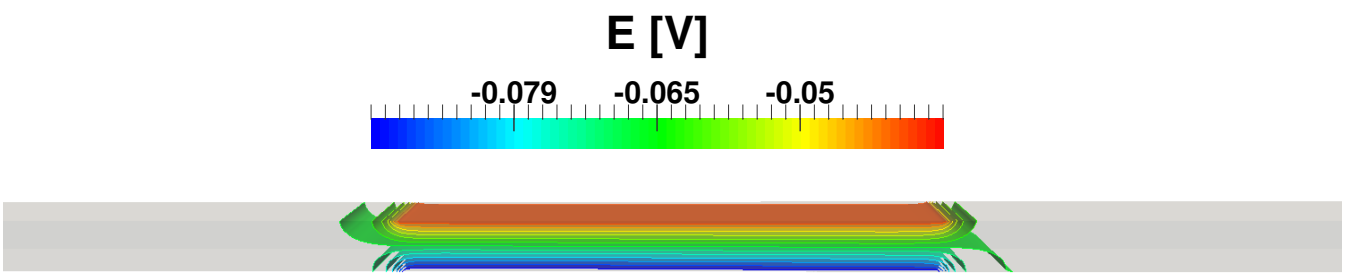

Figure 2.6 Contours of the electric potential E.

The curvatures of the equipotential E at the extremities of the electrodes (Figure 2.7a and 2.7b) show result to be not fully symmetric with respect to the horizontal axis due to the effects of the convective mechanism. The same trend is reflected in the current density field. In Figure 2.8a at the electrode's entrance the curls of the current contours are more pronounced with respect to those at the exit. Indeed in Figure 2.8b the potential gradient is dumped by the electrolyte stream dragging charges away from the electrode.

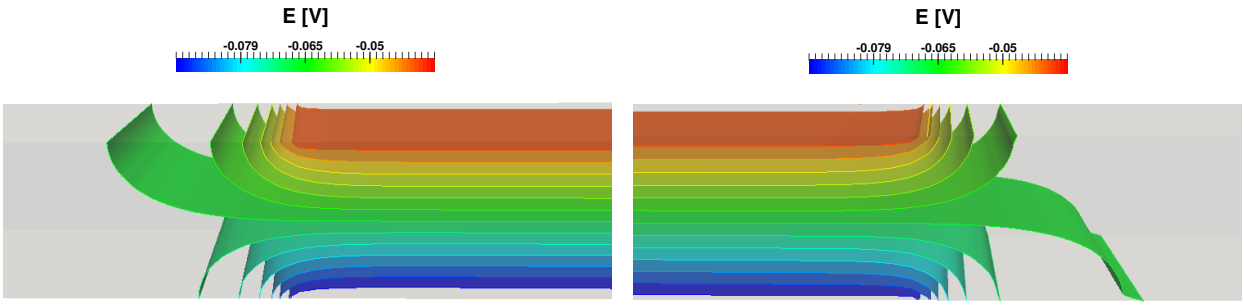

(a) Electrodes' entrance. (b) Electrodes' exit.

Figure 2.7 Contours of E at the extremities of the electrodes.

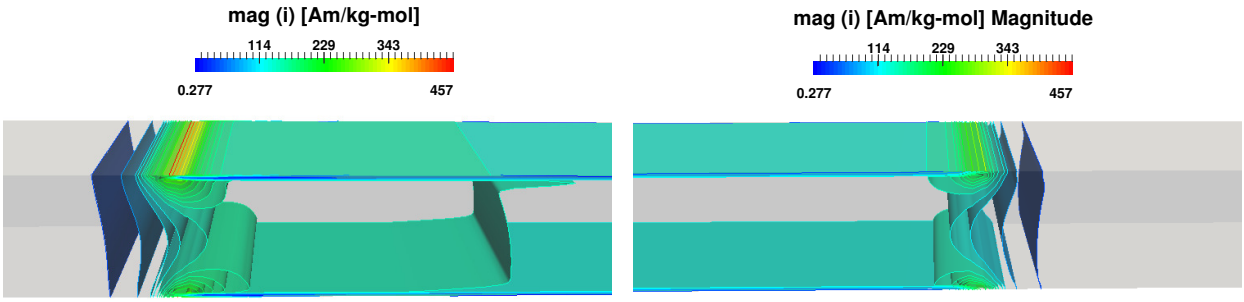

(a) Electrodes' entrance. (b) Electrodes' exit.

Figure 2.8 Contours of $|\boldsymbol{i}|$ at the extremities of the electrodes.

It is now interesting to see what happens alongside the surface of the electrodes in terms of overpotential. In Figure 2.9a, the minimum peak of $\eta_{cathode}$ is gained as soon as the electrode stars, and its value raises up to the maximum asymptotic value right at the end of the active plate. On the contrary at the anode, Figure 2.9b displays the maximum value at the entrance of the anode, and then its value rapidly decreases with an exponential behavior until the minimum is reached at the end of the electrode. The two overpotential solutions are the result of the inversion of Eq. 2.16 through the Ridders' method [49].

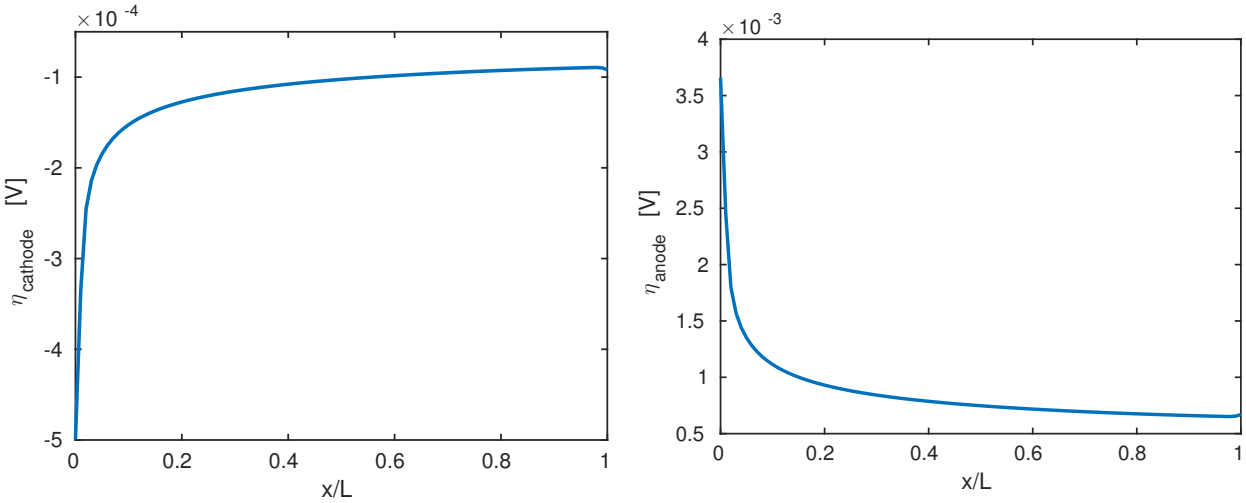

(a) Cathodic overpotential.

(b) Anodic overpotential.

Figure 2.9 Overpotential along the cathode (2.9a), and along the anode (2.9b).

Due to the very high non-linearity of Eq. 2.16, when the Ridders' method is applied to reverse the exponential function, a relaxation factor (see Table 2.4) is considered at both electrodes to improve the stability of the problem. Furthermore, to avoid any unwanted divergent solutions it is strongly suggested to bound the overpotential to any finite values. A similar exponential behavior is found in Figure 2.10. It shows the tendency of the normalized current density along the electrode. Two different test cases are plotted to point out the relevant dependency to the electrolyte velocity. The dashed curve is produced with an almost negligible velocity. Here, with the exception of the two lateral peaks, there is no appreciable variation of the current density, and the case is limited by ohmic drop. On the contrary in the red curve, the velocity becomes important and the limiting mechanisms turn out to be the convection.

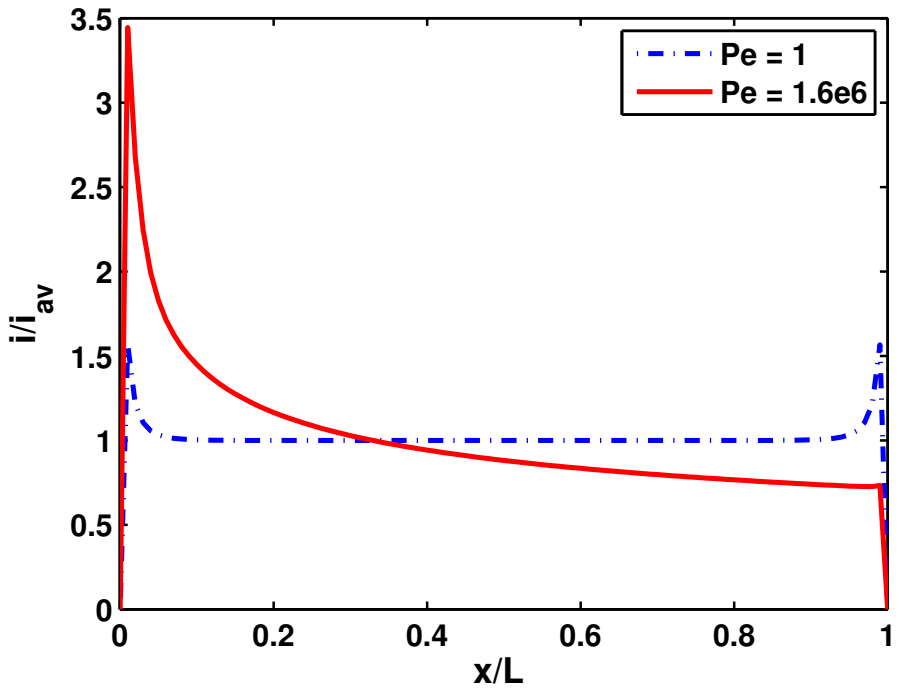

Figure 2.10 Averaged current density along the electrode at different Peclet.

These behaviors result to be consistent with the theory expressed in [42]. The limiting current density distribution is used to estimate the efficiency of the system in terms of mass transport through the Sherwood number (Eq. 2.28):

$$Sh = \frac{i_{lim} L_c}{nF C^b_{Cu^{2+}} D_{Cu^{2+}}} \qquad or \qquad Sh = \frac{k_m L_c}{D_{Cu^{2+}}} \tag{2.28}$$

Equalizing the two definitions of Sh, it is possible to calculate the mass transfer coefficient k_m as in Eq. 2.29. The result is plotted in Figure 2.11 and obviously it turns to be linearly proportional to the current density distribution but inversely dependent to the cupric ions concentration in the bulk solution. The mass transfer rate is infinite at the upstream edge of the electrode where fresh solution is brought in contact with the electrode. The current decreases by increasing x, since the solution in the diffusion layer has already been depleted by the electrode reaction further upstream [42].

$$k_m = \frac{i_{lim}}{nF C^b_{Cu^{2+}}} \tag{2.29}$$

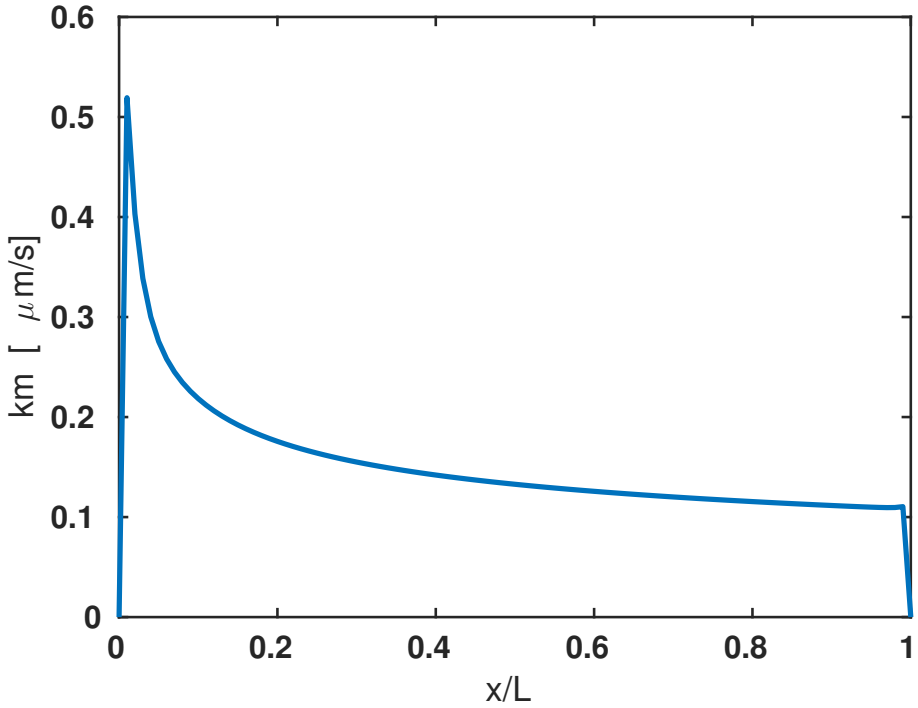

Figure 2.11 Mass transfer coefficient profile along the electrode.

The last part of this section analyzes the stretching and squeezing of the mesh to reproduce the changes in the shapes of the active plates due to the electrochemical reactions. Figure 2.12 shows the solid copper deposited at the cathode after 2000 s of simulation. It acts like a solid block, obstructing the contact between the fresh electrolyte, rich of $Y_{Cu^{2+}}$, and the metallic plate. Firstly only the left part of the cathode is affected, but later on the whole surface diminishes its production rate. The efficiency of the cell is strongly corrupted and it becomes necessary to remove the solid copper.

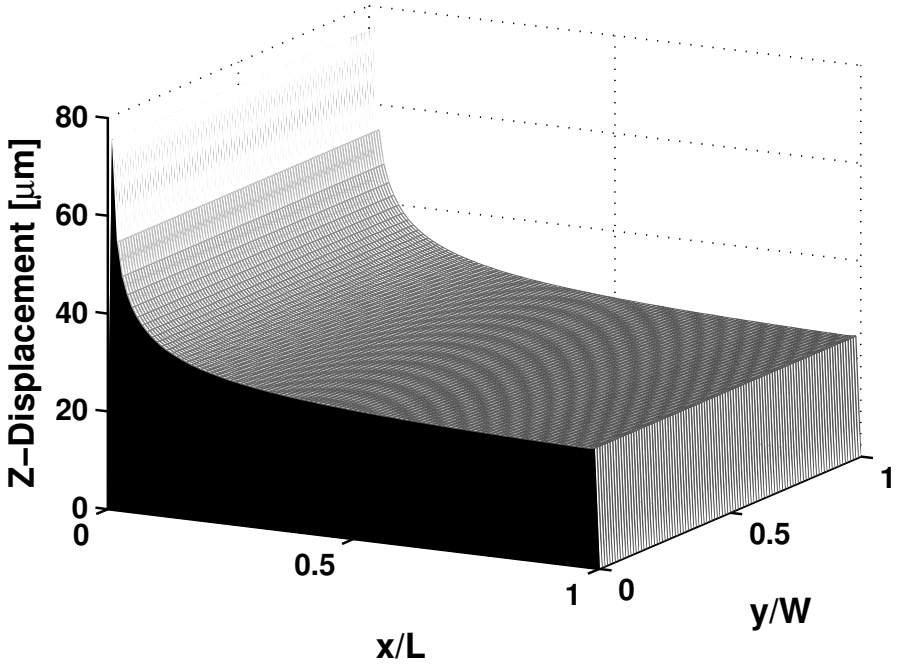

Figure 2.12 Growth of the cathode due to copper deposition.

The process at the anode is reversed, as shown in the sketches on Figure 2.13. The solid copper is turned into ions dissolving in the electrolytic solution, and causing the corrosion of the anode plate itself. A sketch of the deformed domain is presented in Figure 2.13a, and Figure 2.13b illustrates a cross-section of it, where the degradation of the anode takes place following the flow direction (from left to right).

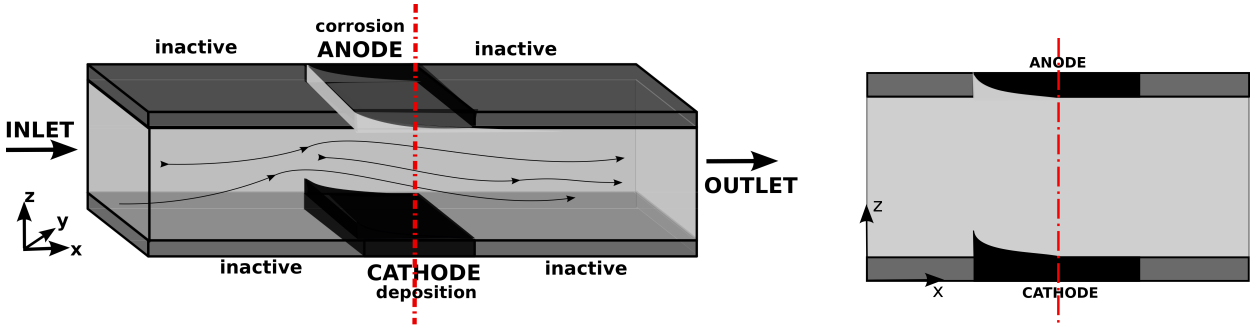

(a) 3D deformation (b) 2D deformation

Figure 2.13 Sketch of the deformed domain in 3D (2.13a), and in 2D (2.13b).

After 2000s the maximum displacement calculated is 80 μm and it is found at the entrance of the electrodes where the highest reactivity is registered, while the deposition of solid copper at the cathode is estimated to be approximately 8.8 mg. The replacement of the active plates is suggested when the efficiency of the system is reduced by approximately

50% of its initial value. Assuming an electrode thickness $th_{electrode}$ of 2 mm, the cell is maintained ideally at 100% of its efficiency for 13.8 h and after 27.7 h the electrodes need to be replaced, because half anode is corroded and the deposited copper changes the dynamics of the cell. Results are summarized in Table 2.7.

Variable	**Value**	**Units**
t	2000	s
$max\ \mathbf{d}$	80	μm
$th_{electrode}$	2	mm
$t_{at\ 100\%}$	13.8	h
$t_{at\ 50\%}$	27.7	h

Table 2.7 Estimation of the electrode's replacements.

From an industrial point of view this solver can be used to predict the amount of copper collected, the electrodes' replacement and therefore estimate the cell life-time.

Validation

The predictions of the new solver *POTisoFOAM* are compared in terms of current density at the electrode to analytic and numerical solutions, as well as the experimental data of Gerth L. [16]. The electrolyte properties, and the input parameters are the same as those shown in Table 2.2 and 2.3. The analytic solution of Leveque [42] is used for limiting current density conditions. As expressed in Eq. 2.30, the limiting current density is proportional to the copper ions concentration, and to the cubic root of the ratio U/x.

$$i_{lim} = 0.9783\,\frac{nFDC^{b}_{Cu^{2+}}}{s}\left(\frac{\langle U\rangle}{HDx}\right)^{1/3} \tag{2.30}$$

In this frame, two additional data sets are used to prove the validity of the *POTisoFOAM* solution. The first simulates the same test case with the commercial software *Comsol*, and the latter is the result of a numerical work performed by Georgiadou M. [15]. Figure 2.14 presents all the data of the normalized current density evolution along the cathode's length.

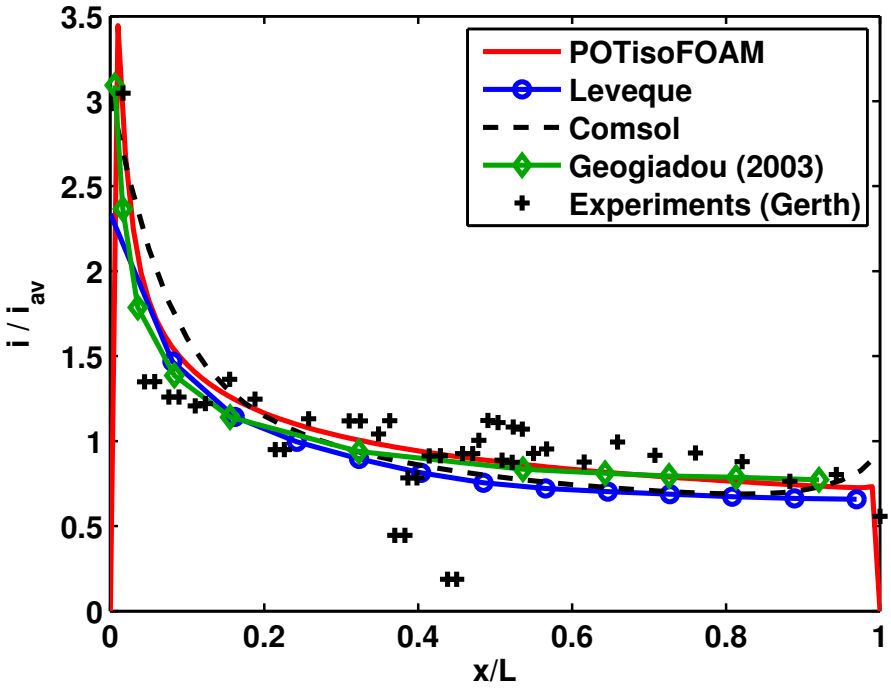

Figure 2.14 Current density comparison.

The trend is the same for all the five sets of data. The peaks at the electrode entrance exponentially decrease until the end of the plate, where the asymptotic value of approximately 0.7 is reached. Starting by analyzing Leveque' solution, it underestimates the normalized current density because of the limiting assumptions of its theory [42], for instance it does not account for the migration transport mechanism. Besides, the solution implemented in Comsol (dashed line) has a sharper transition from the peak to the asymptotic value, while at the exit of the electrode it overestimates the local current density with a small curl. These issues might be related to the discretization method used by the software, but no further investigations have been carried out about this small discrepancy. The curve of POTisoFOAM presents a slightly higher peak at the entrance of the electrode, nevertheless its trend follows the other solutions alongside with the numerical result provided by Georgiadou [15]. Finally, the last set of data presents some deviations from the other trends, specially at the center of the active plate. It could be possible that those gaps are due to some experimental errors not better identified by the authors, like the accuracy of placement of the sensors used. The entrance peak and the final asymptotic value are catch anyhow. By assuming an error band of 20% on the experimental measures the same graph is plotted in Figure 2.15 comparing exclusively the experimental results and the *POTisoFOAM* solution.

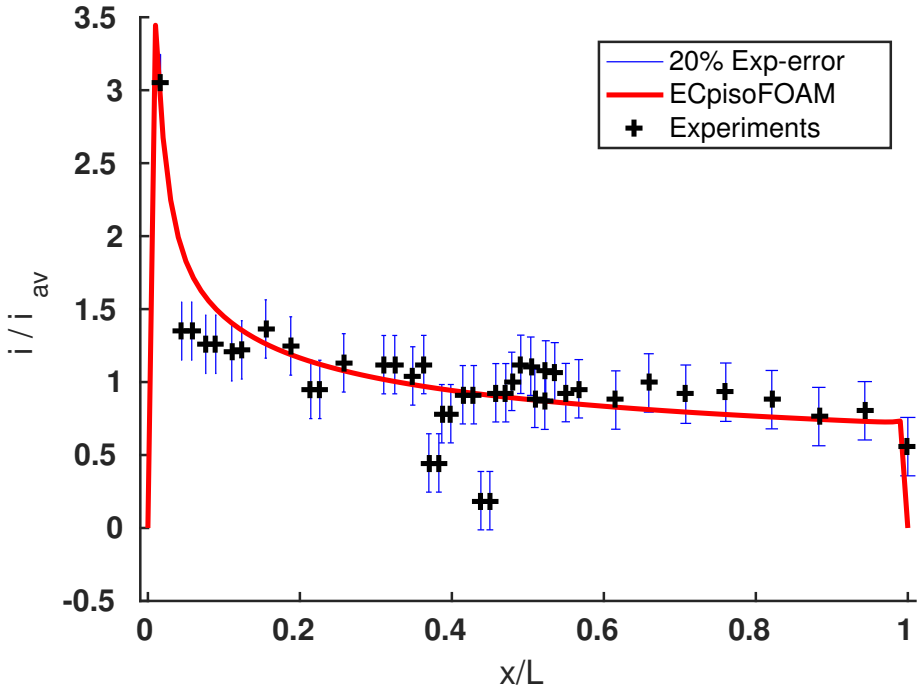

Figure 2.15 Comparison between POTisoFOAM and the experimental data assuming an error band of 20%.

The maximum relative error (Eq.2.31) is estimated to be 3.74. Before and after the middle of the electrode, the measures fall within the 20% range with two exceptions around 0.4 x/L, and other two around 0.1 x/L.

$$Err_{rel} = \left| \frac{\boldsymbol{i}_{POTisoFOAM} - \boldsymbol{i}_{Experiments}}{\boldsymbol{i}_{Experiments}} \right| \tag{2.31}$$

2.2.5 Conclusions

A numerical model has been implemented in *OpenFOAM*-2.3.1 to predict and investigate the performances of a generic electrochemical reactor. A copper depletion system in a rectangular geometry has been selected as the test case. The new solver *POTisoFOAM* makes use of the finite volume method to solve the highly coupled set of equations. *POTisoFOAM* is realized in fact with a tree architecture where each branch is easily accessible from the main body. The solver contains two predictor-corrector loops. The first takes care of the fluid-dynamics, solving pressure and velocity fields. The second predictor-corrector solves the electric potential field coupled together with the mole transport equations. Ohmic drops and gradient concentrations in the electrolytic solution contributes to the E distribution, while diffusion, convection and migration are responsible of the transport of ions in the electrolyte. The current density distribution is accurately predicted and validated

through experimental, analytic, and numerical data from the literature.
This study allows the investigation of the performances of a wider range of electrochemical systems without any strong limiting simplifications. The strength of *POTisoFOAM* is the use of the Butler-Volmer equation in its original and integral form. Few precautions though, have to be accounted for, such as the use of relaxation factors, and the bounding of the overpotential to avoid any undesired divergent solutions. For those systems where the absolute value of the electrode overpotential is relevantly high or extremely low, the solver offers also the possibility to switch respectively to the logarithmic or linear form of the BV-equation saving computational time without losing accuracy. *POTisoFOAM* is equipped with a moving mesh to reproduce the geometric deformations caused by deposition or corrosion at the active plates. This tool becomes important in the estimation of the system life-time, and can be used to evaluate the efficiency of the system and to predict the replacement time of the electrodes. In fact, improvements in the geometry have shown to have a deep impact on the efficiency of the active plates. A new design might be also including turbulence promoters, to have a more performing mixing level of the electrolytic solution. Results can be used to optimize the performances of electrochemical reactors on industrial scales.

2.2.6 Acknowledgments

The authors are very grateful to Dr. Ing. Gaetan Lantagne for his stimulating discussions and his precious comments. At the time this project started he was the director of the *Institut de Recherche d'Hydro-Québec* (IREQ). A special thanks to the Canadian company *Hydro-Québec*, and to the *NSERC* which financially supported this study. The authors thank also the *Université de Sherbrooke* for its fellowship.

2.2.7 Nomenclature

Symbol	Units	Description
$asyR$	$-$	asymptotic range of convergence
C_s	$kg\text{-}mol/m^3$	concentration of the s-th species
C_{TOT}	$kg\text{-}mol/m^3$	total electrolytic concentration
$\boldsymbol{d}$	m	point displacement vector field
d_{imp}	m	imposed point displacement
D_s	m^2/s	diffusivity of the s-th species
E	V	electric potential
E^0	V	standard electric potential
E^0_{RE}	V	standard electric potential of the reference electrode
E^{surf}	V	surface electric potential
E^∞	V	equilibrium potential
F	$A\,s/(kg\text{-}mol)$	Faraday's constant
Fs	$-$	security factor
f	m	functional
H	m	electrode's height
$\boldsymbol{i}$	$A\,m/(kg\text{-}mol)$	current density per units of C_{TOT}
$i_{0,el}$	$A\,m/(kg\text{-}mol)$	exchange current density associated to the null potential
$\boldsymbol{i}_q$	$A\,m/(kg\text{-}mol)$	current density of the q-th reaction per units of C_{TOT}
i_{lim}	$A\,m/(kg\text{-}mol)$	limiting current density
k_m	m/s	mass transfer coefficient
L	m	electrode's length

Table 2.8

Symbol	Units	Description
L_c	m	characteristic length
l	m	distance from the moving node
m	$-$	order of convergence of the solution
$\boldsymbol{N}_i$	m/s	flux of the i-th species per units of C_{TOT}
n	$-$	number of electrons exchanged
Pe	$-$	Peclet number $= UL_c/D$
p	Pa	pressure
R	$J/(kg\text{-}mol\,K)$	universal gas constant
R_{ct}	$\Omega\, kg\text{-}mol/m$	charge transfer resistance
r	$-$	grid refinement ratio
S_r	$1/s$	rate of homogeneous chemical reaction
Sh	$-$	Sherwood number
st_{sq}	$-$	stoichiometric coefficient of the s-th species
T	K	bulk temperature
t	s	time
$th_{electrode}$	m	electrode's thickness
$time_{at\,100\%}$	s	time until which the cell works at 100% of its efficiency
$time_{at\,50\%}$	s	time until which the cell works at 50% of its efficiency
$\boldsymbol{U}$	m/s	velocity
$\boldsymbol{U}_{in}$	m/s	inlet velocity
V_{el}	V	measured electrode potential
ΔE_{cell}	V	imposed cell voltage

Table 2.9

Symbol	Units	Description
Y_s^b	$-$	bulk mole fraction of the s-th species
Y_s	$-$	mole fraction of the s-th species
$Y_{s,RE}$	$-$	mole fraction of the s-th species at the reference electrode
Y_{ox}^b	$-$	bulk mole fraction of the oxidant component
Y_{ox}^{surf}	$-$	mole fraction of the oxidant component at the plate
Y_{red}^b	$-$	bulk mole fraction of the reductant component
Y_{red}^{surf}	$-$	mole fraction of the reductant component at the plate
z_s	$-$	charge number of the s-th species

Greek symbol	Units	Description
α_{sym}	$-$	symmetry factor
η	V	electrode overpotential
ν	m^2/s	kinematic viscosity
ρ	kg/m^3	solvent density

Table 2.10

CHAPTER 3

Turbulence study in an FM01-LC reactor

3.1 Avant-propos

Auteurs et affiliation:

- Giuliana Litrico: étudiante au doctorat*
- Camila B. Vieira: étudiante au post-doctorat*
- Ehsan M. Askari: étudiant au doctorat*
- Pierre Proulx: professeur*

* Université de Sherbrooke, Faculté de génie, Département de génie chimique et de génie biotechnologique

Date d'acceptation: 7 Octobre 2016

État de l'acceptation: version finale publiée

Revue: Electrochemical Society Transactions

Titre français:
Étude en régime turbulent dans un réacteur *FM01-LC*

Contribution au document:
Cet article contribue à la thèse en prenant en compte un régime turbulent et en étudiant les effets de différents modèles sur les performances d'un réacteur électrochimique à l'échelle du laboratoire

Résumé français:
On a développé, en utilisant la librairie de calcul de mécanique des fluides numérique ouverte OpenFOAM, un nouvel outil qui permet d'étudier et de prédire le comportement et d'évaluer la performance de réacteurs électrochimiques, nommé POTisoFOAM. Le modèle mathématique développé est résolu en utilisant la méthode des volumes finis et exploite la flexibilité d'OpenFOAM. Il utilise deux boucles consécutives prédicteur-correcteur qui ré-

solvent en premier les équations de Navier-Stokes moyennes selon Reynolds et en deuxième les équations associées au transport des ions et à la conservation des charges électriques. À ce système d'équations, déjà complexe, s'ajoutent les conditions aux limites fortement couplées et non-linéaires de Butler-Volmer associées à la présence de la double couche électrochimique. On obtient ainsi la distribution tertiaire de la densité de courant. L'étude présentée porte sur la simulation de l'électrodéposition du cuivre dans une cellule de type $FM01-LC$, dans laquelle les géométries d'entrée et de sortie sont censées distribuer uniformément les flux de réactif. Cependant il est montré que la géométrie d'entrée crée des zones ayant des forts gradients de vitesse et provoque un régime d'écoulement en grande partie turbulent même pour des nombres de Reynolds relativement bas.

Note:
À la suite des corrections demandées par les membres du jury, le contenu de cet article diffère de celui qui a été accepté

3.2 Investigation of the effects of turbulence on a FM01-LC reactor

A new solver named POTisoFOAM is presented to predict and investigate the performance of electrochemical reactors. Its mathematical model is developed and implemented through finite volume methods and exploits the flexibility of the open source package OpenFOAM. The solver consists of two consecutive predictor-corrector loops. The first solves the pressure and velocity fields, while the second handles the ions transport and current conservation. The equations' system is further complicated by means of the non linear Buttler-Volmer boundary conditions. Despite the strong coupling between the charged ions and the electric potential, the reconstruction of the tertiary current density distribution is achieved. This study simulates the electrodeposition of copper in a *FM01-LC* cell, where the design of the entrance and exit manifolds create zones with strong velocity gradients, and initiate a turbulent regime inside the reactor.

3.2.1 Introduction

A parallel plate electrochemical reactor (PPER) is a device where two slabs are facing each other, and an electrolytic solution flows in between carrying reactants and products. The voltage difference imposed at the plates is responsible for the creation of the electric field. It facilitates chemical reactions, species from one half-cell lose electrons by oxidation, while species from the other half-cell gain electrodes by reduction [43]. In spite of its structural simplicity, the design of a PPER turns out to be a hard task. Studies demonstrated that improvements in the inlet/outlet geometry lead to more uniform flow patterns promoting a homogeneous distribution of current density, and electric potential, alongside with a more even consumption of the electrode surfaces and an increase of the system life-time [7, 13, 63, 70]. In short, designers ensure that the reaction occurs with the highest efficiency towards the desired output product, requiring the cheapest operative solution. In order to achieve so, this study provides a mathematical model to investigate the performances of a PPER, analyze the critical and challenging coupling, and eventually predict its operative conditions.

3.2.2 FM01-LC

Among the parallel plate electrochemical reactors, the FM01-LC is the most common cell for continuous flows thanks to its validated technology and its versatile electrolyte. It is used in several industrial applications worldwide such as electro-synthesis [56], water treatment [8, 31, 40, 41] and various energy storage process. The *FM01-LC* is the laboratory scale reactor of the industrial cell *FM21-SP* (2.1 m^2) mostly used for the chlor-alkali production by the INEOS Chlor-Chemicals company [20, 68]. The prototype has instead a projected area of only 64 cm^2; it measures 16 cm in length, 4 cm in width and 1.1 cm as the gap between the electrodes [66]. The design is provided of a plate-and-frame filter-press configuration. Electrodes, spacers, ion-exchange membranes and gasket are compressed between two electrically insulated end plates [67]. Figure 3.1 shows a scheme of the *FM01-LC* cell.

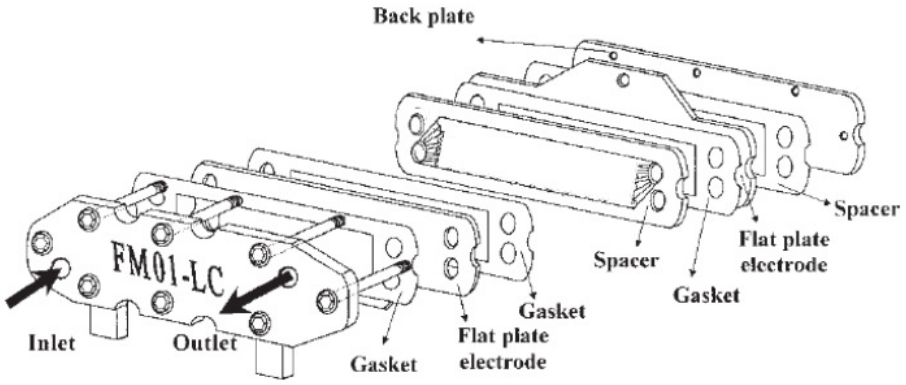

Figure 3.1 Exploded view of the *FM01-LC* laboratory cell electrolyzer [67].

The peculiar structure of its manifolds at the entrance and at the exit of the active channel provokes perturbations which can degenerate into turbulence regimes, affecting the fluid-dynamics, and as a consequence the performances of the reactor. Different flow patterns mean also different mass transfer rate of the electro-active species, different current density and potential distributions [54]. Several design modifications have been analyzed to improve the reactor performance [7, 13, 63], but the simultaneous occurrence of the phenomena results in an intricate scenario difficult to reproduce. In order to handle the high complexity of the problem, and in particular the promoted turbulence, this work is entirely built by means of open source software, from the geometry design, to meshing, and coding, allowing maximum flexibility and accessibility. The mathematical model is implemented in OpenFOAM (*O*pen-source *F*ield *O*peration *A*nd *M*anipulation). The software, mostly used for computational fluid-dynamics (CFD), allows transversal links between different domains interconnecting physical process [9]. This choice permits to

built a multi-disciplinary adaptable solver where various scenario can be reproduced, and solutions are achievable for a wider range of applications.

3.2.3 POTisoFOAM: Mathematical and numerical formulation

POTisoFOAM stands for *POT*ential - P*iso* - FOAM, and it recalls the name of the two main predictor-corrector loops that constitute the solver: the first handles the fluid-dynamics part (Piso-loop) solving continuity, momentum, and turbulence equations, while the second takes care of the electrochemistry (POTential-loop) solving the potential field simultaneously with the mole transport equations. A set of non-linear boundary conditions closes the system. In the next subsection the main structure of the solver *POTisoFOAM* is presented.

Fluid-dynamics

The hydrodynamic behavior is investigated by solving the continuity Eq. 3.1, and the momentum equation Eq. 3.2, in a predictor-corrector loop explained below:

$$\nabla \cdot \boldsymbol{U} = 0 \tag{3.1}$$

$$\frac{\partial \boldsymbol{U}}{\partial t} + \boldsymbol{U} \cdot \nabla \boldsymbol{U} = -\frac{\nabla P}{\rho} + \nu \nabla^2 \boldsymbol{U} - \nabla \cdot \boldsymbol{R} \tag{3.2}$$

where $\boldsymbol{U}$ is the mean velocity, ρ and ν the average density and kinematic viscosity of the electrolytic solution, P the pressure, and $\boldsymbol{R}$ the averaged Reynolds stresses. The latter are linearly related to the strain rate tensor, according to Boussinesq hypothesis [6]. They are described in Eq. 3.3, in which ν_T is the turbulent kinetic viscosity, k the turbulent kinetic energy, and δ_{ij} is the Kronecker delta.

$$-\boldsymbol{R} = \nu_T \left(\frac{\partial U_i}{\partial x_j} + \frac{\partial U_j}{\partial x_i} \right) - \frac{2}{3} k \delta_{ij} \tag{3.3}$$

A first guess on pressure is used in Eq. 3.2 to estimate a non-divergence-free velocity. The coefficients of the resulting velocity matrix are then split into a diagonal and a non-diagonal matrix (*piso* - Pressure Implicit with Splitting of Operators). The predicted velocity is used to calculate the new value of pressure, which in turn corrects the non-diagonal matrix

and force the updated velocity to be divergence-free. The accuracy of this routine is user defined and can be chosen by selecting a specific number of loops or a desired tolerance [12, 21–23, 45].

Turbulence

The particular shapes of the entrance and exit manifolds, create flow patterns with different velocities that sliding on top of each other form eddies increasing in size. Therefore, the investigation of the developed turbulence becomes of utmost importance in the dynamics of the cell. In this study two well known turbulent models are used and discussed: k-ε and SST-k-ω model. The $k-\varepsilon$ model provides the turbulent kinetic energy k, and the turbulent dissipation rate ε, by solving the transport equations Eq. 3.4 and 3.5 [26].

$$\frac{\partial k}{\partial t} + \boldsymbol{U} \cdot \nabla k = \nabla \cdot \left(\nu + \frac{\nu_T}{\sigma_k} \nabla k \right) + P_{prod} - \varepsilon \tag{3.4}$$

$$\frac{\partial \varepsilon}{\partial t} + \boldsymbol{U} \cdot \nabla \varepsilon = \nabla \cdot \left(\nu + \frac{\nu_T}{\sigma_\varepsilon} \nabla \varepsilon \right) + C_{\varepsilon,1} \frac{P_{prod} \varepsilon}{k} - C_{\varepsilon,2} \frac{\varepsilon^2}{k} \tag{3.5}$$

The equations are written in accordance to *OpenFOAM* implementation, where P_{prod} is defined as in Eq. 3.6

$$P_{prod} = -\boldsymbol{R} \nabla \cdot \boldsymbol{U} \tag{3.6}$$

The values of the constants σ_k, σ_ε, $C_{\varepsilon,1}$, and $C_{\varepsilon,2}$ are shown in Table 3.1. An additional extra constant C_μ is needed in Eq. 3.7 to estimate the turbulent kinematic viscosity ν_T:

$$\nu_T = C_\mu \frac{k^2}{\varepsilon} \tag{3.7}$$

σ_k	σ_ε	$C_{\varepsilon,1}$	$C_{\varepsilon,2}$	C_μ
1	1.3	1.44	1.92	0.09

Table 3.1 k-ε: model's constants.

The method discussed above belongs to the RANS family, **R**eynolds **A**veraged **N**avier & **S**tokes equations, where each variable is decomposed in its averaged and its fluctuating part. During the simulation, this allows to store only the significant components of each variable with a significant decrease on the computational costs. Moreover, the

computational time is further reduced thanks to the special treatment reserved to walls, where the shape of the velocity profile can be retrieved by placing the first cell inside the logarithmic layer. Indeed, in the region closest to the wall, called laminar sub-layer, the viscosity controls the normal momentum, and the non dimensional velocity U_n^+ follows Eq. 3.8. Farther from the wall, the profile falls in the so-called logarithm region where turbulence controls the normal transport of momentum, and U_n^+ obeys Eq. 3.9. The use of wall functions permits to predict the steep changes between the two regimes without any additional mesh refinements [39]. Figure 3.2 shows the near wall treatment.

$$U_n^+ = u_\tau \frac{\delta}{\nu} \tag{3.8}$$

$$U_n^+ = \frac{1}{K}\, ln(\delta^+) + B \tag{3.9}$$

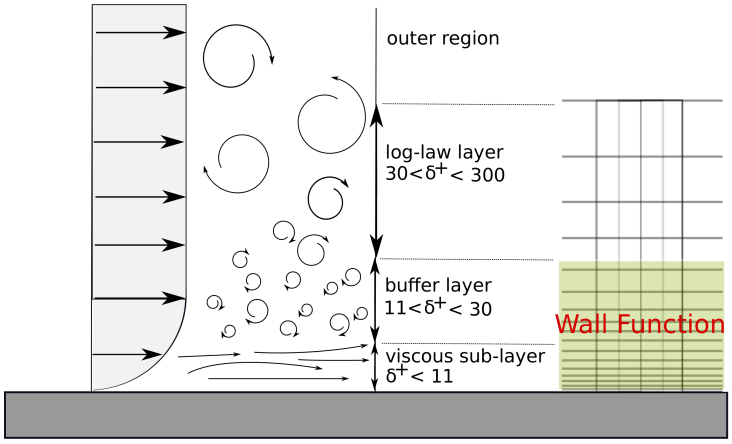

Figure 3.2 k-ε model: near wall treatment.

where u_τ is the friction velocity, δ the distance perpendicular to the wall, and δ^+ its non dimensional form ($=\delta u_\tau/\nu$), $K = 0.41$ is a constant same as $B = 5.2$. The model k-ε is widely used thanks to its easy convergence and its robustness, specially far away from walls . A valid alternative to this is the SST-k-ω model. It belongs to the RANS family, and it acts like a low Reynolds model close to walls, and like a high Reynolds model far from walls, meaning that it correctly reproduces the limiting behaviors of various flow quantities as the distance to the wall approaches zero, without any extra damping functions. For these reasons in this work no wall functions are employed when the SST-k-ω is used. Additionally, the SST formulation switches to a k-ε behavior in the free-stream and thereby prevents the model to be too sensitive to the inlet turbulence properties [34, 35]. The model is a two-equation model where k and the turbulence frequency ω are solved through Eq. 3.10 and 3.11

$$\frac{\partial k}{\partial t} + \boldsymbol{U} \cdot \nabla k = \nabla \cdot \left(\nu + \frac{\nu_T}{\sigma'_k} \nabla k \right) + P'_{prod} - \beta^* \omega k \tag{3.10}$$

$$\frac{\partial \omega}{\partial t} + \boldsymbol{U} \cdot \nabla \omega = \nabla \cdot \left(\nu + \frac{\nu_T}{\sigma_\omega} \nabla \omega \right) + \alpha_\omega S^2 - \beta \omega^2 + 2\left(1 - F_1\right) \frac{\sigma_{\omega 2}}{\omega} \nabla k \nabla \omega \tag{3.11}$$

The model is equipped with a blending function, F_1. It allows the model to behave like k-ω close to the wall, $F_1 = 1$, and like k-ε away from it, $F_1 = 0$. All the constants follow the blend form of Γ in Eq. 3.12 [37], and are regrouped in Table 3.2.

$$\Gamma = \Gamma_1 F_1 + \Gamma_2 (1 - F_1) \tag{3.12}$$

	β^*	β	α_ω	σ'_k	σ_w
Γ_1	0.09	3/40	5/9	0.85	0.5
Γ_2	0.09	0.0828	0.44	1	0.856

Table 3.2 *SST-k-ω*: model's constants.

Furthermore the modeling of turbulent eddy viscosity ν_T follows the form in Eq. 3.13

$$\nu_T = \frac{a_\omega K}{max\left(a_\omega \omega\,,\, S F_2\right)} \tag{3.13}$$

in which $a_\omega = 0.31$, S is the local strain rate [46], and F_2 is another blending function described by Eq. 3.14 [36]

$$F_2 = tgh\left\{ \left[max\left(\frac{2\sqrt{k}}{\beta^* \omega \delta}\,,\, \frac{500\nu}{\delta^2 \omega} \right) \right]^2 \right\} \tag{3.14}$$

As said before, only significant components are stored through a RANS simulation; but the substantial increase in computer power of the last decades, allows to achieve considerable progresses in the development of more accurate turbulence models. Among these, Large Eddy Simulation (LES) are found. *LES* is used here in its one equation eddy viscosity model for incompressible flows, where the eddy viscosity Sub Grid Scales (SGS) are modeled through a balance equation to describe the transport of k. Hence Eq. 3.15, and Eq. 3.16:

$$\frac{\partial k}{\partial t} + \boldsymbol{U} \cdot \nabla k = \nabla \cdot \left(\nu_{eff} \nabla k \right) - B_{LES} D_{LES} - C_e \frac{k^{3/2}}{\Delta} \tag{3.15}$$

$$\nu_{eff} = \nu_{sgs} + \nu \qquad , \qquad \nu_{sgs} = C_k\sqrt{k}\Delta \tag{3.16}$$

where $B_{LES} = 2/3kI - 2\nu_{sgs}\ dev(D_{LES})$, while $D_{LES} = symm\,(\nabla \boldsymbol{U})$, and the two constants are equal to $C_e = 1.048$ and $C_k = 0.094$. The filter separating small scales from large scales Δ is modeled as the cubic root of the volume cell. Indeed LES makes use of the assumption that large turbulent scales are the only ones to be fully resolved, while smaller scales are universal and sub-grid models can be used instead. This makes LES a good compromise between the high computational cost of more exact solutions, like Direct Numerical Simulation (DNS), and the lack of information in the variables' fluctuations of RANS [48, 74]. Nevertheless the full LES formulation is not further explained, because in this paper it is used only to identify the target velocity solution. Due of the generality and the well known validity of these turbulence models, the author decides to refer to [37, 47, 71] for any further detailed explanation.

Electrochemistry

The electric potential field E, and the mole fractions Y are here solved. The electric potential at the previous time step $^{ts-1}$ is required to initialize the POTential-loop, solve the ions transport equations, and predict the mole fraction of each $*$-th species. Once all the mole fractions are retrieved Eq. 3.17, they are employed in the current conservation equation to update the value of E^{ts}, Eq. 3.18. The new electric potential is finally used in Eq.3.19 to keep the value of each mole fraction up to date.

$$E^{ts-1}$$

$$\downarrow$$

$$\partial_t Y^{ts}_{s*} + \nabla\cdot(\boldsymbol{U}, Y^{ts}_{s*}) - \nabla^2(D_{eff}, Y^{ts}_{s*}) = a_1\nabla^2(Y^{ts}_{s*}, E^{ts-1}) \tag{3.17}$$

$$\downarrow \quad Y^{ts}_{s*}$$

$$a_2\nabla^2(Y^{ts}_{s*}, E^{ts}_{*}) + a_3\nabla^2(D_{eff}, Y^{ts}_{s*}) = 0 \tag{3.18}$$

$$\downarrow \quad E^{ts}$$

$$\partial_t Y^{ts}_{s} + \nabla\cdot(\boldsymbol{U}, Y^{ts}_{s}) - \nabla^2(D_{eff}, Y^{ts}_{s}) = a_1\nabla^2(Y^{ts}_{s}, E^{ts}_{*}) \tag{3.19}$$

$$\downarrow$$

$$Y^{ts}_{s},\ E^{ts}$$

In the scheme above the apexes refer to the time step, $*$ indicates the guessed values, a_1, a_2, and a_3 are constant coefficients. The term D_{eff} is the effective diffusion coefficient of the electrolytic solution, and it sums up the molecular diffusivity and the turbulent diffusion

of the flow. It is worth mentioning that the transport Equations account for convection, diffusion and migration. Meanwhile, the current conservation consists of the ohmic drop across the cell, and the concentration potential. The latter is often neglected in presence of diluted solutions where reactants' concentrations play an important role just close to the electrodes. In this work it is decided not to use this simplification to maintain the generality of the case. The result is a very strong challenging coupling between the electric potential and the mole fractions. The number of species solved in this POTential-loop are N-2, being N the total number of species considered in the solution. The two missing equations are the total mole fraction conservation Eq.3.20 and the electroneutrality of the solution Eq.3.21, where z_s is the charge number of the species.

$$\sum_s Y_s = 1 \tag{3.20}$$

$$\sum_s z_s Y_s = 0 \tag{3.21}$$

Electrode kinetics

The coupling between the electric potential and the mole fractions of the species gets stronger at the boundaries. Here, $\boldsymbol{N}_s$ the normal flux of ions taking part to the surface's reaction is expressed as a function of the normal current density $\boldsymbol{i}_q$ in Eq.3.22 :

$$\boldsymbol{N}_s \cdot \boldsymbol{n} = \pm \sum_s \frac{s_{sq} \boldsymbol{i}_q \cdot \boldsymbol{n}}{n_q F} \tag{3.22}$$

in which s_{sq} is the stoichiometric coefficient of the s-th active species in the q-th reaction, n_q the number of electrons exchanged per reaction, while the sign $\pm$ depends whether the reaction is occurring at the anode or at the cathode. In both cases to model the kinetics of the electrodes, the term $\boldsymbol{i}_q$ needs to be further developed. The current density transported by the active ions is indeed a function of the electrode's overpotential (Eq.3.23):

$$\boldsymbol{i}_q \cdot \boldsymbol{n} = i_0 \left[exp\left\{ \alpha \frac{n_q F}{RT} \eta \right\} - exp\left\{ -(1-\alpha) \frac{n_q F}{RT} \eta \right\} \right] \tag{3.23}$$

where i_0 is the exchange current density associated to the null potential, α is the symmetry factor also known as the charge transfer coefficient, F the Faraday's constant, R the universal gas constant, T the temperature of the electrolyte and finally η the electrode's overpotential. Equation 3.23 is also known as the Butler-Volmer equation [5, 42, 66], and its exponential nature complicates even more the coupling. At the initial time step the

value of η is unknown. Thanks to Eqs. 3.17, 3.18 and 3.19, the variable Y^n and E^n are retrieved, the product $\boldsymbol{i}_q \cdot \boldsymbol{n}$ is estimated and substituted into Eq. 3.23. The Butler-Volmer equation is then inverted by means of the Ridders' method and the electrode's overpotential is recovered. The Ridders' method is a non-linear regula-falsi method, where the originally non linear function $f(x)$ is transformed (Fig. 3.3) into a linear function $g(x)$ whose roots are (η) [49]. The method also requires that the two initial values ($x1$ and $x2$) are on different sides of the root to be sought.

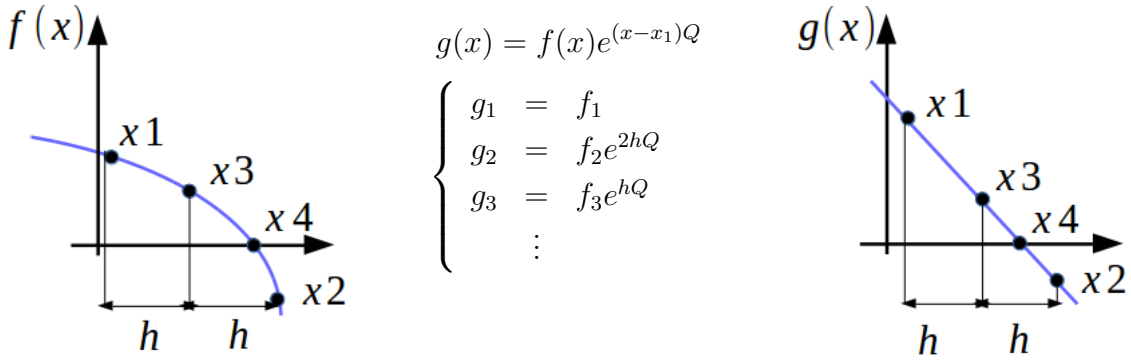

Figure 3.3 Ridders' method: Transformation.

The electric potential on the active plates E_{el} can now be updated by subtracting the new value of the overpotential and the calculated equilibrium potential E^{∞} (here estimated as a fixed value) from the measured electrode potential V_{el}.

$$E^{surf} = V_{el} - \eta - E^{\infty} \tag{3.24}$$

3.2.4 Simulation set up

In this study, the prototype FM01-LC is chosen. Its CAD model has been realized with the geometry module of *Salome 7.4* (open-source integration platform for numerical simulations). Figure 3.4 provides a 3D sketch, and the dimensions of the rectangular channel.

As it can be noticed, the flow at the inlet and at the outlet of the channel is perpendicular to the plates. This design allows to pack in series multiple reactors increasing the overall productivity in a large scale plant. Another characteristic of this design is the manifold used at the entrance and at the exit of the reactive channel. The flow entering from the inlet cylinder, is re-distributed in five conducts with different lengths, causing an uneven flow at the entrance of the rectangular channel. Figure 3.5 gives a top view of the entrance manifold, whose height is 3 mm smaller than the reactive chamber.

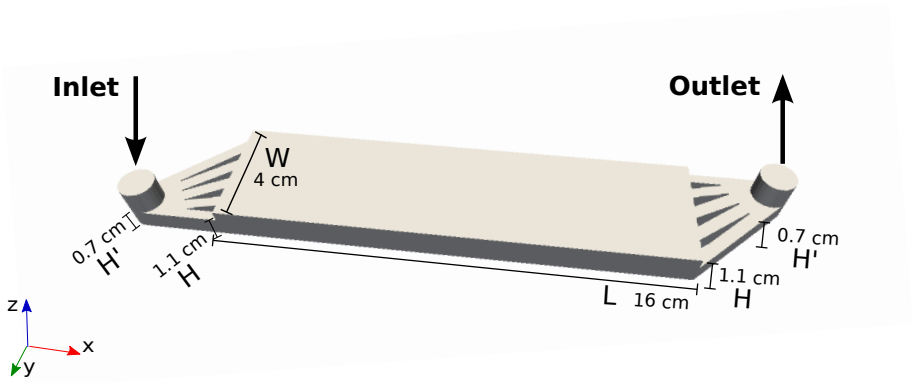

Figure 3.4 Geometry of the FM01-LC prototype.

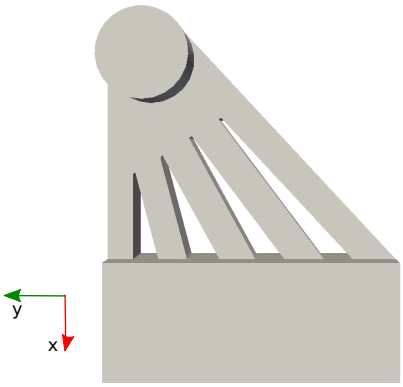

Figure 3.5 Top view of the entrance manifold.

In order to mesh this geometry, *SnappyHexMesh* has been used. It is a tool embedded in the OpenFOAM package and helps creating a structured grid out of a given geometry. Table 3.3 shows the main mesh's characteristics used with the three different turbulence models. The k-ε and SST-k-ω meshes have approximately the same number of cells in the rectangular reactive channel. The first makes use of wall functions, while the second has three refinement levels with an expansion ratio of 1.1 to integrate the bulk solution up to the walls. The LES mesh presents a much more refined grid, where most of the non-orthogonality is concentrated at the entrance and exit manifolds. A zoom-in of the k-ε exit manifold's mesh is reported in Figure 3.6.

The solver, is implemented using a finite volume formulation. All the first order derivatives in time are discretized using an implicit Euler method, and all the gradients follow the Gauss linear discretization. Particular care is used for the convection term discretized by means of the Gauss limited linear scheme. In the results section is shown that the more common Gauss upwind discretization is not appropriate for this test-case. The

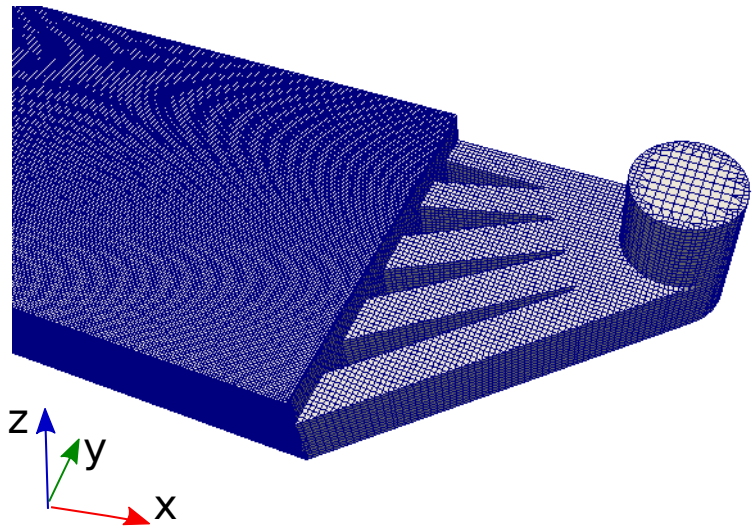

Figure 3.6 k-ε model: zoom in of the exit manifold mesh.

laplacians are modeled with a Gauss linear corrected scheme, to help reducing the mesh non-orthogonality in the manifold areas. Relaxation factors on pressure, velocity and mole fraction are used to make sure that the matrix coefficients are diagonally dominant, and encourage a faster convergence.

	k-ε	SST-k-ω	LES
equations	Eqs. 3.4 - 3.5	Eqs. 3.10 - 3.11	Eq. 3.15
tot cells	213,175	677,832	3,922,896
hexahedra cells	189,580	590,034	3,905,930
prisms cells	/	6780	15,946
polyhedra cells	23,595	81,018	1020
aspect ratio	1	4.1	8
non-orthogonality	10	10	5
max skewness	0.3	2.8	3.7
extra info	WF	no WF	$\Delta = (V_c)^{1/3}$
y^+ average	14.18	5.3	1.2

Table 3.3 Meshes properties: k-ε, SST-k-ω, LES.

The prototype FM01-LC is used in this work to simulate the electroplating of copper. The electrolytic diluted solution consists of $18\,mM\ CuSO_4 + 1M\ H_2SO_4$ and both the electrodes are made of copper. The cathode is considered the working electrode where the ions Cu^{2+} capture the electrons and deposit on the plate, ready to be removed. At the anodic counter electrode the copper is oxidized, and dissolves releasing ions as expressed

in Eq. 3.25. For the sake of simplicity the ΔE_{cell} is equal to the cathode initial potential, while the anodic potential is set to zero.

$$Cu^{2+} + 2e^{-} \underset{anode}{\overset{cathode}{\rightleftharpoons}} Cu(s) \tag{3.25}$$

3.2.5 Results and discussions

In this section the results obtained using *POTisoFOAM* are presented and discussed. The solver has been previously validated versus analytic, experimental, and numerical data for the limiting current density distribution in a laminar case on a rectangular geometry, including only fluid-dynamics and electrochemical phenomena. The validation has provided excellent agreement [29].

Fluid-dynamics

The hydrodynamic results are presented below. Figure 3.7 indicates the locations of seven cross-sections perpendicular to the flow which allow to investigate averaged velocity contours shown in Figure 3.8

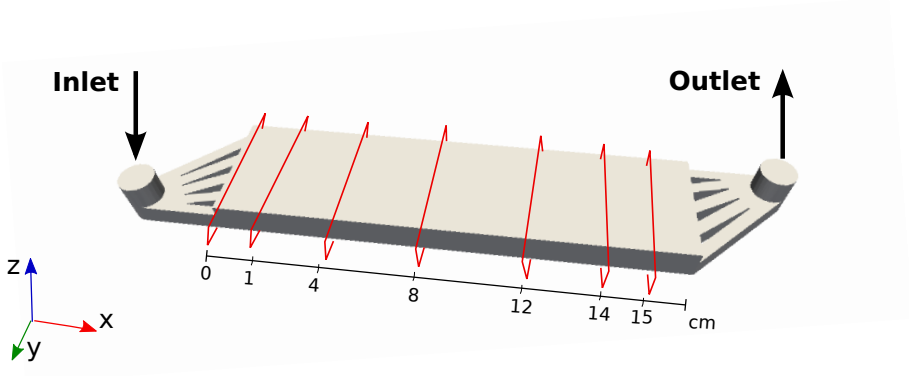

Figure 3.7 Locations of the cross-sections where the velocity is investigated.

In Figure 3.8 the cross-section at the entrance of the channel, $x = 0\ cm$, shows the presence of five jets. The maximum magnitude velocity located at the bottom, comes from the shortest entrance channel where the flow is not deviated and goes straightforward to the main reactive chamber. The difference in height between the paws and the reactive channel, see Figure 3.4, improves the mixing of the solution, and produces a zero-velocity zone in blue on the right side of this cross-section. In the second cross-section at $x = 1\ cm$, this zero velocity zone is reduced and the shapes of the inlet jets become blurred. At $x = 4\ cm$ and $x = 8\ cm$, the flow can be already considered fully developed, since the jets can be barely distinguished, and those at the extremities of the y-axes have almost

halved their strength. The fifth contour at $x = 12\ cm$, introduces the presence of a higher velocity magnitude for small values of y. The same trend is depicted in the cross-section at $x = 14\ cm$, where the velocity keeps increasing. At $x = 15\ cm$, the effects of the exit manifold become more evident, and new concentrated higher velocity zones appear.

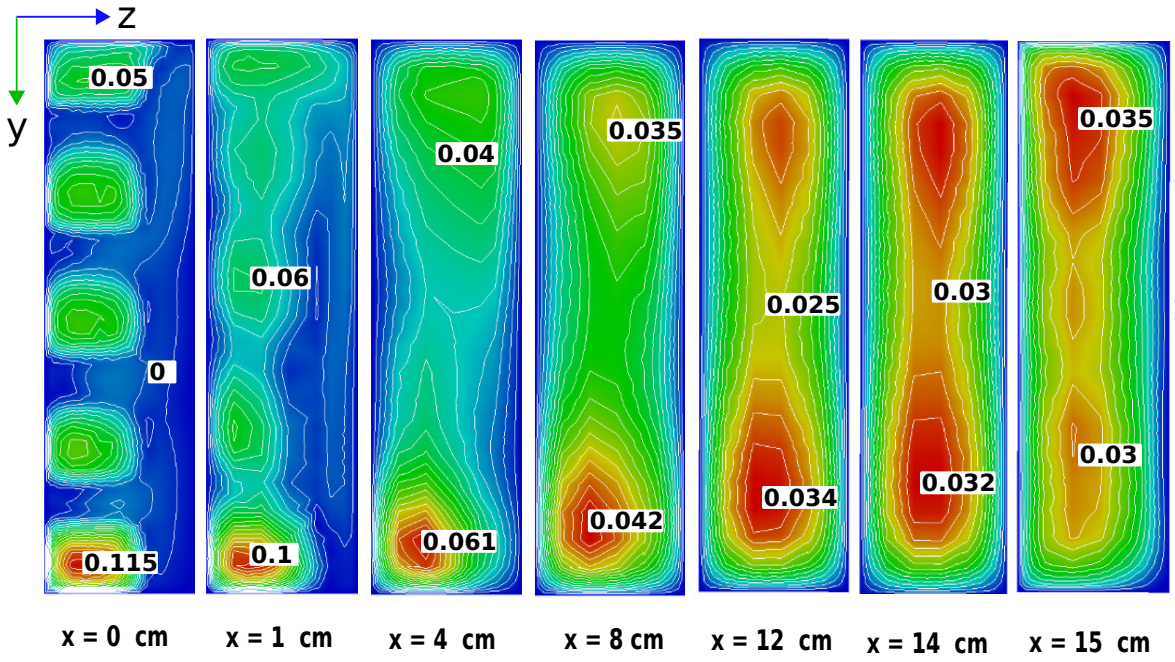

Figure 3.8 Contours of the averaged magnitude velocity in m/s, for Re=1000, at different distances from the entrance.

It is clear that the effects of the entrance and exit manifolds have an impact on the flow patterns in the reactor. Therefore, it becomes interesting to see how the velocity profile looks like close to the entrance. A line extracted perpendicularly to the flow (Figure 3.9a) shows the axial velocity profile in Figure 3.9b. Results are obtained at a Reynolds number of 4845, and are compared with a previously validated numerical work with a similar grid size using the k-ε turbulence model [53]. The averaged profiles show a good agreement for the smallest values of y, and a poor overlapping immediately close to it. The jets at $y/W = 0.25$ and $y/W = 0.5$ well describe the axial velocity component, but as soon as the ratio y/W overcomes half cell, a more important mismatch is noted. This work ($POTisoFOAM$) underestimates the fourth peak, and presents an overshooting in the last one (Figure 3.9a). The differences between the predictions could be explained by the fact that the details of the geometry were not provided by [53], therefore the simulated manifold's geometries may have small differences.

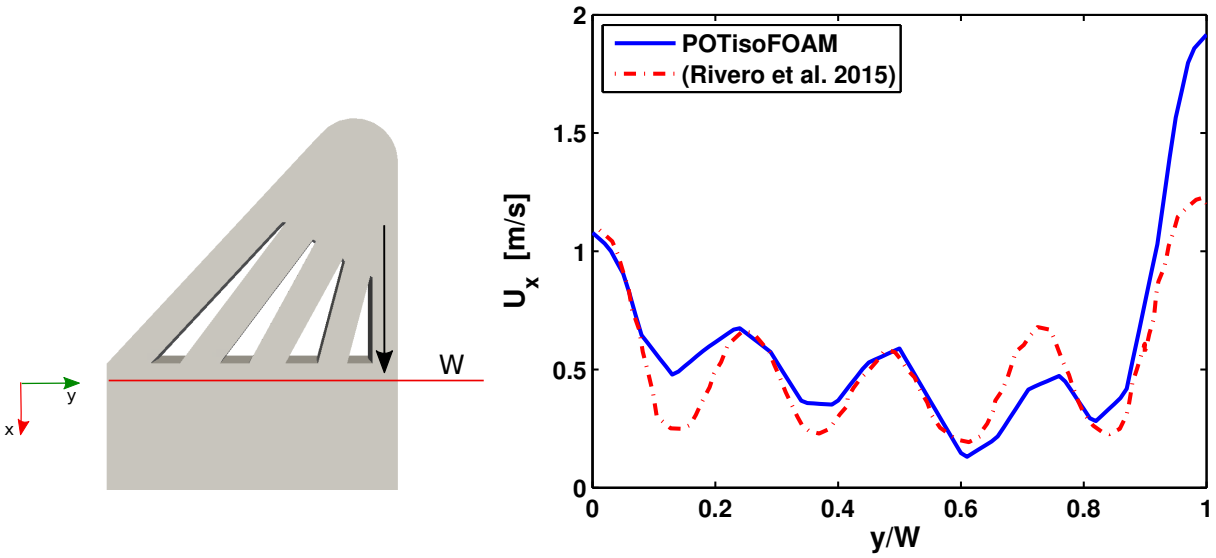

(a) Location of the profiles.

(b) Averaged axial velocity profiles.

Figure 3.9 k-ε model: averaged axial velocity profiles comparison at the entrance, Re=4845.

Turbulence

This section presents the results of the two RANS models here implemented. The LES simulation, as previously mentioned, is only used as a validation standard, and later on the two RANS models are compared with it. Figure 3.10 shows an instantaneous magnitude of the velocity on a horizontal slice placed in the middle of the reactor.

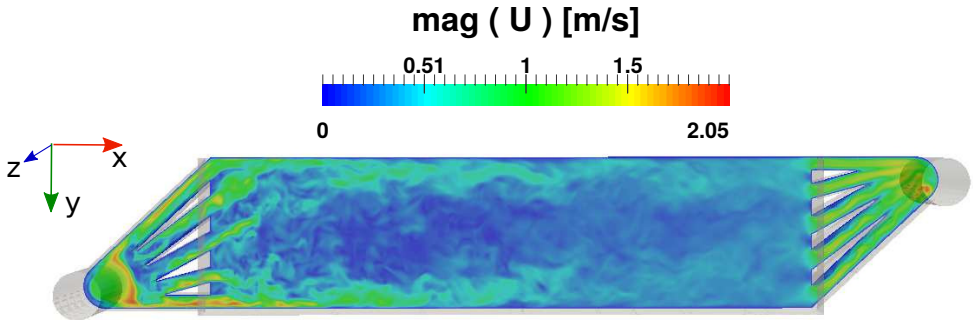

Figure 3.10 *LES* model: instantaneous magnitude velocity on a horizontal slice placed in the middle of the reactor, $Re = 4845$.

The effect of the manifold geometry on the flow patterns is not negligible, specially close to the entrance as shown in Figure 3.11, where the flow goes from left to right. The streamlines of the electrolyte are obtained by means of the k-ε model, and they are mapped with the mean axial velocity U_x. Figures 3.11a and 3.11b give a top and bottom view of the reactor. The most diagonal entrance channel produces a slow jet that first bounces on the later edge of the reactor with an angle of almost 45^o, and then rolls on top of the other jets, as it can be seen from its top view. The three jets close by have a higher velocity which allow them to impact the reactor's edge farther from the entrance and with smaller angles. The velocity peak is found between the straight jet and its neighbor. This pushes the straight jet until the end of the reactive channel without any contact with the lateral side of the rector. The second half of the reactor appears to have lower velocity, and less vorticity than the first half.

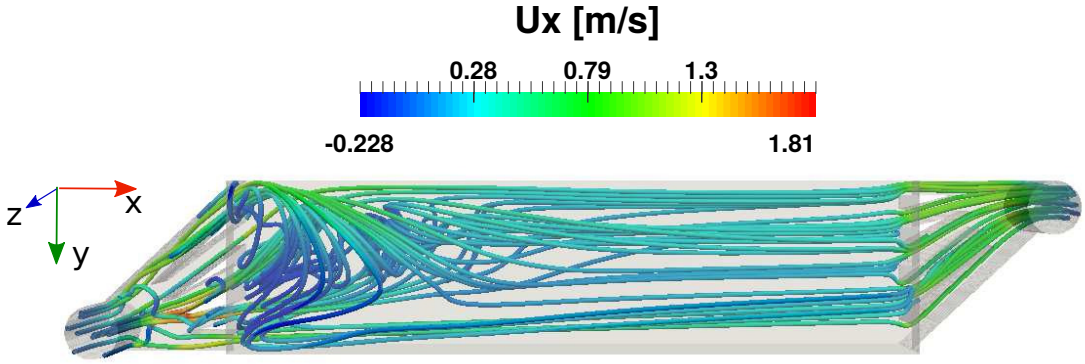

(a) Top view.

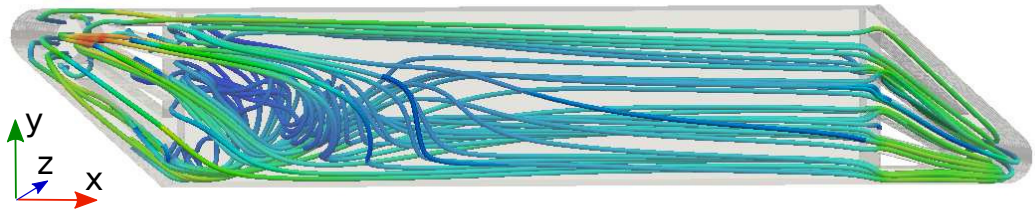

(b) Bottom view.

Figure 3.11 k-ε model: averaged streamlines of the electrolyte mapped with the mean axial velocity U_x, top view (3.11a) and bottom view (3.11b), $Re = 4845$.

To have a better understanding of the turbulence involved in the process, Figure 3.12 shows a slice extrapolated from the middle of the reactor where the contours of the turbulent kinetic viscosity are plotted. The ν_T is here calculated through the SST-k-ω modeling. As said before, most of the turbulence is concentrated on the first half of the reactor. The turbulent kinetic viscosity presents darker shades of red along the paths of the shortest entrance channel and its neighbor. The two form a recirculating zone right in the middle of the reactor, that drags alongside the rest of the fluid downstream. A third smaller orange shade is shown close to the second jet from the top, and it merges with the other two immediately after its formation. The exit manifold presents a blue zone of basically zero ν_T along the jets, and a lighter green area where the velocity changes sharply its direction.

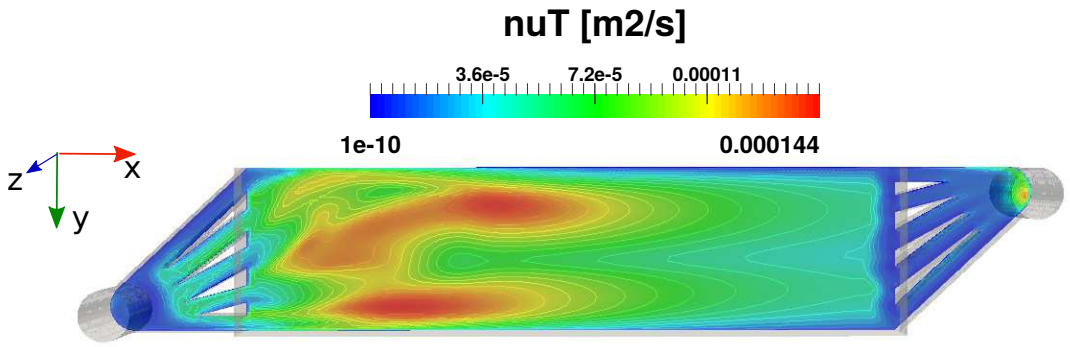

Figure 3.12 SST-k-ω model: contours of the mean turbulent kinetic viscosity in the middle of the reactor, $Re = 4845$.

The three models are now compared by extracting the axial velocity profiles from the two red lines placed in the middle of the reactive chamber, Figure 3.13, where line l crosses the reactor longitudinally, and line h horizontally. Figure 3.14 presents the averaged axial velocity along the two lines. In Figure 3.14a, results are plotted versus the normalized y coordinate. The two high velocity lateral zones identify in Figure 3.10 are caught by the three models with some differences. SST-k-ω does not make use of wall functions, and integrates the turbulent variables up to the wall.

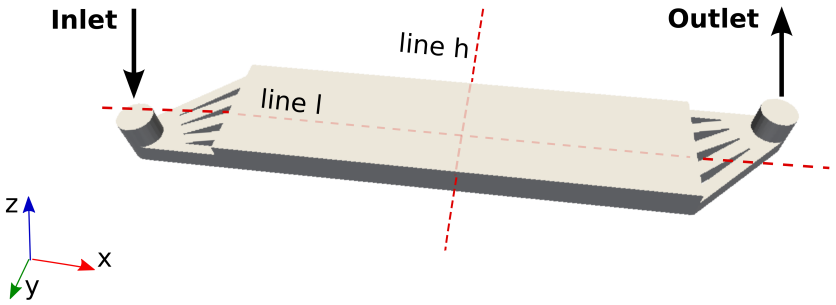

Figure 3.13 Longitudinal line l, and horizontal line h at $z = H/2$.

For values of y/W lower than 0.5, the agreement of SSt-k-ω with LES is good; but in the second half of the cell, the gap between the two increases. An opposite behavior is noticed for k-ε which has a better agreement with LES for values $0.5 \leq y/W \leq 1$, and over-predicts the axial velocity elsewhere. Figure 3.14b shows the averaged axial velocity along the longitudinal profile versus the normalized x coordinate. The figure compares the two models discussed in the turbulent section with respect to the target LES-velocity. Both SST-k-ω and k-ε well predicts the behavior of U_x for high values of x/L. Despite the computational time saving of k-ε using wall functions for wall treatments, the solution in magenta does not reproduce properly the target velocity for values $0.1 \leq x/L \leq 0.5$.

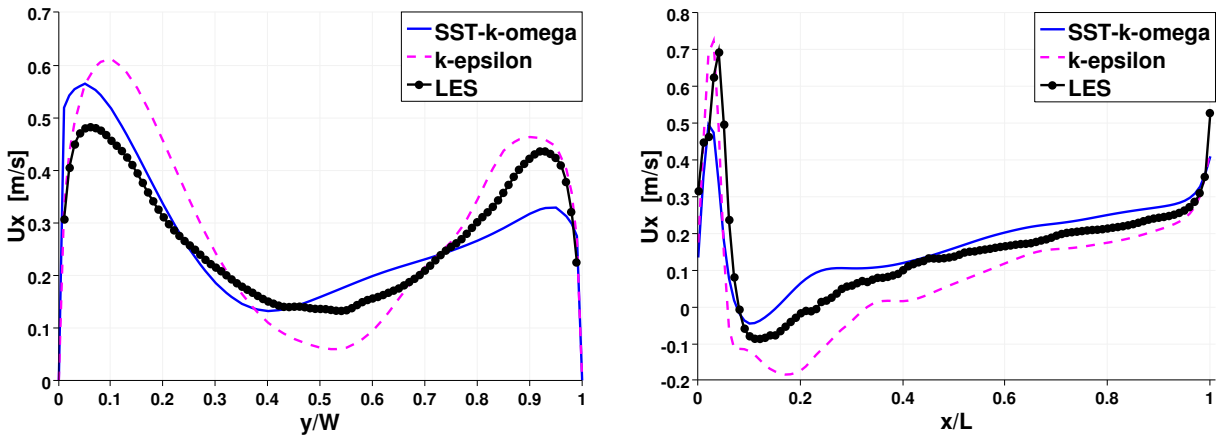

(a) Averaged U_x along line h.

(b) Averaged U_x along line l.

Figure 3.14 Averaged axial velocity profiles obtained with SST-k-ω (blue), k-ε (magenta), and LES (black) along lines h (3.14a), and l (3.14b), for $Re = 4845$.

Another interesting comparison is obtained in Figure 3.15 where the turbulence intensity (Ti) is plotted on a slice cut. The turbulence intensity is generally known to be the ratio between the fluctuating velocity u' and the the averaged magnitude velocity [47], and it can be expressed as in Eq. 3.26. [4]

$$Ti = \frac{\sqrt{\frac{2}{3}k}}{mag|\boldsymbol{U}|} \tag{3.26}$$

Figure 3.15 shows its trend on a slice cut at $z = H/2$ for the three turbulent models. The color maps are uniformed so that the reader is at ease with the comparison. In figure 3.15a k-ε predicts a turbulence intensity zone of elliptical shape, where $Ti \approx 3\%$. This zone is close to the entrance manifold and follows the diagonal path of the second and third jet. Inside this zone highlighted in green, three other areas with higher Ti are identified. The turbulence is then dumped, and propagates to the end of the reactive chamber with a small deviation to the right of the reactor due to the first straight jet at the entrance. The relatively high level of turbulence intensity in the first half of the reactor produces a desirable high level of mixing in the electrolytic solution. If on one hand this can be translated with a more productive cell, on the other hand it also means more anodic corrosion. This scenario will lead to an uneven and unwanted consumption of the electrode, and an under-prediction of the cell life-time. In Figure 3.15b the same slice is reproduced. The effect of the entrance manifold appears to be less concentrated. The green elliptical zone identified in the previous picture, is spread longitudinally but remains confined in the first part of the reactor. At its inside there are still few concentrated zones of higher turbulence intensity. This second scenario presents a less critic solution where Ti is less concentrated and more distributed in the first half of the chamber; but the non uniformity with the rest of the chamber will lead to the same conclusion. The elliptical shape of the first two pictures can be identified also in Figure 3.15c. This time the zones with higher Ti are concentrated at the edge of the ellipse and not inside it. The rest of the reactor looks to have a null turbulence intensity, but this is only due to the uniformed color maps, as the contours lines demonstrate. The use of LES produces a more even turbulence intensity distribution, with a smoothed gradient between the entrance and the exit of the reactor. The local mass transfer rate is probably less enhanced than in the case of k-ε, but the global mass transfer rate of the reactor modeled with LES is for sure higher, since the well mixing of the solution is guaranteed along the whole chamber. A more realistic prediction of the cell life-time is then achievable.

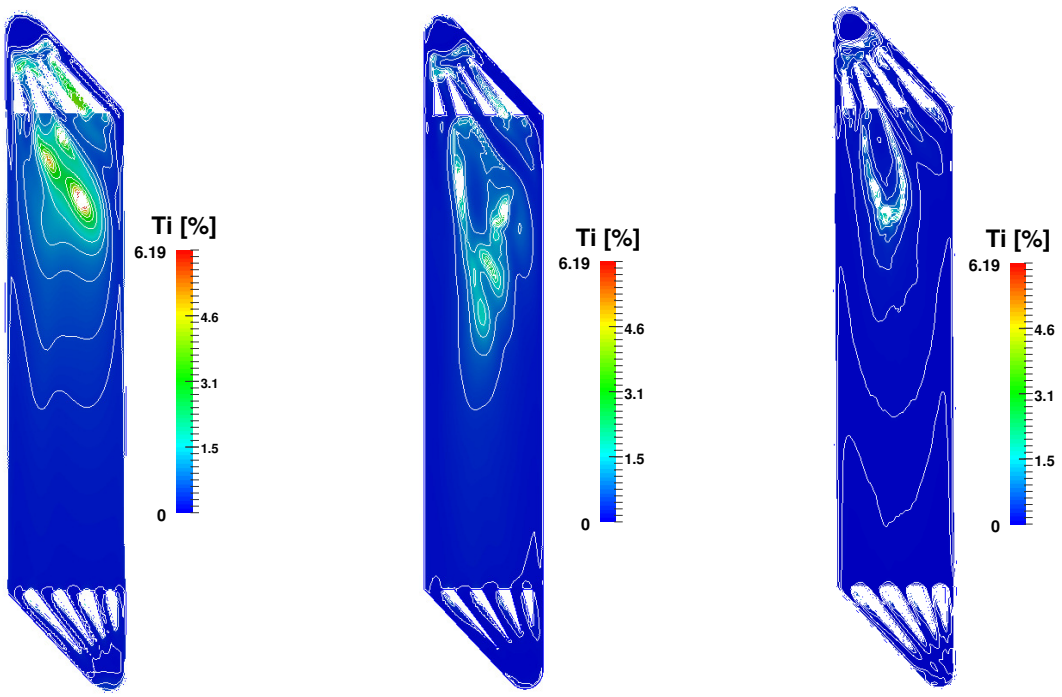

(a) k-ε. (b) SSt-k-ω. (c) LES.

Figure 3.15 Averaged turbulence intensity contours obtained on a slice at $z = H/2$ with k-ε (3.15a), SST-k-ω (3.15b), and LES (3.15c); $Re = 4845$.

As explained before, the three models make use of different meshes, and different wall treatments. For a reactor like the *FM01-LC* this work points at SST-k-ω as the most appropriate choice. It produces results close to LES simulation with a reasonable computational effort. Table 3.4 summarizes the resources used by each model, to give an idea of the various computational costs.

	k-ε	SST-k-ω	LES
wall time	01 : 01 : 08	03 : 11 : 57	119 : 56 : 04
cpu time	24 : 06 : 55	76 : 16 : 29	2871 : 42 : 09
memory [kb]	1,975,712	2,647,616	7,332,016
virtual memory [kb]	11,605,988	12,273,624	17,216,792

Table 3.4 Resources used: k-ε, SST-k-ω, and LES.

Section 3.2.4 lists all the discretization schemes used in this work. Particular attention is reserved to the divergence term, since its non linearity deeply affects the convergence of this strongly coupled problem. The sensitivity of the model to this discretization scheme is plotted in Figure 3.16. It presents the axial velocity profiles obtained by SST-k-ω model

using two different divergence schemes, and compares them to the LES result here used as target.

- Gauss limited linear.

  It has an accuracy of the second order, and it is characterized by a limiting function to avoid non physical values of the solution [64].

- Gauss upwind.

  It does not need any limiting functions, because it is able to remain confined to physical results on its own [64]. On the contrary it is a first order scheme, and it may incur in diffusive solutions specially when the flow it is not completely aligned with the mesh.

The blue solid line identifies the Gauss limited linear scheme. It follows the same trend as the LES dotted line, but it under-predicts the first peak, and over predicts the values around 0.25 x/L. From 0.3 x/L on, the two lines overlap. The dashed line in magenta makes use of the Gauss upwind scheme. The scheme is really sensitive to the artificial diffusivity caused by a non alignment between the flow and the mesh. This is indeed the case in the first half of the reactor, where the longest entrance channel produces a slow jet that hits the lateral edge of the reactor, flips its direction, and crosses diagonally the rectangular chamber. The bump already identified with the Gauss limited linear scheme is here emphasized. Nevertheless a good matching is noted in the second half of the reactor, where the flow swirl is attenuated.

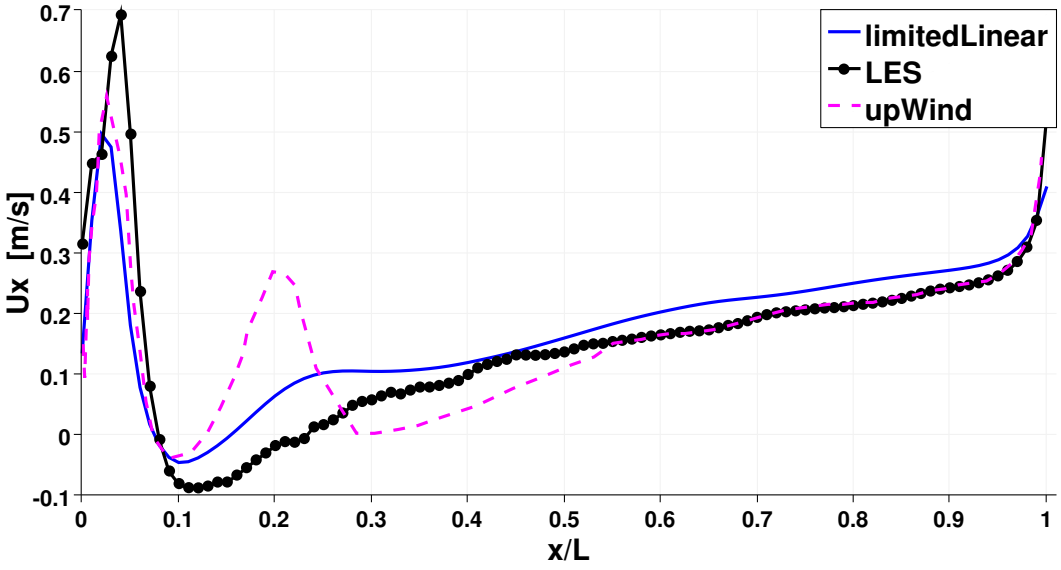

Figure 3.16 Averaged U_x profiles obtained with the discretization of the divergence term through Gauss limited linear (blue) and Gauss upwind schemes (magenta), along the longitudinal line l. Results use SST-k-ε model, and they are compared with the target LES, for $Re = 4845$.

Electrochemistry

The POTiso-loop already validated in a 2D rectangular geometry [29], is now exploited to investigate the effects of various Reynolds numbers and several cell potentials on the mole fraction of copper. The following three cases in Figure 3.17 present a parametric study on different Reynolds numbers. The reactors are fed with 18 mM of copper, and their cell potential ΔE_{cell} is fixed to $-0.03\ V$. The electrolyte flows along the x-direction, each slice is extracted at $z = 1.5\ mm$, close to the cathodic interface electrode/electrolyte, and the results are expressed in terms of mole fractions normalized by the $Y_{Cu^{2+}}$ inlet value. In Figure 3.17a Re 1384 produces a consumption of the mole fraction of copper close to the exit which tends to have a more uniform distribution. Despite it, a flow pattern with a visible tendency towards the bottom left part of the reactor can be noticed. This stream is pushed at the entrance of the reactor channel from the straight jet at the right, and it is sunk at the exit by the other straight jet placed at the left of the exit manifold. By increasing the Reynolds number to 2769 as in Figure 3.17b, the stream enhances its strength. The electrolyte becomes faster, and the higher mass flow rate keeps bringing in the reactive cell fresh solution. Last scenario in Figure 3.17c, has a doubled Reynolds number. The most reactive part appears to be even more confined in the diagonal stream where the ratio $Y_{Cu^{2+}}/Y_{Cu^{2+},inlet}$ reaches zero, while the rest of the solution is almost uniform in the surrounding areas. It can be summed up that high Reynolds number eventually facilitate the removal of the depleted solid copper pushing away the deposits on the cathode surface. On the other side a system with a lower Reynolds number can be desired to have a more even consumption of the electrodes, and a longer life time of the plates.

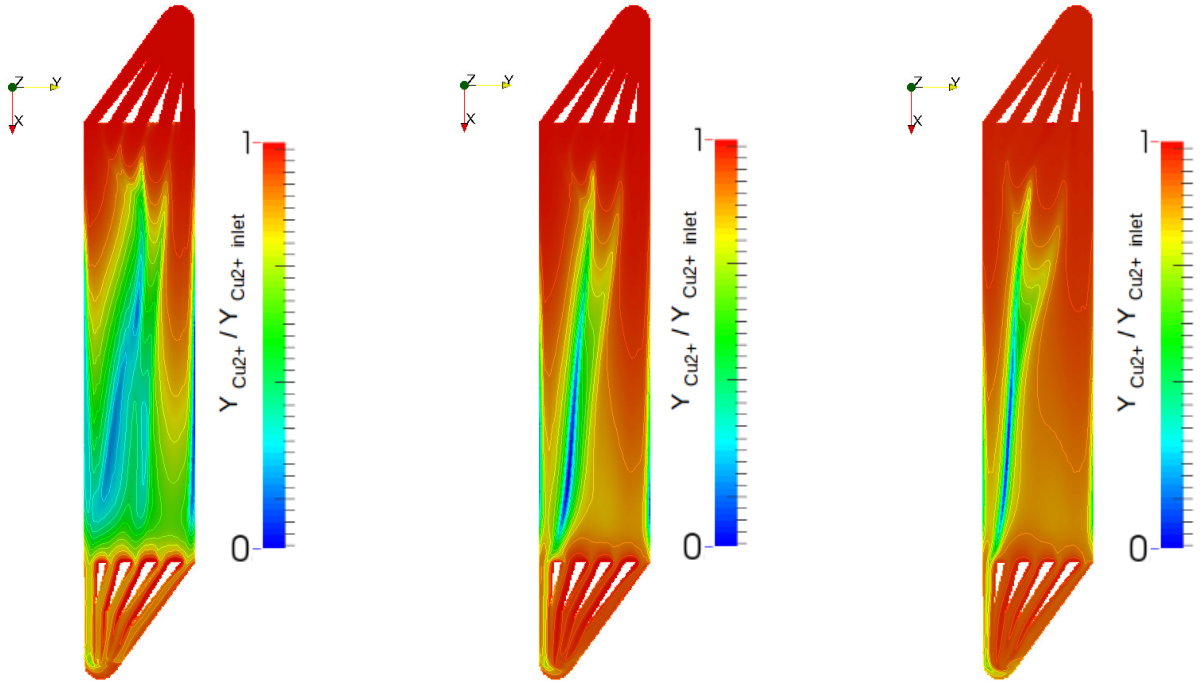

(a) Re 1384. (b) Re 2769. (c) Re 4845.

Figure 3.17 Parametric analysis on different Reynolds using SST-k-ε model: normalized mole fraction distribution of copper at $z = 1.5\ mm$, inlet copper concentration 18 mM, and $\Delta E_{cell} = -0.03\ V$.

After working on the effects of the Fluid-dynamics, it is important to study the role of the cell potential in this intricate scenario. The effects on the $FM01$-LC are investigated once more in terms of mole fraction distribution of copper along the reactor in Figure 3.18. The slices are extracted at the same height as before $z = 1.5\ mm$, the inlet copper concentration is still 18 mM, and the Reynolds number is now fixed to 4845. In Figure 3.18a, the cell potential is set to $0.06V$. The convection mechanism covers completely the effect of the migration, and the scenario presents again a strong non symmetry, depicted by the path crossing diagonally the whole electrode. Increasing the value of the cell potential up to $-0.13\ V$ as in Figure 3.18b, the migration term gets bigger and becomes comparable to the convection term whose effect is drastically reduced. The sinking effect of the diagonal stream is soften but remains still visible in the central green patch. Figure 3.18c follows the same trend and the augmentation of ΔE_{cell} produces a potential field strong enough to allow the migration term to become predominant over the convection. The FM01-LC reactor works under mass transfer limited conditions in the lower half of the reactor, where the concentration of copper is null. It can be said then that higher cell potentials are desired to push the reactor system up to its productive-limits. At the same time higher Reynolds numbers facilitate the removal of the depleted solid copper.

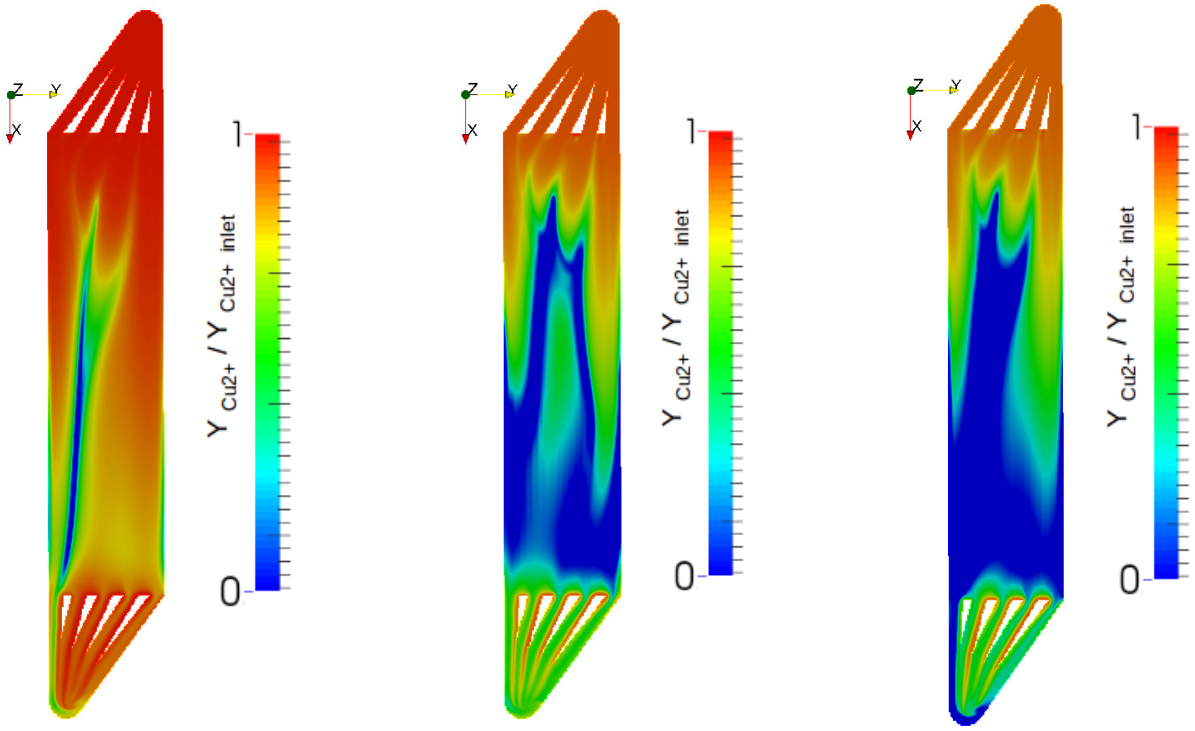

(a) ΔE_{cell} -0.06 V. (b) ΔE_{cell} -0.13 V. (c) ΔE_{cell} -0.21 V.

Figure 3.18 Parametric analysis on different ΔE_{cell} SST-k-ε model: normalized mole fraction distribution of copper at $z = 1.5$ mm, inlet copper concentration 18 mM, for $Re = 4845$.

3.2.6 Conclusions

The numerical model implemented in this study by means of OpenFoam-2.3.1, can be used to optimize the performance of a parallel plate electrochemical reactor. The new solver *POtisoFOAM* consists of two predictor-corrector loops. The first solves the fluid-dynamics here complicated by the geometry of the reactor. The $FM01$-LC presents an entrance and an exit manifold designed to increase the mixing of the electrolytic solution. A turbulence model is then required to allow a proper reproduction of the flow. Results prove that the SST-k-ω model without wall functions achieves this goal, by making use of the Gauss limited linear scheme to discretize the divergence terms. The second loop solves the electrochemistry by coupling the mole transport of ions with the charge conservation. The convection, migration, and diffusion phenomena are satisfactory implemented, alongside the ohmic drop and feeble concentration polarizations. The boundaries treatment at the active plates successfully implements the non linear Butler-Volmer equation. Results show that the geometry of the manifold at the entrance and at the exit of the reactor strongly impacts the cell's behavior. The electrolytic flow presents a favorite path crossing

diagonally the reactive channel. Fluid-dynamics results indicate that at low Reynolds numbers these effects are attenuated at the expenses of a lower production rate. A more uniform mole fraction of copper is achieved by using a high ΔE_{cell}, letting the migration mechanism dominating the convection phenomena. The drawback of such solution comes from the operative costs that may be involved to provide a higher current to the reactor, specially on industrial scales with multiple reactors in series. Finally *POTisoFOAM* can be used to reshape the manifold design and optimize the reactor's performance.

3.2.7 Acknowledgments

The authors are very grateful to the Canadian company *Hydro-Québec*, and to the *NSERC* which financially supported this study. The authors thank also the *Université de Sherbrooke* for its fellowship.

3.2.8 Nomenclature

Symbol	Units	Description
a_1	$m^2/(V\,s)$	model constant $=Fz_jD_j/RT$
a_2	$A\,m^2/(V\,kg\text{-}mol)$	model constant $=F^2/RT\sum_j z_j^2 D_j$
a_3	$A\,m^2/kg\text{-}mol$	model constant $=F\sum_j z_j D_j$
a_ω	$-$	SST-k-ω turbulent constant
B	$-$	k-ε turbulent constant
B_{LES}	m^2/s^2	$2/3\;kI - 2\nu_{sgs}dev(D)$
C_k	$-$	LES turbulent constant
C_e	$-$	LES turbulent constant
$C_{\varepsilon,1}$	$-$	k-ε turbulent constant
$C_{\varepsilon,2}$	$-$	k-ε turbulent constant
C_μ	$-$	k-ε turbulent constant
CFD	$-$	Computational Fluid-Dynamics
D_{eff}	m^2/s	effective diffusivity
D_s	m^2/s	molecular diffusivity of the s-th species
D_{LES}	$1/s$	$symm(\nabla \boldsymbol{U})$
DNS	$-$	Direct Numerical Simulation
E	V	electric potential
E^{surf}	V	electric potential on active plate
E^∞	V	equilibrium potential
F	$A\,s/kg\text{-}mol$	Faraday's constant

Table 3.5

Symbol	Units	Description
F_1	$-$	SST-k-ω constants' blending function
F_2	$-$	SST-k-ω nu_T blending function
h	$-$	horizontal line
H	m	reactive chamber's height
H'	m	paws height
i_0	$A\,m/kg\text{-}mol$	exchange current density associated to null potential
$\boldsymbol{i}_q$	$A\,m/kg\text{-}mol$	current density of the q-th reaction per units of C_{TOT}
K	$-$	von Karman's constant
k	m^2/s^2	turbulent kinetic energy
L	m	reactive chamber's length
L_c	m	characteristic length
LES	$-$	Large Eddy Simulation
l	$-$	longitudinal line
N	$-$	total number of species
$\boldsymbol{N}_s$	m/s	flux of the s-th species
n_q	$-$	number of electrons exchanged in the q-th reaction
$\boldsymbol{n}$	$-$	vector normal to the electrode' surface
P	Pa	pressure
$PPER$	$-$	Parallel Plate Electrochemical Reactor
P_{prod}	m^2/s^3	k-ε turbulent production
P'_{prod}	m^2/s^3	SST-k-ω turbulent production
$\boldsymbol{R}$	m^2/s^2	averaged Reynolds stresses
R	$J/(kg\text{-}mol\,K)$	universal gas constant
$RANS$	$-$	Reynolds Averaged Navier & Stokes
Re	$-$	Reynolds number
S	$1/s$	strain rate tensor
SGS	$-$	Sub-Grid Scales
SST	$-$	Shear Stress Transport

Table 3.6

Symbol	Units	Description
st_{sq}	$-$	stoichiometric coefficient of the s-th species in the q-th reaction
T	K	bulk temperature
Ti	$-$	turbulent intensity
t	s	time
ts	$-$	time step
$\boldsymbol{U}$	m/s	velocity
U_i	m/s	i-velocity component
U_j	m/s	j-velocity component
U_n^+	$-$	non dimensional normal velocity
U_x	m/s	axial velocity
u_τ	m/s	friction velocity = $\sqrt{\tau_w/\rho}$
u'	m/s	fluctuating velocity
V_c	m	cell volume
V_{el}	V	measured electrode potential
W	m	reactive chamber's width
WF	$-$	wall function
x_i	m	i-coordinate
x_j	m	j-coordinate
Y_s	$-$	mole fraction of the s-th species
z_s	$-$	charge number of the s-th species

Table 3.7

Greek Symbol	**Units**	**Description**
α	$-$	symmetry factor
α_ω	$-$	SST-k-ω turbulent constant
β^*	$-$	SST-k-ω turbulent constant
β	$-$	SST-k-ω turbulent constant
ε	m^2/s^3	turbulent dissipation
ΔE_{cell}	V	imposed cell voltage
Δ	m	LES cut-out filter
δ	m	distance from the wall
δ^+	$-$	non dimensional distance from the wall $= \delta u_\tau/\nu$
δ_{ij}	$-$	Kronecker delta
η	V	electrode overpotential
ν	m^2/s	solvent kinematic viscosity
ν_{eff}	m^2/s	effective kinematic viscosity
ν_{sgs}	m^2/s	sub-grid scale kinematic viscosity
ν_T	m^2/s	turbulent kinematic viscosity
ρ	kg/m^3	solvent density
σ_ε	$-$	k-ε turbulent constant
σ_k	$-$	turbulent constant
σ'_k	$-$	SST-k-ω turbulent constant
σ_ω	$-$	SST-k-ω turbulent constant
τ_w	N/m^2	wall shear stress $= \mu(\partial_y U)\|_w$
ω	$1/s$	specific rate of turbulent dissipation

Table 3.8

CHAPTER 4

Two-phase flow investigation in a lithium production cell

4.1 Avant-propos

Auteurs et affiliation:

- Giuliana Litrico: étudiante au doctorat*
- Elaheh Oliaii: étudiante au doctorat*
- Camila B. Vieira: étudiante au post-doctorat*
- Martin Désilets: professeur*
- Pierre Proulx: professeur*

* Université de Sherbrooke, Faculté de génie, Département de génie chimique et de génie biotechnologique

Date de soumission: January 2018

Revue: Journal of Fluid Flow, Heat and Mass Transfer

Titre français:
Étude du transfert de masse dans une cellule électrolytique pour la production de lithium utilisant un code CFD sur plate-forme ouverte

Contribution au document:
Cet article contribue à la thèse en étudiant la dynamique d'un réacteur électrochimique où la présence d'une phase gazeuse dans le liquide électrolyte affecte grandement le champ d'écoulement

Résumé français:
Une étude du transport des espèces chimiques dans une cellule de production électrolytique de lithium est effectuée en utilisant la librairie ouverte de calcul de mécanique des fluides numérique OpenFOAM. Le domaine numérique est discrétisé en utilisant l'hypothèse de symétrie axiale. Le coeur de la cellule modélisée est constitué d'une solution électrolytique eutectique de chlorure de potassium et de chlorure de lithium. Les ions Li^+ sont réduits

à la cathode alors que les ions Cl^- sont oxydés à l'anode en produisant du chlore gazeux. Les bulles de chlore produites sont entraînée par la force d'Archimède vers la surface de l'électrolyte, créant un mouvement de liquide par leur traînée. La convection naturelle ainsi induite contribue au transport des ions en plus des mouvements déjà associés à la migration et à la diffusion. Il en résulte un écoulement 2-phases turbulent augmentant le transport des ions, changeant la chute de potentiel aux électrodes et causant une polarisation de concentration. Le modèle mathématique développé traite le couplage prononcé entre les champs en utilisant une première étape de prédiction-correction qui résoud la mécanique des fluides, et d'une deuxième traitant du couplage électrochimique. Les conditions aux limites mixtes et fortement non-linéaires complètent la pose du problème. Une validation du modèle est présentée et les résultats des prédictions sont discutés.

4.2 Mass transfer study inside a Li production electrolysis cell using an open source CFD code

A mass transfer study in a lithium production electrolysis cell is carried out. The numerical domain is a 2D axis-symmetric wedge of 5^o. The bulk of the cell is filled with an electrolytic solution consisting of an eutectic mixture of $LiCl - KCl$. Lithium ions reduce at the cathode while Cl^- oxidize at the anode releasing bubbles of chlorine gas, which are moving upward due to their light density, thus dragging the nearby electrolyte. The induced convection is responsible for the transport of ions, together with the migration and diffusion mechanisms. The result is a turbulent two-phase flow accounting for the transport of ions, potential drop and polarization concentration. The highly non-linear coupled mathematical model is solved using an OpenFOAM solver designed to use predictor-corrector loops for both the fluid dynamics and the electrochemistry coupling. Non-linear mixed boundary conditions complete the set of governing equations.

4.3 Introduction

The demand for lithium has grown considerably during the last decades. Its importance has become unquestionable for the production of electronic devices and electric vehicles industry, where its lightweight and strong reduction potential is exploited. Batteries have been produced with a much higher volumetric and gravimetric energy densities - typically of the order of $160\,Wh/kg$ and $400\,Wh/L$ [50] - meaning almost 50% over conventional batteries. On the other side, lithium's production presents some important technological difficulties, for instance the electrodes' corrosion, back reactions, high energy demand, or the formation of unwanted foam [33], [11], [24], [3]. Therefore, in order to optimize its production, modeling the behavior of a standard cell where lithium is produced by the electrolysis of $LiCl$, is an essential tool. Figure 4.1a shows a simplified schematic of a Li-production cell. In the present model, cylindrical symmetry is assumed and only the concentrated electrolytic solution domain is taken into account with some contribution from the gas bubbles released at the central electrode, see Figure 4.1b.

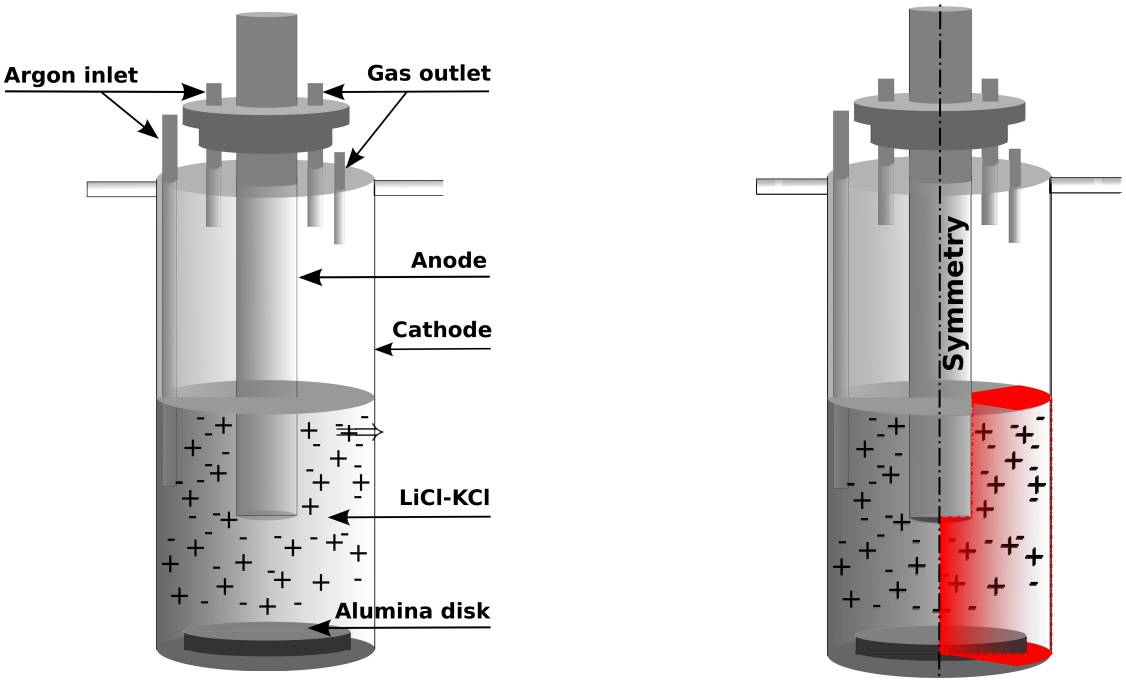

(a) Physical domain

(b) Numerical domain

Figure 4.1 Sketch of a standard cell (4.1a), and its numerical domain (4.1b) in red

At the cathode, Li^+ reduces to its metallic liquid phase (Eq.4.1) eventually extracted from the cell as it floats on the electrolyte.

$$Li^+ + e^- \rightleftharpoons Li_{liq} \tag{4.1}$$

The oxidation of chloride takes place at the anode where bubbles are released (Eq.4.2). Their upward movement causes natural convection circulation of the liquid in turn.

$$Cl^- \rightleftharpoons \frac{1}{2} Cl_{2,gas} + e^- \tag{4.2}$$

A mathematical model of this electrolytic cell results in a strongly coupled set of partial differential equations representing the complex interactions between these physical phenomena. In the following, it is presented a solution to this strongly coupled mathematical model using an open-source CFD tool (OpenFOAM) that enables to address some of the simplifications that have been used in earlier works [44, 52]. The presence of the secondary phase (chlorine bubbles) and its effect on the turbulence fields and the liquid electrolytic flow circulation is taken into account as well as the effect of the tertiary current distribution.

Therefore OpenFOAM is used here to accomplish the objective of this paper: showing for the first time the behavior of a Li electrolytic cell simulated with an OF model representing a two-phase turbulent flow, mass transfer in concentrated solutions (molten salt) and electrochemical surface reactions considering a tertiary current distribution.

4.4 Mathematical Modelling

The interaction among all phenomena just described is of utmost importance; however, for the sake of clarity, the governing equations below are split into three main areas of interest: fluid-dynamics, electrochemistry, and transport of ions.

4.4.1 Fluid-dynamics

The bulk solution mainly consists of a liquid $LiCl-KCl$ electrolyte, and a small amount of chlorine gas mostly located close to the anode. The cell dynamics obtained in a simulation without modeling the $Cl_{2,gas}$ upward motion would be completely different, close to a common batch reactor. Therefore, a two phase Euler-Euler model is employed under few assumptions:

1a. *No lift, and no virtual mass.* The drag force is the only one considered. Previous study demonstrated that the other interfacial forces are negligible [30].

1b. *Constant sized and spherical shaped bubbles.* The combination of the Reynolds, Eotvos, and Morton numbers helps to identify the bubbles shape as spherical through the graphical scheme regime for bubbles and drops [10].

1c. *Fixed turbulent Schmidt number* considered to be equal to 1 in this study.

The Euler-Euler model [58] treats the two phases as continua, with a unique common pressure p [17]. It consists of one continuity equation, Eq. 4.3, a constraint equation on the sum of the two volume phase fractions α_i, Eq. 4.4, and one momentum equation per phase, Eq. 4.5:

$$\frac{\partial \alpha_i}{\partial t} + \nabla.(\alpha_i \boldsymbol{U}_i) = 0 \tag{4.3}$$

$$\sum_i \alpha_i = 1 \tag{4.4}$$

$$\frac{\partial(\alpha_i \boldsymbol{U}_i)}{\partial t} + \nabla.(\alpha_i \boldsymbol{U}_i \boldsymbol{U}_i) = -\frac{\alpha_i}{\rho_i}\nabla p - \nabla.(\alpha_i \boldsymbol{R}_i) + \alpha_i \boldsymbol{g} + \frac{\boldsymbol{M}_i}{\rho_i} \tag{4.5}$$

where the subscript i identifies the i_{th} phase, $\boldsymbol{U}$ is the velocity, $\boldsymbol{R}$ the turbulent Reynolds stresses, and $\boldsymbol{M}$ the interfacial momentum transfer term, here consisting only of the drag force, Eq. 4.6. The latter accounts for the resistance felt by each gas-bubble moving inside the electrolyte, which affects the velocity of the gas phase, and its residence time in the cell.

$$\boldsymbol{F}_D = \frac{3}{4}\, C_D\, \alpha_{gas}\, \rho_{liq}\, \frac{1}{d_{gas}} |\boldsymbol{U}_{gas} - \boldsymbol{U}_{liq}|\, (\boldsymbol{U}_{gas} - \boldsymbol{U}_{liq}) \tag{4.6}$$

where d_{gas} is the fixed bubble's diameter, here set to 1.5 mm according to a similar experimental study [30], and C_D is the drag coefficient modeled as in Eq. 4.7 [59]:

$$C_D = \begin{cases} \frac{24\,(1+0.15\,Re_{rel}^{0.687})}{Re_{rel}} & Re_{rel} \leq 1e^3 \\ 0.44 & Re_{rel} > 1e^3 \end{cases} \quad , \quad Re_{rel} = \frac{|\boldsymbol{U}_{gas} - \boldsymbol{U}_{liq}|\, d_{gas}}{\nu_{liq}} \tag{4.7}$$

where ν_{liq} is the liquid kinematic viscosity. The presence of the bubbles and their movement through the reactor promotes turbulence in the liquid phase, however due to their low concentration, the gas turbulence as well as the bubble-bubble collisions can be neglected [4]. Therefore the standard $k-\varepsilon$ model is used only for the liquid phase. The balances of the turbulent kinetic energy (k), and the dissipation rate (ε) are expressed in Eq. 4.8 and Eq. 4.9:

$$\frac{\partial\,(\alpha k)}{\partial t} + \nabla \cdot (\alpha\, \boldsymbol{U}\, k) = \nabla \cdot \left[\alpha \left(\nu + \frac{\nu_T}{\sigma_k}\right) \nabla k\right] + \alpha\, P_k - \alpha\, \varepsilon \tag{4.8}$$

$$\frac{\partial\,(\alpha\varepsilon)}{\partial t} + \nabla \cdot (\alpha\, \boldsymbol{U}\, \varepsilon) = \nabla \cdot \left[\alpha \left(\nu + \frac{\nu_T}{\sigma_\varepsilon}\right) \nabla \varepsilon\right] + \alpha\, \frac{\varepsilon}{k}\, (C_{\varepsilon 1}\, P_k - C_{\varepsilon 2}\, \varepsilon) \tag{4.9}$$

$$with \quad P_k = 2\, \nu_{eff}\, \left[\nabla \boldsymbol{U}\, \cdot dev(\nabla \boldsymbol{U} + (\nabla \boldsymbol{U})^T)\right] \tag{4.10}$$

where the constants are $C_{\varepsilon 1} = 1.44$, $C_{\varepsilon 2} = 1.92$, $\sigma_k = 1.0$, $\sigma_\varepsilon = 1.3$, ν_{eff} is the sum of the laminar and turbulent viscosity, and P_k stands for the production of turbulent kinetic energy [32, 47, 58, 71]. The closure of this first set of equations comes with the appropriate boundary conditions shown in Table 4.1 and explained in the following bullet list:

- Anode:
  The volume fraction of the gas, α_{gas} depends on the distribution of the normal current density i_n as described in Eq. 4.11, [65].

$$\alpha_{gas} = 0.023\ i_n^{0.3} \tag{4.11}$$

  It is directly related to the mass flow rate j_n which induces $\boldsymbol{U}_{gas}$ at the anode, Eq. 4.12, [2].

$$j_n = \alpha_{gas}\ U_{n,gas} \quad , \quad j_n = \frac{i_n\ M_{gas}}{n\ F\ \rho_{gas}} \tag{4.12}$$

  The pressure gradient is tuned according to the velocity to maintain a constant flux. While the turbulent variables k, ε, and ν_T follow the well known algebraic relations from literature [27, 28, 62], re-grouped in Table 4.1 where Ti is the turbulence intensity, and l_{mix} the turbulent mixing length.
- Cathode & Walls:
  No-slip boundary conditions are imposed for the velocities, and the wall functions, wf, handle the turbulence variables [60].
- Outlet:
  Gas leaves the system at the outlet, no back-flow is allowed. Therefore a mixed boundary condition switching from a zero gradient to a zero value, depending on the direction of the flow (*inletOutlet*), is imposed for both α_{gas} and $\boldsymbol{U}_{gas}$. The liquid is confined inside the cell, it cannot leave but can glide along the outlet. A slip condition, meaning null normal component and null tangential derivative, is applied for $\boldsymbol{U}_{liq}$. By doing so, a degassing boundary condition is created, modeling the free surface condition between the top of liquid and the atmosphere [38].
- Front & Back:
  The standard cell is axis-symmetric, where the front and back do not represent physical faces but just the end of the numerical domain. A wedge condition containing this information is applied to all the variables for all sets of equation.

Variable	**Anode**	**Cathode & Walls**	**Outlet**	**Front & Back**
α_{gas}	$0.023\ i_n^{0.3}$	$\nabla\alpha_{gas} = 0$	$inletOutlet$	$wedge$
$U_{n,gas}$	j_n/α_{gas}	$no-slip$	$inletOutlet$	$wedge$
$\boldsymbol{U}_{liq}$	$no-slip$	$no-slip$	$slip$	$wedge$
p	$\nabla p = f_x(U)$	$\nabla p = f_x(U)$	$fixedValue$	$wedge$
k	$1.5(Ti\ U_{liq})^2$	wf	$\nabla k = 0$	$wedge$
ε	$C_\mu^{0.75}k^{1.5}/l_{mix}$	wf	$\nabla\varepsilon = 0$	$wedge$
ν_T	$C_\mu k^2/\varepsilon$	wf	$\nabla\nu_T = 0$	$wedge$

Table 4.1 Fluid-dynamics boundary conditions with the *OpenFOAM*-nomenclature

4.4.2 Electric field and current distribution

The charges distribution between the electrodes is the result of the current conservation law shown in Eq. 4.13. The first term represents the ohmic contribution, basically the potential gradient times the electrolyte's conductivity (later named K_e); while the second term is the polarization contribution.

$$\nabla\cdot\left[\nabla E\left(-\frac{F^2}{RT}\sum_s z_s^2 D_{s,mol}\,C_s\right) \quad -\nabla\left(F\sum_s z_s D_{s,eff}\,C_s\right)\right] = 0 \tag{4.13}$$

where T is the temperature of the ionic solution, z the charge number, C the ion's concentration, E the electrolytic potential, and the subscript s identifies the s_{th} species. Two additional variables appear in Eq. 4.13: the molecular diffusion coefficient ($D_{s,mol}$) of the s_{th} species with respect to the total mixture modeled through Wilke's correlation [72]; and the effective diffusivity ($D_{s,eff}$) arising from the turbulent and the molecular components (Eq. 4.14) :

$$D_{s,mol} = \frac{1-X_s}{\sum_{s\neq z}^{s=z}(X_z/D_{s,z,mol})} \qquad , \qquad D_{s,eff} = D_T + D_{s,mol} \tag{4.14}$$

where X is the molar fraction.

The following assumptions apply:

2a. *No adsorption.* Adsorption is neglected at the electrodes.

2b. *Equilibrium potential.* At both electrodes the equilibrium potential is assumed to be constant. No dependencies on ions' concentrations nor on their activities is accounted for.

2c. *Turbulent diffusivity.* Due to assumption *1c*, the turbulence diffusion coefficient is modeled as $D_T = \nu_T$.

Additionally, the set of equations obeys the following boundary conditions, which are summarized in Table 4.2.

- Anode:
  The current applied at the anode, faces a high overpotential (η) where the kinetic contribution of the heterogeneous reaction and the resistive layer of the freshly released bubbles are added. Therefore the slow oxidation of chlorine is modeled through Eq.4.15, where the Butler-Volmer equation in its Tafel form is presented (slow reaction → high overpotential → Tafel approximation, [42])

$$i_n = i_{0,a}\,(1-\alpha_{gas})\,exp\left(\frac{\eta F \alpha_{sym}}{RT}\right) \tag{4.15}$$

  where $i_{0,a} = 10\ A/m^2$ is the exchange current density, $\alpha_{sym} = 0.5$ the symmetric coefficient, while the term $(1-\alpha_{gas})$ stands for the portion of surface available for the electrochemical reaction due to the fact that the anode surface is partly blocked by the bubbles. The i_n just calculated is then divided by the electrolyte's conductivity (K_e) and imposed to be equal to the normal gradient potential. The electrolyte conductivity close to the anode is altered by the presence of bubbles [30], where the resistive layer formed has a conductivity that can be estimated as in Eq. 4.16, [1]:

$$K_{gas} = K_e\,(1-\alpha_{gas})^{1.5} \tag{4.16}$$

  Results prove that neglecting the concentration polarization at the anode is a correct assumption. See Section 4.5.3.

- Cathode:
  Contrary to the anodic reaction, the reduction of lithium is a fast reaction. The current density is linked to the kinetic overpotential through Eq. 4.17, where the Butler-Volmer equation is written in its linearized form (fast reaction → small overpotential → linear approximation [42]). The exchange current density is assumed to be high, for instance $i_{0,c} = 1000\ A/m^2$, while the surface potential E_{surf}, and

the equilibrium potential E_{eq}^{∞} are set to zero, so that the whole cell potential is imposed at the anode.

$$i_n = i_{0,c}\, F \frac{\eta}{RT} \tag{4.17}$$

- Outlet & Walls:
  A slip boundary condition on the current density is imposed, meaning null normal component and null tangential derivative. It blocks the charges from escaping the cell, but allows them to slide along the boundary, while the gradient of the electrolytic potential is set to zero.

Variable	**Anode**	**Cathode**	**Outlet & Walls**
i	$i_{0,a}\,(1-\alpha_{gas}) exp\left(\frac{\eta F \alpha_{sym}}{RT}\right)$	$i_{0,c}\, F \frac{\eta}{RT}$	$slip$
E	$\nabla E = i_n / K_e$	$E_{surf} - E_{eq}^{\infty} - \eta$	$\nabla E = 0$

Table 4.2 Electrochemical boundary conditions with the *OpenFOAM*-nomenclature

4.4.3 Transport of ions

Inside this electrolytic cell, the movement of ions is driven by the electrolyte's velocity (convection), the concentration's gradient (diffusion), and by the potential's gradient (migration). While the convection induces the same motion to all the species, the diffusive and the migrative mechanisms are dependent on the diffusion coefficients and the mobility of each species. The transport equation, Eq. 4.18, is solved for $N_{tot} - 1$ species, being Cl^-, Li^+, and K^+.

$$\frac{\partial C_s}{\partial t} + \boldsymbol{U}_{liq} \cdot \nabla C_s - D_{s,eff}\, \nabla^2 C_s = z_s \frac{F}{RT}\ \nabla \cdot (D_{s,mol} C_s\, \nabla E) \tag{4.18}$$

The extra equation needed to balance the number of unknowns is the electroneutrality of the solution, Eq. 4.19. It assures that there are no spurious charges floating around:

$$\sum_s z_s C_s = 0 \tag{4.19}$$

The already complex system of equations, and its strong full coupling suggest to include few additional assumptions without compromising the generality of the problem:

3a. *Nernst-Planck.* The Nernst-Planck conservation law is employed instead of the Maxwell-Stefan diffusion and convection equation.

3b. *No homogeneous reactions.* There are no reactions in the bulk of the reactor, only at the electrodes.

The boundary treatments is deployed below. In Table 4.3 the conditions are expressed in terms of the fluxes N_s. The convective term is included for clarity, but it is null since $\boldsymbol{U}_{liq} = 0$ at the wall. In the source code, Eq. 4.20 is manipulated, and a mixed boundary condition is written in terms of concentrations. The latter is implemented with a blending function weighting the Dirichlet condition (migration term) and the Neumann condition (diffusive term).

$$N_s = \boldsymbol{U}_{liq} C_s - D_{s,eff} \nabla C_s - z_s \frac{F}{RT} D_{s,mol} C_s \nabla E \tag{4.20}$$

- Anode:
  The only active species at the anode is the chloride. Its normal flux is regulated by Faraday's law, where the normal current density described in Section 4.4.2 is divided by the number of electrons involved in the reaction n_q times the Faraday's constant. Lithium and potassium ions do not react, and their flux is null.
- Cathode:
  A similar scenario occurs at the cathode, but chlorine and lithium ions switch their role. The latter becomes the active species following the Faraday's law, while chlorine do not react. The same condition as the anode holds for K^+.
- Outlet & Walls:
  A zero flux condition should be imposed for all species but the migration term is already set to zero thanks to the condition on the potential gradient in Table 4.2. Therefore it is sufficient to impose a zero concentration gradient for all species.

Variable	**Anode**	**Cathode**	**Outlet & Walls**
C_{Cl^-}	$N_{Cl^-} = i_n/(n_{ox,Cl}F)$	$N_{Cl^-} = 0$	$\nabla C_{Cl^-} = 0$
C_{Li^+}	$N_{Li^+} = 0$	$N_{Li^+} = i_n/(n_{red,Li}F)$	$\nabla C_{Li^+} = 0$
C_{K^+}	$N_{K^+} = 0$	$N_{K^+} = 0$	$\nabla C_{K^+} = 0$

Table 4.3 Concentration boundary conditions with the *OpenFOAM*-nomenclature

4.4.4 Simulation

Built using the framework of OpenFOAM, the numerical model developed uses an object-oriented approach, in which the classes' structures are confined in specific regions of the code where they are easier to manage. The main core of the solver is made of two predictor-corrector loops, namely *PIMPLE*, and *POTiso* [29]. The PIMPLE algorithm takes care of the fluid-dynamics of the problem [21], [22], [23], [45], [12], and its biggest advantage is the increase of the time step without any restriction on the Courant number. Basically an initial guessed pressure is employed to solve the momentum equation and to get an estimation of the velocity. The latter is then used to update the pressure at the present time step, which in turn corrects the velocity. The solver also uses a Multidimensional Universal Limiter for Explicit Solution (MULES) method [46], to maintain boundedness of the phase fractions. Similarly, the electrochemical solver uses a predictor-corrector loop (POTiso) which starts with an initial guess on the potential, solves $N-1$ transport equations. The predicted species' concentrations are then used to solve the charge continuity equation and get the updated value for the potential field. Finally the ions' transport equations are solved again to correct their previous appraisals. The two loops are sequential since it can be assumed that there is a one-way-coupling between the fluid mechanics (advection) and the electrochemical phenomena [57].

All partial differential equations are solved using the Finite Volume Method. The first derivatives in time are discretized with an *Euler* first order, bounded, implicit method. The gradients are all discretized by means of the second order *least squares* method. The divergence terms are treated with a Gaussian second order, but they are of different types: a *Gauss vanLeer* is used in Eq. 4.3; a *Gauss limitedLinearV 1* taking into account the

direction of the field is used in Eqs. 4.5, 4.8, and 4.9, and finally a *bounded upwind* applies in Eq. 4.18. The laplacian schemes are handled with a *Gauss linear corrected* method, acting as an unbounded, second order, conservative method; and at last the interpolation schemes are simply *linear*. Furthermore all the boundary conditions are implemented through the utility *groovyBC*. For further details the reader is referred to the OpenFOAM user guide.

Additional information include:

- the initial composition of the concentrated solution consists of 60% of $LiCl$ and 40% of KCl (molar basis),
- the bulk solution is in an isotherm equilibrium at 723 K,
- a constant current of 65 A is imposed at the anode.

The numerical domain illustrated in Figure 4.1b has the dimensions of 76 x 3.3 x 200 mm^3, and it is divided in 4575 hexahedra cells, and 50 prisms, with a maximum skewness of 1.06. The wedge has an angle of 5^o.

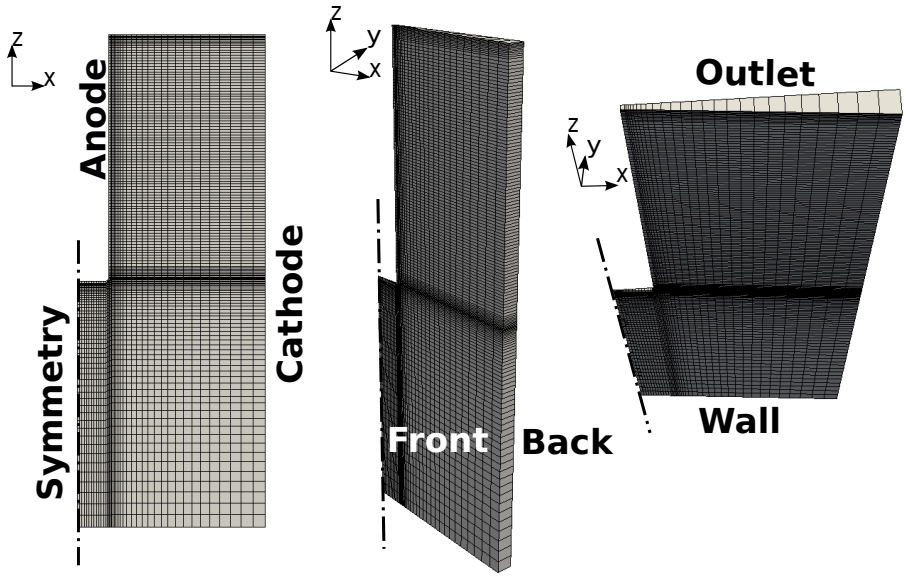

Figure 4.2 2D axi-symmetric mesh

The maximum aspect ratio is 15, and it is located close to the corner of the L-shaped anode, where 4 refinement layers are applied to catch the exact amount of gas entering the system. Eight extra refinements are also added close to the Outlet, to make sure that the free surface is adequately approximated. The Wall and the Cathode present a coarser mesh so that the $y^+ > 11$ criteria [60] is respected and wall functions can be applied for the turbulent flow. The maximum mesh non-orthogonality is way below the critical value

of 70, and its average is 6.9. The mesh just described is reported in Figure 4.2, and has positively passed the mesh dependency test, proving that the solution is not affected by the mesh chosen.

To solve the momentum equations for $\boldsymbol{U}$, k, and ε a smooth solver is used, while the p is evaluated with a generalized geometric-algebric multi grid solver. The conservation of charges makes use of a diagonal incomplete Cholesky preconditioned conjugate gradient solver. Finally the transport equations are solved through a diagonal incomplete LU preconditioned bi-conjugate gradient solver [46].

4.5 Results and Discussions

The following section presents the results of this work divided in three main groups earlier introduced in Section 4.4.

4.5.1 Fluid-dynamics

The first predictor corrector loop solves the fluid-dynamics of the problem and the associated turbulence. Figure 4.3a shows the magnitude of the electrolyte's velocity field after 3600 s. The peak of 0.291 m/s is found close to the anode where the gas, released by the oxidation of chloride, drags the electrolyte upward. Once the electrolyte reaches at the outlet, it can not escape (as imposed by its slip condition), and it is pushed rightward the cathode. Then it falls down and it is pulled back inside the bulk, where it splits in two parts: a faster clockwise re-circulation on the upper side of the cell, and a slower counterclockwise re-circulation at the bottom. On top of the colored magnitude velocity map, Figure 4.3a shows also the electrolyte's velocity vectors. The vectors are not scaled with the velocity magnitude direction; the intent here is only to identify the direction of the flow and the zones just described.

The same three zones can be identified in Figure 4.3b. The peak this time is located at the upper end of the anode, where the flow changes sharply. The nucleus of the clockwise circulation is shifted with respect to the center of the electrodes' gap, because a portion of the flow with lower kinetic energy is entrapped. Meanwhile the wall functions along the cathode and the bottom wall integrate appropriately the kinematic viscosity from the bulk through the viscous sub-layer.

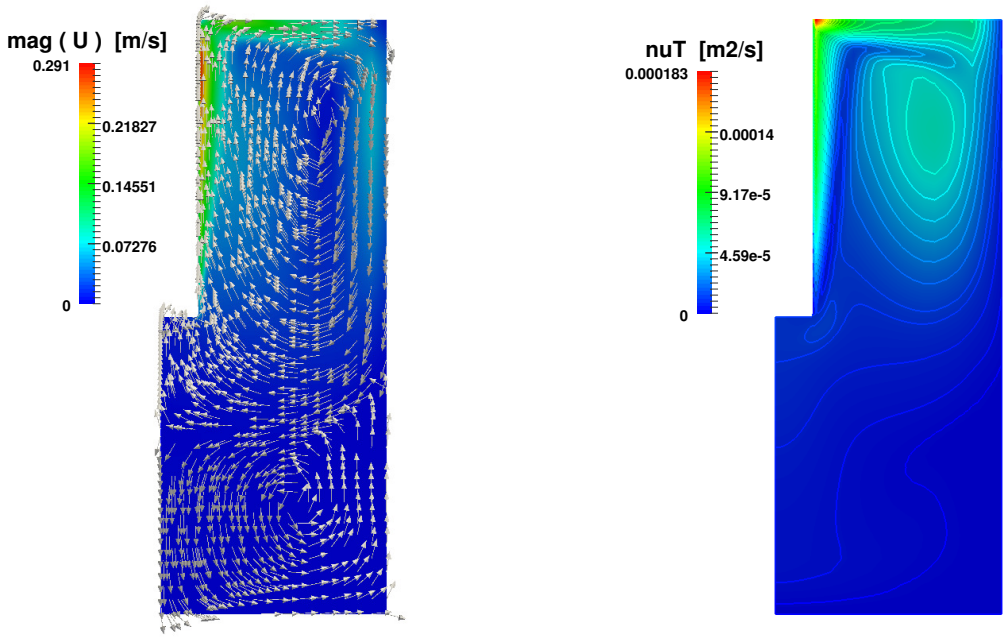

(a) Electrolyte velocity (b) Kinematic viscosity

Figure 4.3 Scaled off electrolyte's velocity vectors on top of the 2D slice of the electrolyte's magnitude velocity map (4.3a). Kinematic viscosity map and its contours (4.3b)

The induced gas velocity field map is not shown here since the $Cl_{2,gas}$ remains confined to a thin layer close to the anode and escapes once it reaches the top of the cell. Very little gas can be seen at the free surface interface, but it does not affect the flow afterwards. On the other hand, the bubble coverage along the anode is much more of interest. Since the authors are not aware of available experimental measurements published on this type of cell configuration for lithium production, a magnesium cell with a similar behavior is used for the validation of the model. This cell has a slightly different configuration with two vertical parallel anodes, a cathode placed in between and an electrolytic solution with a fixed flow rate injected from the bottom [30]. After matching the initial conditions of the experimental data [30], the calculated gas distribution is plotted on top of the PIV data image in Figure 4.4 with the permission of the *Canadian Journal of Chemical Engineering*. The blue line identifies the gas volume fraction (namely α_{gas}) obtained in this work. After the initial small oscillation at the bottom entrance of the left anode, the curve follows the same behavior of the bubbles in the background of the image, showing that the present model appears to reproduce adequately the bubble's movement. The red horizontal lines help to measure the growth of the bubble layer, being null at the entrance of the electrode, 10 mm in the middle, and increasing up to 20 mm close to the free surface.

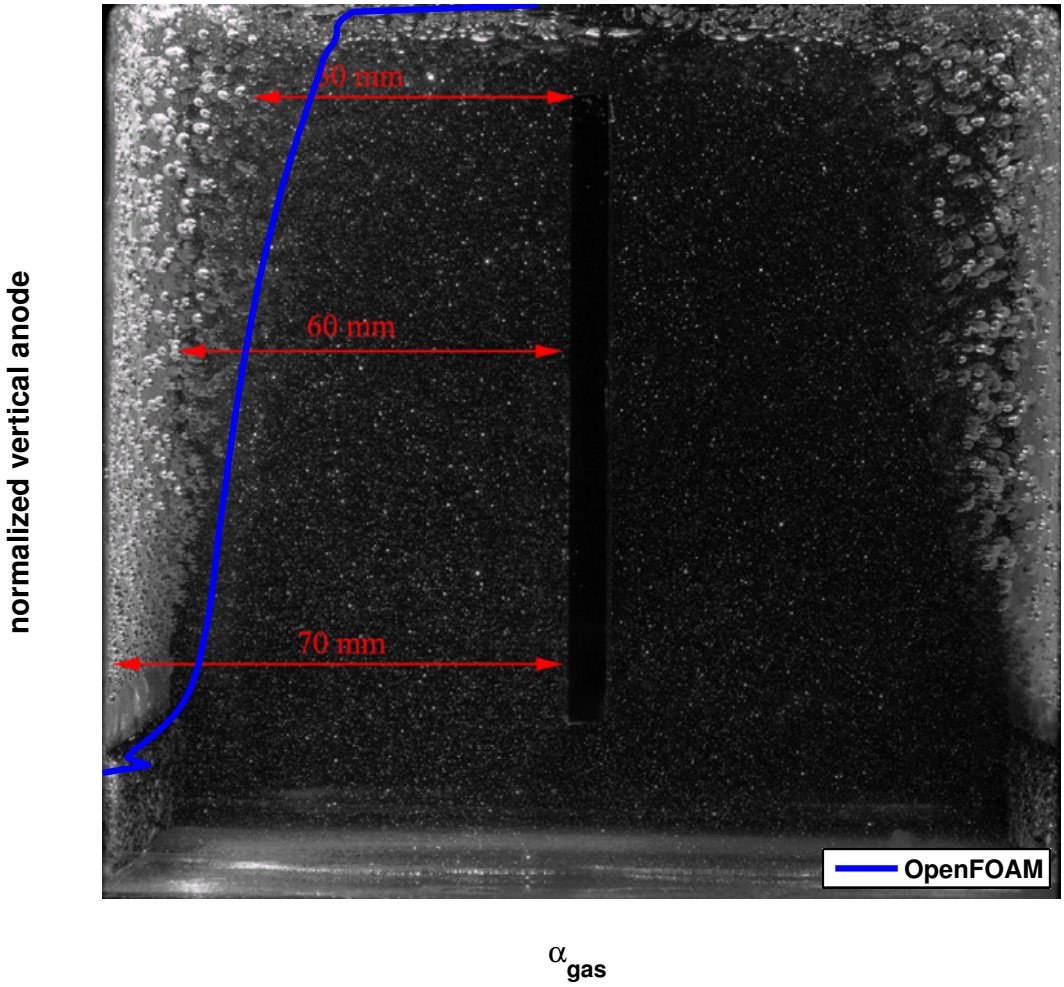

Figure 4.4 PIV data imaging of a magnesium cell [30] and α_{gas} evolution along the anode obtained in this work

4.5.2 Electrochemistry

The second calculation loop solves the electrochemical part, whose results are described below. Figure 4.5a shows the magnitude of the current density vectors along the anode. The peak of 1.5e4 A/m^2 at the lower anodic corner decreases gradually toward the two other extremities of the electrode. The importance of this result is crucial since it is responsible for the gas velocity distribution, which in turns induces the electrolyte motion, which in turns affects the convective mechanism of the transported ions, and as a con-

sequence the electric potential field. In Figure 4.5b the anodic current density resulting from this study is compared with the anodic current density of published work of Oliaii [44]. The ordinate measures the length of the whole anode, where the zero corresponds to the left extremity of the horizontal part and the value of 0.115 m to the last point at the top of the vertical anode. The peak is located at the corner between these two parts. The solid blue line is the result of this work, and the red dashed line is extracted from [44], where the horizontal contribution is not considered.

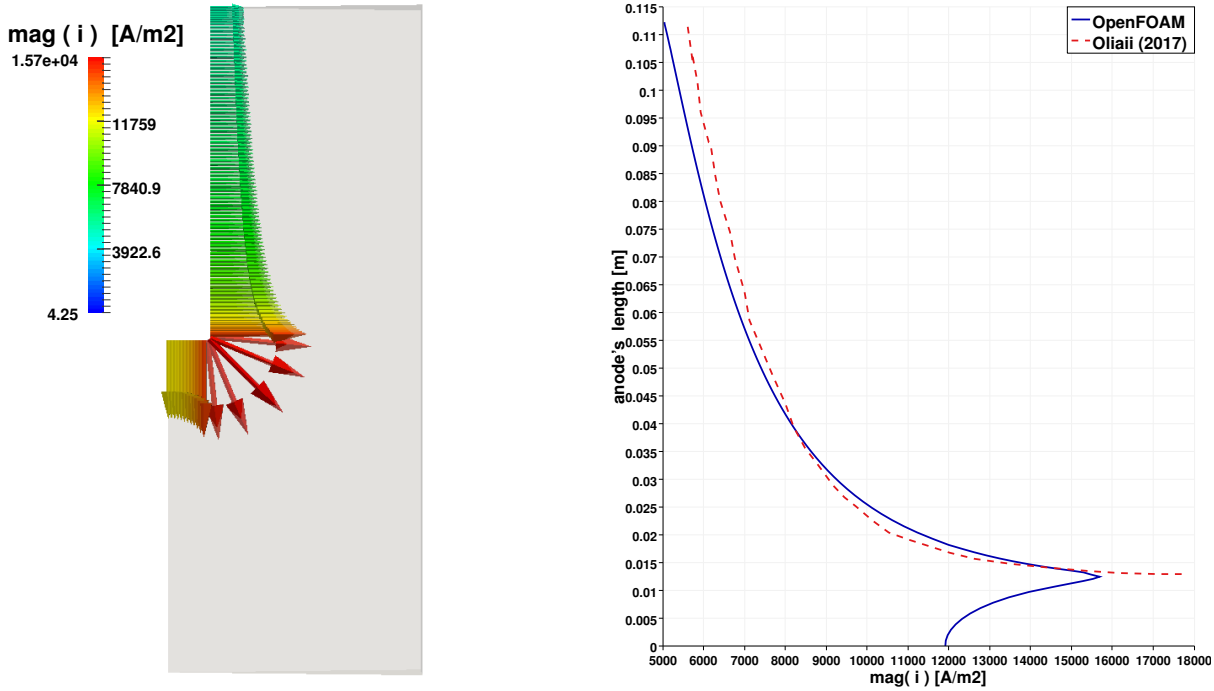

(a) Current density vectors

(b) Current density distribution

Figure 4.5 Magnitude of the current density's vectors (4.5a), and its distribution's profile along the anode (4.5b) compared with a previously validated model [44]

Analogously the electric potential field is reported in Figure 4.6a. The maximum values are found at the bottom of the anode, where the bubble coverage is less as shown in Figure 4.4. Away from the anode, the electric potential decreases all the way down to the cathode, where only the kinetic overpotential is present. A more detailed description of the anodic scenario is plotted in Figure 4.6b. The ordinates indicate the anodic length as explained for Figure 4.5b, and the abscissa the intensity of the potentials expressed in $[V]$. The solid lines are the results of this study, while the dashed lines reproduce the results of [44]. The black lines show the trend of the electrolytic potential. Apart from a small portion of the electrode, its value decreases from the bottom of the vertical anode up to the top. The same occurs to the kinetic overpotential with the only difference being the

concavity of the curve. An opposite behavior is noted on the distribution of the resistive overpotential induced by the gas film. Its lowest value is registered at the horizontal anode and it increases (almost linearly) all the way up to the outlet of the cell, where the resistive layer created by the bubble reduces the conductivity of the nearby electrolyte, as explained in Eq. 4.16. All the three potentials present a peak at around 0.012 m, which corresponds to the corner of the L-shaped anode as already mentioned for the current density distribution.

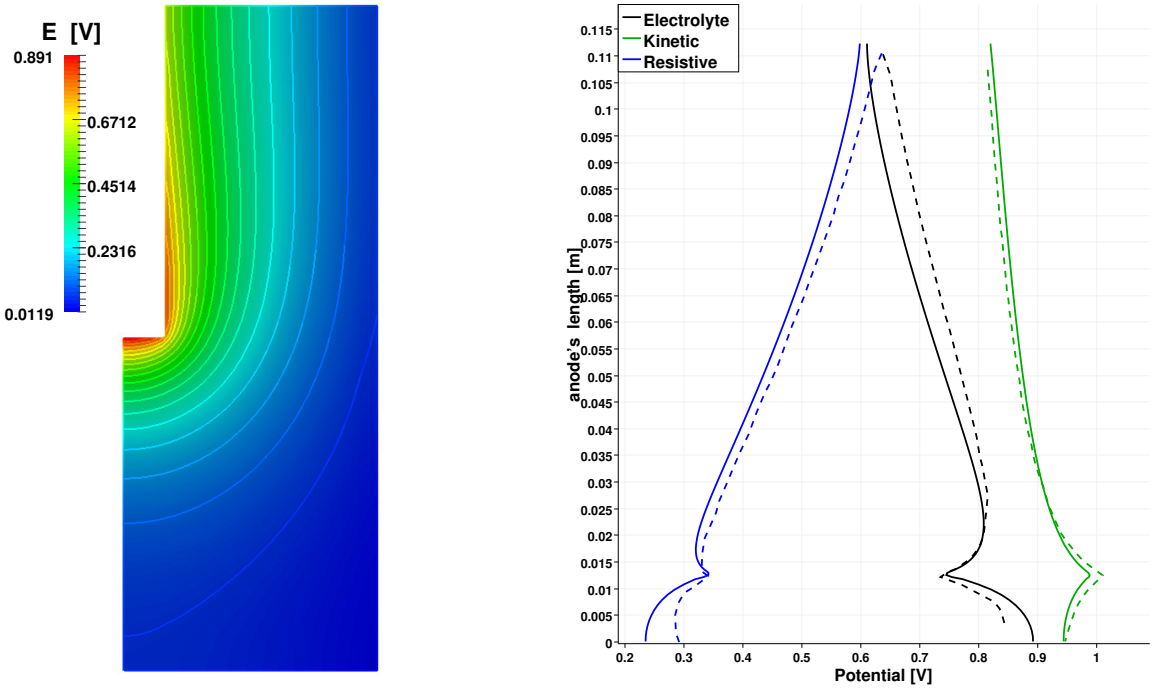

(a) Electric potential

(b) Anodic potential distributions

Figure 4.6 Electric potential field (4.6a), and anodic distributions of the electrolytic, kinetic, and resistive overpotential (4.6b) compared with previously validated work in dashed lines [44]

4.5.3 Transport of ions

The last part of this section presents the motion of ions across the cell. The three species Cl^-, Li^+, and K^+ are driven by convection, diffusion and migration. Figure 4.7, 4.8, and 4.9, show the electrodes' behavior of the migration (in blue) and the diffusion fluxes (in magenta) of chlorine, lithium, and potassium respectively. The contribution of the convection at the electrodes is zero since a non slip condition is imposed for the electrolyte's velocity.

Figure 4.7a plots the perpendicular components of both the migration and the diffusion fluxes of Cl^-. The horizontal part of the anode is not presented for the sake of clarity, but it follows the same trend as the vertical part.

The arrows at the left electrode are scaled with the magnitude intensity of the vectors themselves; but a magnifying factor is applied on vectors at the right electrode to better check the direction of the fluxes until the bottom of the cell where their intensity is smaller. At the positive electrode both fluxes are exiting the domain. Figure 4.7b shows the monotonic trends of the anodic fluxes decreasing in an absolute value from $8e^{-5}$ $kg\text{-}mol/(m^2 s)$ at the anode's corner, to approximately $3e^{-5}$ $kg\text{-}mol/(m^2 s)$ close to the outlet. It is important to point out that along the anode the two fluxes are not the same. Their sum is the result of the chloride's heterogeneous reaction and it is proportional to $\sim i_n/(n_{Cl^-}\ F)$ as described in Table 4.3. On the other hand at the cathode, chloride is a non-active species, and its total flux impacting the electrode has to be zero. Figure 4.7c proves that the contribution of the diffusion flux cancels out the migration component in each segment of the cathode. Additionally both cathodic curves change their curvature at approximately $0.08\ m$ from the bottom of the cell. This is the location where the electrolytic flow splits into two counter rotating zones, affecting the turbulent diffusion and the effective diffusivity through assumption *2c.*, and Eq. 4.14 respectively. It is also possible to notice that the fluxes on this side of the reactor present normal components one order of magnitude smaller than those at the anode as previously mentioned.

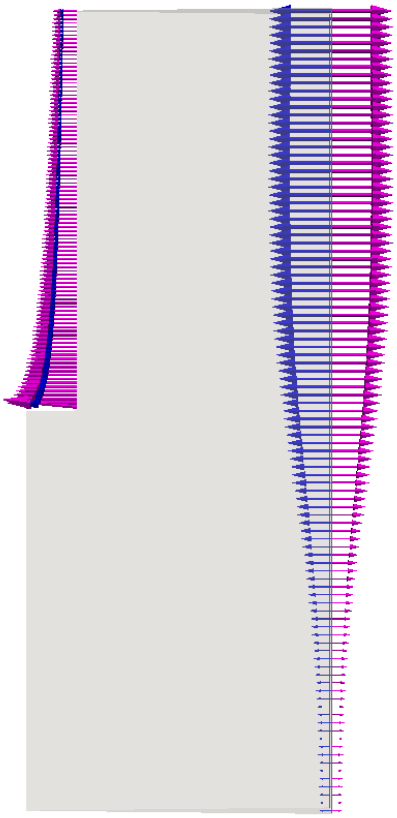

(a) Migration and diffusion fluxes

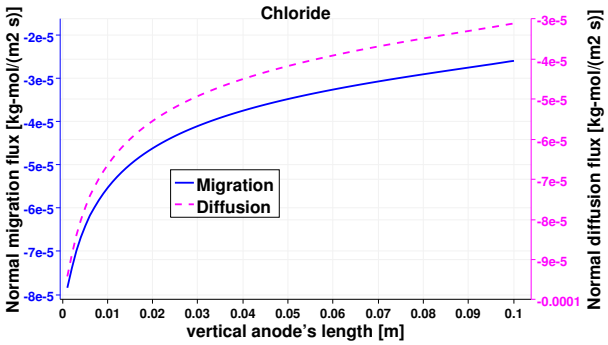

(b) Anodic fluxes distributions

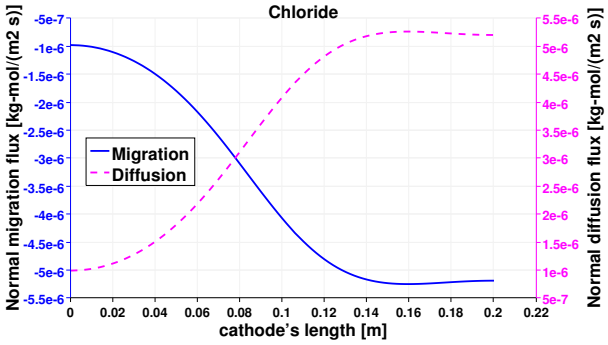

(c) Cathodic fluxes distributions

Figure 4.7 Normal components at the electrodes of the migration (blue) and diffusion fluxes (magenta) of Cl^- (4.7a). Distributions of the same fluxes along the vertical anode (4.7b), and cathode (4.7c)

The same analysis is performed on lithium, and Figure 4.8a presents the normal vector components of its diffusive and migrative fluxes at the electrodes. The first main difference with respect to Figure 4.7a, is the opposite direction of the migrative arrows, due to their charge number $z_{Li^+} = -z_{Cl^-}$. Lithium ions are attracted to the positive electrode, and tend to escape the negative cathode. Despite the magnifying factor used for vectors at the negative electrode, the migrative contribution is still weak, especially at the bottom of the reactor. The anode represents the non-active surface for lithium, in fact the two fluxes have opposite directions and cancel each other. Figure 4.8b plots the normal diffusion and migration fluxes along the vertical anode, with the diffusive mechanism being predominant as it can be noticed on the right scale of Figure 4.8c. The sum between the two fluxes is the results of the heterogeneous reaction occurring at the cathode (see Table 4.3). Nevertheless the shapes of the two curves are similar and their inflection point is again located around 0.8 m from the bottom of the cell.

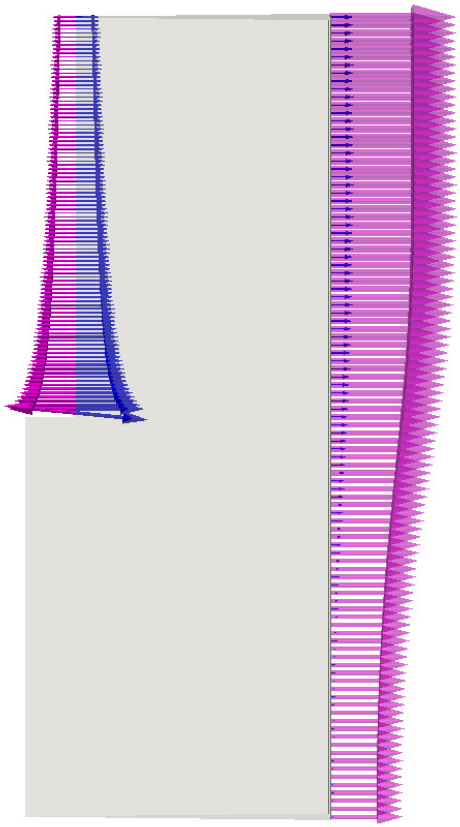

(a) Migration and diffusion fluxes

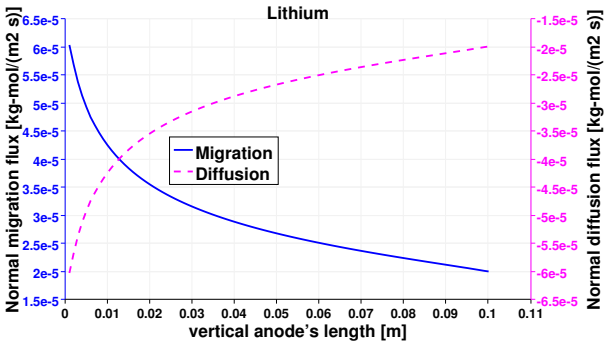

(b) Anodic fluxes distributions

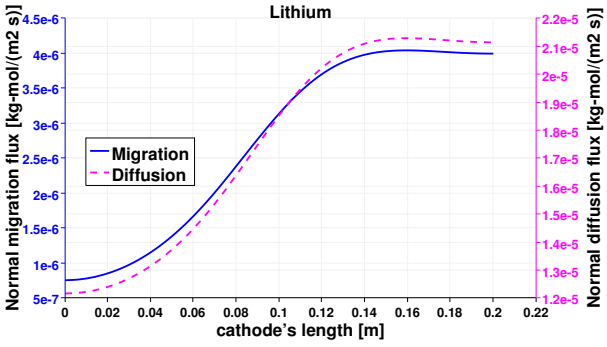

(c) Cathodic fluxes distributions

Figure 4.8 Normal components at the electrodes of the migration (blue) and diffusion fluxes (magenta) of Li^+ (4.8a). Distributions of the same fluxes along the vertical anode (4.8b), and cathode (4.8c)

The study is completed by presenting the results of the mass transport of the third species, K^+. Figure 4.9a reports that the migration fluxes of K^+ are aligned with those of Li^+ due to their equal charge numbers. Potassium is the only considered species which is non-active at both the electrodes. Indeed it presents the same fluxes' behavior of *Lithium* at the anode and of *Chloride* at the cathode. Nevertheless their scales are not the same due to the different diffusion coefficients and concentration's gradients of the species. Therefore, the same considerations elaborated before for Figures 4.7c and 4.8b are valid for Figures 4.9c and 4.9b.

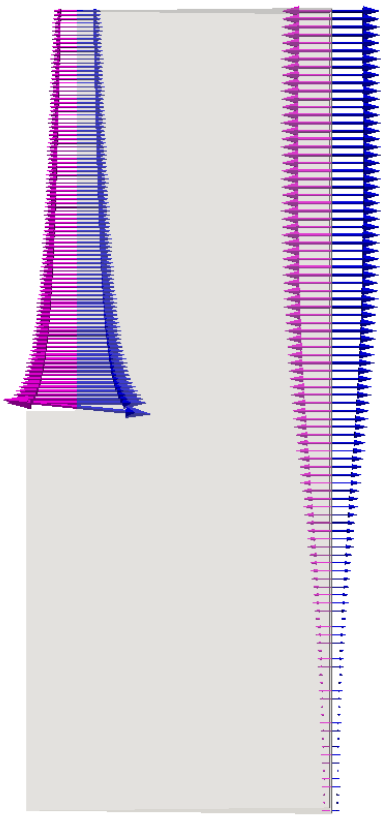

(a) Migration and diffusion fluxes

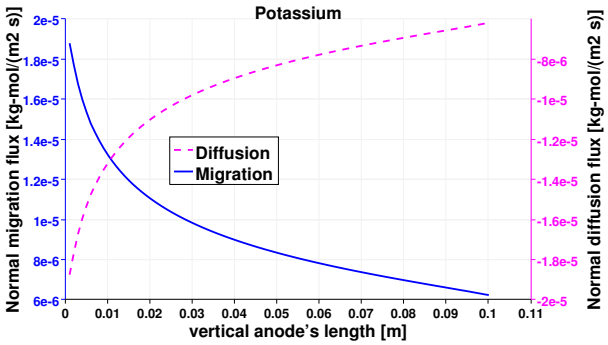

(b) Anodic fluxes distributions

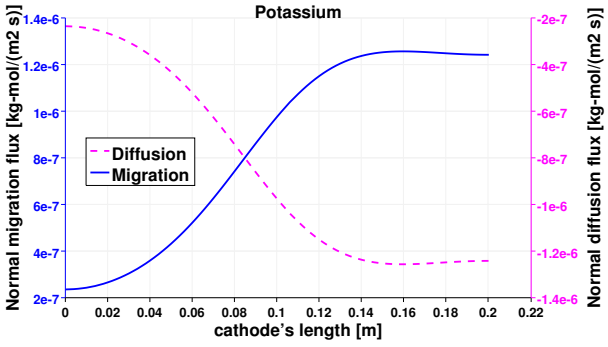

(c) Cathodic fluxes distributions

Figure 4.9 Normal components at the electrodes of the migration (blue) and diffusion fluxes (magenta) of K^+ (4.9a). Distributions of the same fluxes along the vertical anode (4.9b), and cathode (4.9c)

4.6 Conclusions

A mathematical model for an electrochemical cell is developed and solve numerically using the open-source CFD package *OpenFOAM*-2.3.1 to investigate the performances of a standard cell for the production of lithium in molten salts. Two predictor-corrector loops in series were used to first solve the fluid-dynamics equations and then the electrochemical equations. The electrochemical cell model takes into account the presence of the bubbles of chlorine released by the reaction at the anode and their effect on the flow of the liquid electrolyte. The upward movement of the gas due to their low density induces a natural convection on the electrolyte otherwise motionless. The flow becomes turbulent and a standard $k - \varepsilon$ model is applied for the liquid phase. The steady state of the electrolytic flow presents three main zones: a fast zone close to the anode moving upward, a clockwise re-circulation on the upper side of the cell, and a counterclockwise re-circulation at the bottom. The electrochemical part solves the conservation of charges accounting for ohmic

drop, concentration polarization, and also electrochemical kinetics. The distribution of current density along the anode shows a peak at the bottom corner of the anode. The same peak occurs on the electrolytic potential, the kinetic and the resistive overpotential. The latter reflects the presence of the film where the bubbles are mostly concentrated, reducing the overall conductivity of the electrolyte. The electrochemical aspect is validated by comparing the results of the present model to previously published studies [44]. The last part of this work focuses on the transport of ions and the results are presented in terms of fluxes. Results show that the normal migration flux cancels out the normal diffusion flux in presence of non-active species. In case of active species the two contributions are summing up. Indeed the total chloride flux at the anode is proportional to $\sim i_n/(n_{Cl^-}\ F)$, while the total lithium fluxes at the cathode to $\sim i_n/(n_{Li^+}\ F)$. In spite of this, the shape of all anodic fluxes report a similar trend to the current density, recalling the strong effect of the gaseous bubbles released by the oxidation of chloride. Analogously, the shape of all cathodic fluxes recalls the influence of the electrolytic flow with an inflection point located at $\sim 0.8\ m$ from the bottom of the cell, where the flow splits into two counter rotating zones.

4.6.1 Acknowledgments

A special thanks goes to the Canadian company *Hydro-Quebec*, and to the $NSERC$ which financially supported this study. The authors also thank the *Université de Sherbrooke* for its fellowship.

4.6.2 Nomenclature

Symbol	Units	Description
C_D	$-$	drag coefficient
$C_{\varepsilon,1}$	$-$	empirical turbulent constant
$C_{\varepsilon,2}$	$-$	empirical turbulent constant
Cl^-	$-$	chlorine ions
$Cl_{2,gas}$	$-$	chlorine gas
C_μ	$-$	empirical turbulent constant
Co	$-$	Courant number
C_s	$kg\text{-}mol/m^3$	concentration of the s_{th} species
$D_{s,eff}$	m^2/s	effective diffusion coefficient of the s_{th} species
$D_{s,mol}$	m^2/s	molecular diffusion coefficient of the s_{th} species
D_T	m^2/s	turbulent diffusion coefficient
d_{gas}	m	bubble's diameter
E	V	electric potential
E_{surf}	V	surface potential
E_{eq}^{∞}	V	equilibrium potential
F	$A\ s/kg\text{-}mol$	Faraday's constant
$\boldsymbol{F}_D$	$kg/(m^2\ s^2)$	drag force
$f_x(\cdot)$	$-$	function of $(\cdot)$
$\boldsymbol{g}$	m/s^2	gravity vector
$i_{0,a}$	A/m^2	anodic exchange current density

Table 4.4

Symbol	Units	Description
$i_{0,c}$	A/m^2	cathodic exchange current density
i_n	A/m^2	normal current density
j_n	m/s	specific normal mass flow rate
K^+	$-$	potassium ions
K_e	S/m	electrolyte conductivity
K_{gas}	S/m	gas conductivity
k	m^2/s^2	turbulent kinetic energy
Li^+	$-$	lithium ions
Li_{liq}	$-$	liquid lithium
l_{tls}	m	turbulent length scale
$\boldsymbol{M}_i$	m/s^2	interfacial momentum transfer of the i_{th} phase
M_{gas}	$kg/(kg\text{-}mol)$	molar mass of the gas phase
N_s	$kg\text{-}mol/(m^2\ s)$	flux of the s_{th} species
N_{tot}	$-$	total number of species in the solution
n_q	$-$	number of electrons involved in the q_{th} reaction
PIV	$-$	Particle Image Velocimeter
P_{prod}	m^2/s^3	turbulent kinetic energy production
p	Pa	pressure
R	$J/(kg\text{-}mol\ K)$	universal gas constant
$\boldsymbol{R}_i$	m^2/s^2	turbulent Reynold stresses of the i_{th} phase
Re_{rel}	$-$	relative Reynolds number
T	K	temperature
Ti	$-$	turbulent intensity

Table 4.5

Symbol	Units	Description
t	s	time
$\boldsymbol{U}_{gas}$	m/s	velocity vector of the gas phase
$\boldsymbol{U}_{i}$	m/s	velocity vector of the i_{th} phase
$\boldsymbol{U}_{liq}$	m/s	velocity vector of the liquid phase
$U_{n,gas}$	m/s	normal velocity component of the gas phase
u_{τ}	m/s	friction velocity, $\sqrt{\tau_w/\rho}$
wf	$-$	wall functions
Y_s	$-$	mole fraction of the s_{th} species
y	m	wall distance
z_s	$-$	charge number of the s-th species

Greek symbol	Units	Description
α_{gas}	$-$	volume fraction of the gas phase
α_i	$-$	volume fraction of the i_{th} phase
α_{liq}	$-$	volume fraction of the liquid phase
α_{sym}	$-$	symmetry coefficient
δ^+	$-$	non dimensional wall distance $=\delta\ u_{\tau}/\nu$
η	V	overpotential
ν_{eff}	m^2/s	effective kinematic viscosity
ν_{liq}	m^2/s	averaged liquid kinematic viscosity
ν_T	m^2/s	turbulent kinematic viscosity
ε	m^2/s^3	turbulent dissipation rate
ρ_{gas}	kg/m^3	density of the gas phase
ρ_i	kg/m^3	density of the i_{th} phase
σk	$-$	empirical turbulent constant
$\sigma\varepsilon$	$-$	empirical turbulent constant
τ_w	N/m^2	wall shear stress, $\mu(\partial_y U)\|_w$

Table 4.6

CHAPTER 5

CONCLUSIONS

5.1 Conclusions - Français

Un modèle mathématique a été implémenté avec succès en utilisant la librairie *OpenFOAM-2.3.1*, afin de nous permettre d'étudier avec beaucoup de liberté une grande gamme de systèmes électrochimiques et d'éviter d'avoir à effectuer des simplifications trop sévères. La modélisation numérique suit une architecture arborescente avec l'intention de rendre chaque branche facilement accessible. Le modèle mathématique est résolu en utilisant deux boucles consécutives prédicteur-correcteur qui résolvent en premier les équations de Navier-Stokes par l'algorithme *PISO* et en deuxième les équations associées au potentiel électrique (donc la densité de courant électrique) et le transport des ions par la convection, la migration et la diffusion. Le modèle a été initialement appliqué à une cellule rectangulaire de plaquage électrolytique du cuivre. Ce choix a été fait pour la simplicité, ce qui a permis de valider le squelette du modèle et en particulier de développer la méthode de solution associée aux conditions aux limites fortement couplées et non-linéaires que représentent les équations de Butler-Volmer. Le profil de densité de courant à l'électrode de travail a été correctement obtenu et présente un accord avec les résultats expérimentaux tirés de la littérature à l'intérieur d'une fourchette de 20%. Puisque les mesures expérimentales près des électrodes sont très difficiles, cet accord est satisfaisant. De plus, la solution numérique présente moins de 3% d'erreur par rapport à la solution analytique connue. On a inclus dans le modèle la modification des électrodes par la déposition et la corrosion en utilisant une approche de géométrie dynamique. Cet outil est important dans l'optique ou le modèle pourrait être utilisé afin de prédire la durée des électrodes et leurs cycles de remplacement, en plus de leur efficacité.

Après cette première étape de validation, un système géométriquement plus réaliste a été simulé en utilisant la géométrie de cellule $FM01\text{-}LC$, une copie de laboratoire de la géométrie industrielle répandue $FM21$. La présence de la zone de distribution d'entrée et de sortie de ces cellules est d'intérêt car elle montre la présence de 5 canaux différents ayant des vitesses et des débits différents. La présence des jets créés par ces canaux cause de la turbulence locale, ce qui rend la modélisation de la turbulence nécessaire.

Les résultats du modèle ont démontré la présence d'un écoulement préférentiel à la position de l'entrée la plus courte, court-circuitant en quelque sorte l'écoulement vers la sortie. On a trouvé que cet effet diminuait naturellement avec le nombre de Reynolds, en réduisant cependant la productivité de la cellule. Une meilleure uniformité de la déposition du cuivre a été obtenue en utilisant une cellule à ∇E_{cell} plus élevé, de sorte que la migration domine le transport des ions par rapport à la convection. Cependant les coûts d'opération associés à cette modification pourraient être un aspect qui limite son applicabilité, surtout en considérant l'utilisation de plusieurs réacteurs en série dans une configuration industrielle normale.

Afin d'appliquer le modèle à une cellule de production de lithium liquide dans des sels fondus, on a ajouté au modèle la possibilité d'écoulements multiphases gaz-liquide. L'oxydation du chlorure à l'anode produit en effet le dégagement de bulles de chlore qui ont un effet important sur le comportement fluido-dynamique et par conséquent réactif de la cellule. Les bulles dégagées à l'anode montent vers la surface et entraînent un mouvement de convection naturelle dans la cellule au sein de laquelle le fluide serait sans mouvement autrement. Le mouvement des bulles entraîne le liquide dans un mouvement qui devient turbulent. Pour simplifier l'analyse, la turbulence dans la phase gazeuse est négligée, ce qui est sans doute une approximation très raisonnable considérant la faible fraction volumique occupée par celle-ci. Afin de valider le modèle, la fraction de la surface de l'anode couverte par les bulles a été comparée à des résultats obtenus dans la littérature pour une cellule de magnésium et la comparaison qualitative est apparue adéquate. Étant donné le manque de mesures expérimentales disponibles dans la littérature scientifique disponible, le modèle a été validé partiellement en le comparant avec les résultats obtenus par un modèle mathématique ayant été publié récemment. La densité de courant, ainsi que le potentiel électrique et le surtension ont été comparés favorablement avec un cas de référence. Enfin, les résultats du transport des ions ont montré que la migration annulait la diffusion ordinaire en présence d'espèces non réactives, alors que dans le cas d'espèces réactives les deux contributions s'additionnent. De plus, la forme de tous les flux anodiques montre une forme similaire à celle de la densité de courant, soulignant ainsi le puissant effet de la présence des bulles dégagées à l'anode. De façon analogue, la forme des flux cathodiques montrait aussi l'influence de l'écoulement électrolytique avec un point d'inflexion correspondant à la position à laquelle l'écoulement se sépare en deux recirculations opposées.

En conclusion, le but de ce travail était de développer un modèle mathématique permettant de prédire les performances d'un procédé industriel électrolytique et d'exploiter la

modélisation mathématique avancée afin de permettre éventuellement de l'utiliser pour valider des nouveaux concepts de réacteurs électrochimiques.

5.2 Conclusions - English

A numerical model has been successfully implemented in *OpenFOAM-2.3.1* to freely investigate the performances of a wider range of electrochemical systems avoiding strong limiting simplifications. The modeling followed a tree architecture with the intent to maintain each branch easily accessible. The highly coupled system of equations is solved by means of two predictor-corrector loops. The first handles the fluid-dynamics, solving pressure and velocity through the *PISO* algorithm. The second deals with the electric potential, hence current density, and the transport of ions by means of convection, diffusion and migration. The initial model was applied to a rectangular cell performing copper electroplating. The cell was selected for its simplicity to validate the skeleton of the model and the non-linear Butler-Volmer boundary condition. The current density profile at the working electrode was correctly reproduced and met the experimental results within a 20% range. Knowing the difficulties in measuring the current density close to the electrode, the results were considered satisfactory, especially because supported by a 3% error band with the analytic solution. Geometry transformation of the reactor due to material deposition and corrosion are accounted with a moving mesh. This tool becomes important to estimate the replacement time of the electrodes, the system life-time, and its efficiency.

Once the basic solver was proven right, a similar system of equation was applied to a more complicated geometry. The laboratory scale $FM01\text{-}LC$ cell was chosen because of its entrance and exit manifolds. They provide the reactive channel with a plug flow having five different entrance velocities. Their presence caused the dilute electrolytic solution to be in a turbulent regime, forcing the implementation of a turbulent model. By doing so, the new flow patterns presented a favorite path in correspondence of the shortest entrance jet, causing a counter sinking effect at the exit. Fluid-dynamics results indicated that at low Re these effects are obviously attenuated at the expenses of a lower production rate. A more uniform molar fraction of copper was achieved by using a high ∇E_{cell}, so that the migration mechanism dominated the transport of ions with respect to the convection phenomena. The drawbacks counts higher operative costs, specially considering the industrial scale and the packing of multiple reactors in series.

An additional level of complexity was brought to the solver when it was applied to a cylindrical standard cell for the production of lithium in molten salt. The structure of

the solver was maintained, but the anodic oxidation of chloride releasing gas, imposed the modeling of a two-phase electrolytic flow. The bubbles freed at the anode, due to their low density tended to move upward, dragging with them the nearby liquid flow otherwise motionless. The electrolyte started to get eddy-populated and a turbulent model was required to model the concentrated solution. No turbulence was considered for the gas phase, due to its low volume fraction. To validate the model the bubbles coverage at the anode was overlapped to a PIV image of a magnesium cell with a similar behavior, and the comparison was found adequate. Due to the lack of measurements data, the electrochemical aspect was proven right by a previously validate and published model. Current density, alongside with the liquid electric potential, the kinetic overpotential, and the overpotential of the bubbly resistive layer matched with the reference test case. Last but not least, results on the transport of ions, showed that the normal migration flux canceled out the normal diffusion flux in presence of non-active species, while in case of active species the two contributions were summing up. Additionally the shape of all anodic fluxes reported a trend similar to the current density, recalling the strong effect of the gaseous bubbles released by the oxidation of chloride. Analogously, the shape of all cathodic fluxes recalled the influence of the electrolytic flow with an inflection point in correspondence of a location where the flow splits into two counter rotating zones.

To conclude, the aim of this work to create an open source platform to predict and analyze industrial reactor's performances is achieved. The advanced modeling is exploited and ready to be used as a validation instrument for new electrochemical concepts.

5.2.1 Future perspective

Thanks to the structure of the solver POTiso, future developments will be easier to integrate to the already validated model. Indeed, the solver could be further expanded by adding a population balance modeling. The use of non constant bubble diameters will help describing the evolution of a population of particles, through a set of integro-partial differential equations, where particulate systems will be characterized by the birth and death of particle. This can eventually rise issues that will have to be investigated such as the contribution of other interfacial forces not negligible anymore, i.e. the force due to virtual mass and the lift. As a consequence the turbulence will probably become important for both the two phases, requiring a turbulence modeling also for the gas phase, and few extra coupling terms depending on the turbulence models selected. At this point it will be wise to use a better approximation for the turbulent Schmidt number, for instance the Kays Crawford modeling, and it will become crucial to get the right concentration's

distribution in the near electrode regions, by implementing a set of wall functions. For the latter ones, a Launder-Spalding distribution adapted to mass transfer could be an appropriate choice. Furthermore, in order to have an even current density distribution along the active plates, couple of turbulent promoters could be added in the bulk of new cells' design concepts. Preliminary studies on this subject made by the author determined that multiple cross sections of fractal grids may represent a good solution. In conclusion, thanks to the accessibility of the open source code, and its flexible structure, this solver can be modified according to the research needs. It can be used as a tool to predict and vallidate the performance of an electrochemical reactor since the lack of data represents a strong obstacle for this research.

ANNEX A

This appendix shows the structure of the solver at its final status.

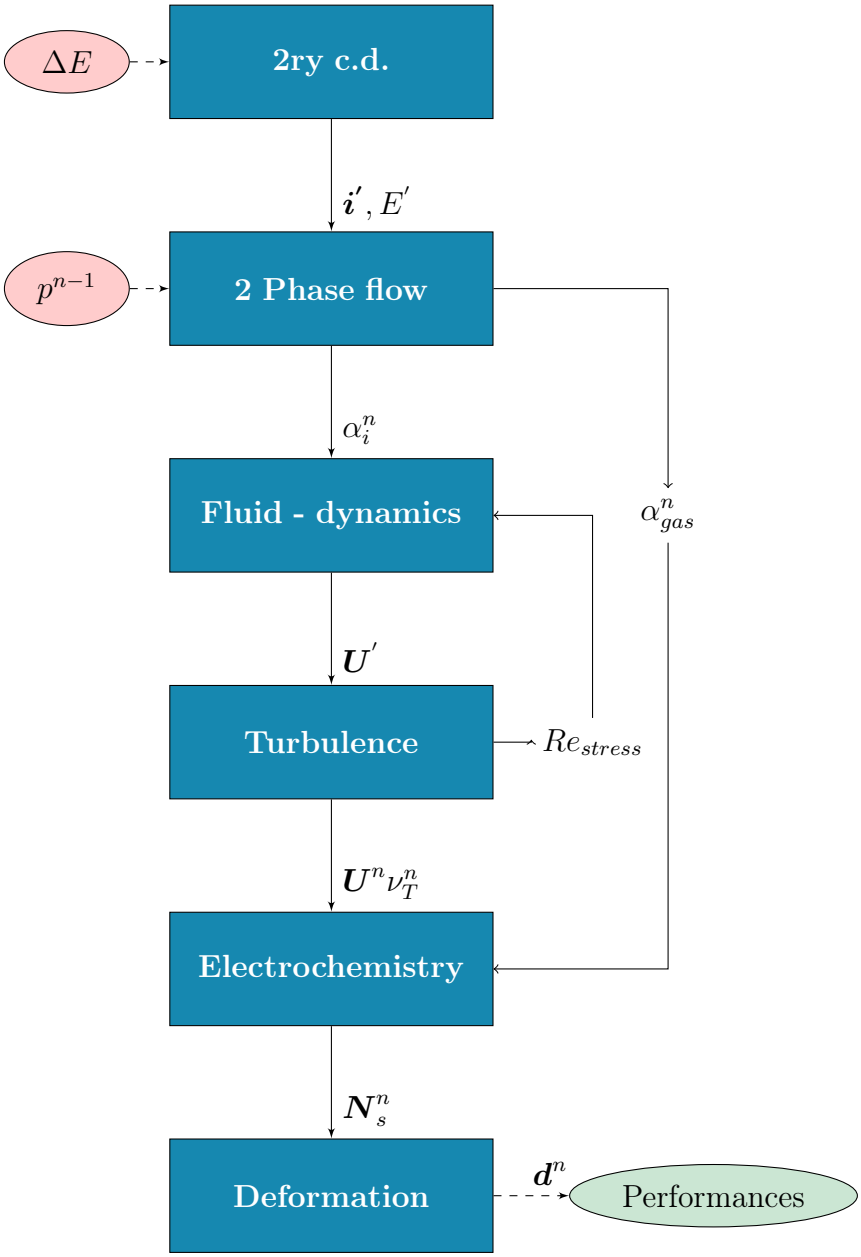

More in details, the structure of the solver reveals the strong coupling among the blocks.

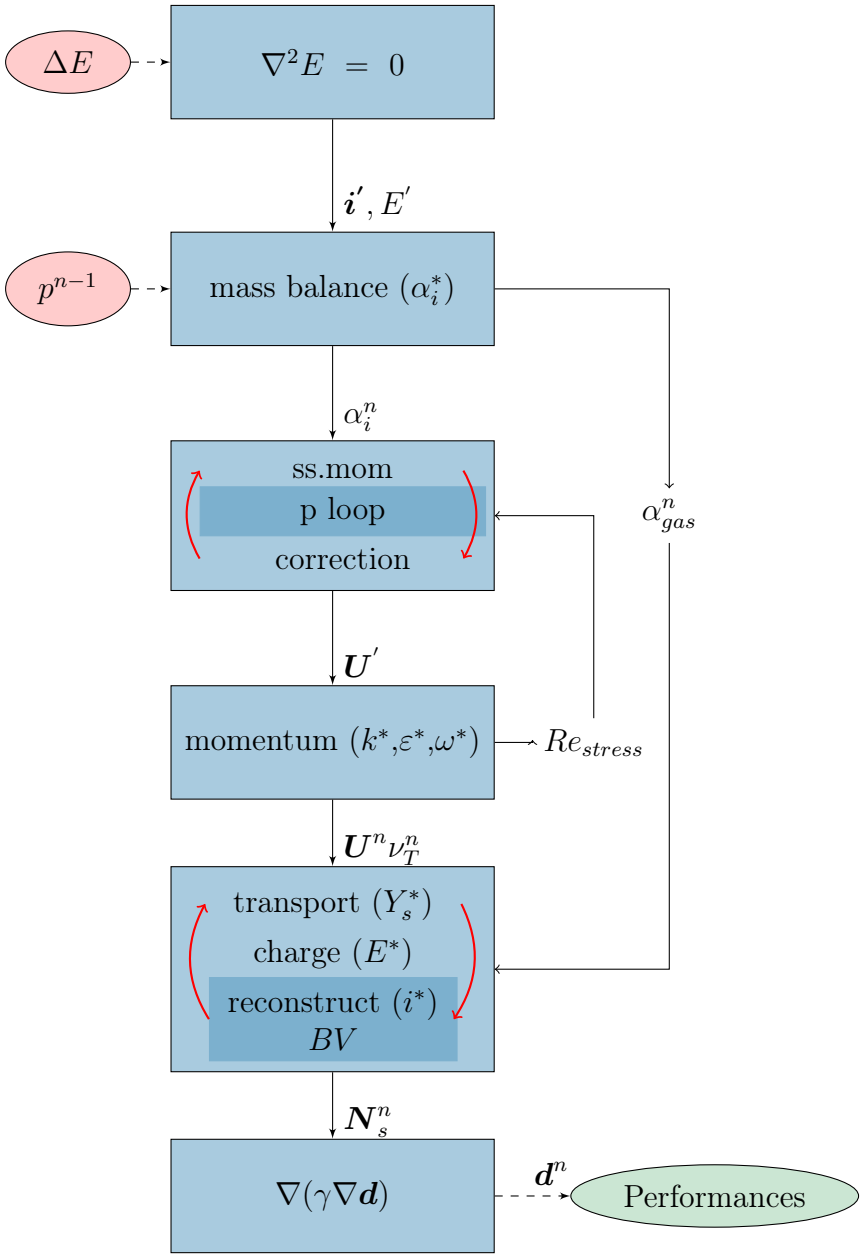

LIST OF REFERENCES

[1] Aldas, K., Pehlivanoglu, N. and Mat, M. (2013). Numerical and experimental investigation of two-phase flow in an electrochemical cell. *International Journal of Hydrogen Energy*, volume 48, pp. 32 – 45.

[2] Alexiadis, A., Dudukovic, M., Ramachandran, P., Cornell, A., Wanngard, J. and Bokkers, A. (2011). Liquid-gas flow patterns in a narrow electrochemical channel. *Chemical Engineering Science 66*, volume 66, pp. 2252–2260.

[3] Amendola, S., Swonger, L. and Goldman, S. (Accessed 08-27-2017). Electrolytic production of lithium metal. US Patent 13/172, 401 online at `http://www.google.com/patents/US20120006690`.

[4] ANSYS, I. (2011). Fluent theory guide. *14.0 edition*.

[5] Bard, A. and Faulkner, L. (2001). *Electrochemical Methods. Fundamentals and applications*, 2nd edition. John Wiley & Sons, Inc., Hoboken - New Jersey.

[6] Boussinesq, J. (1877). Essai sur le théorie des eaux courantes. *Mémoires présentés par divers savants à l'Académie des Sciences*, volume 23, pp. 1–680.

[7] Brown, C., Pletcher, D. and Walsh, F. (1992). Local mass transport in the fm01 laboratory electrolyser. *J. Appl. Electrochem.*, volume 22, pp. 811–823.

[8] Butrón, E., Juárez, M., Solís, M., Teutli, M., González, I. and Nava, J. (2007). Electrochemical incineration of indigo textile dye in filter-press-type fm01-lc electrochemical cell using bdd electrodes. *Electrochim. Acta*, volume 52, pp. 6888–6894.

[9] CFD-Direct (2016). Openfoam.

[10] Clift, R., Grace, J. R. and Weber, M. E. (1978). Bubbles, drops, and particles. *ACADEMIC PRESS, New York-San Francisco-London*.

[11] DeYoung, D. (Accessed 08-27-2017). Production of lithium by direct electrolysis of lithium carbonate. US Patent 4, 988, 417 online at `https://www.google.com/patents/US4988417`.

[12] Ferziger, J. and Peric, M. (2002). *Computational Methods for Fluid Dynamics*, 3rd edition. Springer-Verlag.

[13] Frías-Ferrer, A., González-García, J., Sáez, V., Ponce de Léon, C. and F.C., W. (2008). The effects of the manifold flow on mass transport in electrochemical filter-press reactors. *AIChE Journal*, volume 54, pp. 811–823.

[14] Georgiadou, M. (1197). Finite-difference simulation of multi-ion elecfrochemical systems governed by diffusion, migration, and convection. *J. Electrochem. Soc.*, volume 148, pp. 2732–2739.

[15] Georgiadou, M. (2003). Modeling current density distribution in electrochemical systems. *Electrochemica Acta*, volume 48, pp. 4089–4095.

[16] Gerth, L. (1995). *Electrodéposition de cuivre à partir de solutions sulfuriques; mesures locales de la densité de courant dans des cellules à hydrodynamique complexe*. Ph.D. thesis, Ecole Nationale Polytechnique de Loraine, Nancy - France.

[17] Holzinger, G. (2015). Openfoam a little user-manual. *CD-Laboratory - Particulate Flow Modelling Johannes Keplper University, Linz, Austria*.

[18] Huerta Garrido, M. and Pritzker, M. (2006). Eis and statistical analysis of copper electrodeposition accounting for multi-component transport and reactions. *Journal of Electroanalytical Chemistry*, volume 594, pp. 118–132.

[19] Huerta Garrido, M. and Pritzker, M. (2008). Reply to "remarks on " eis and statistical analysis of copper electrodeposition accounting for multi-component transport and reactions" [m.e. huerta garrido, m.d. pritzker, j. electroanal. chem. 594 (2006) 118]" by a. lasia. *Journal of Electroanalytical Chemistry*, volume 619, pp. 183–186.

[20] INEOS (Accessed 01-03-2016). Technologies enterprise: Chlorine technology. Available at `http://www.ineos.com/businesses/ineos-technologies/technologies/`.

[21] Issa, R. (1985). Solution of the implicitly discretized fluid flow equations by operator-splitting. *Journal of Computational Physics*, volume 62, pp. 40–65.

[22] Issa, R., Gosman, A. and Watkins, A. (1986). The computation of compressible and incompressible recirculating flow by a non-iterative implicit scheme. *Journal of Computational Physics*, volume 62, pp. 66–82.

[23] Jasak, H. (1996). *Error Analysis and Estimation for the Finite Volume Method with Applications to Fluid Flow*. Ph.D. thesis, Imperial College of Science, Technology, and Medicine, Department of Mechanical Engineering.

[24] Kruesi, W. H. and Fray, D. J. (1994). Fundamental study of the anodic and cathodic reactions during the electrolysis of a lithium carbonate-lithium chloride melt using a carbon anode. *Journal of Applied Electrochemistry*, volume 24, number 11, pp. 1102–1108.

[25] Lasia, A. (2007). Remarks on "eis and statistical analysis of copper electrodeposition accounting for multi-component transport and reactions" [m.e. huerta garrido, m.d. pritzker, j. electroanal. chem. 594 (2006) 118]. *Chemical Engineering Research and Design*, volume 605, pp. 77–79.

[26] Launder, B. E. and Sharma, B. I. (1974). Application of the energy dissipation model of turbulence to the calculation of flow near a spinning disc. *Letters in Heat and Mass Transfer*, volume 1, pp. 131–138.

[27] Lesieur, M. (2008). Turbulence in fluids, 4th edition. *Springer*.

[28] Libby, P. A. (1996). Introduction to turbulence. *Taylor and Francis*.

[29] Litrico, G., Vieira, C. B., Askari, E. and Proulx, P. (2017). Strongly coupled model for the prediction of the performances of an electrochemical reactor. *Chemical Engineering Science*, volume 170, pp. 767–776.

[30] Liu, C. L., Lu, G. M., Song, X. F. and Yu, J. G. (2015). Experimental and numerical investigation of two-phase flow patterns in magnesium electrolysis cell with non-uniform current density distribution. *The Canadian Journal of Chemical Engineering*, volume 93, pp. 565–579.

[31] López, O., González, I. and Nava, J. (2008). Electrochemical inceneration of indigo textile dye in filter-press-type fm01-lc electrochemical cell using mesh-dsa anode. *ECS Transactions*, volume 15, pp. 395–402.

[32] Mathieu, J. and Scott, J. (2000). An introduction to turbulent flow. *Cambridge University Press*.

[33] McCormick, E. S., Reddy, S. S. and Sintim-Damoa, K. (1984). Electrolytic production of lithium metal. *U.S. patent 4455202*.

[34] Menter, F. R. (1993). Zonal two equation k-omega turbulence models for aerodynamic flows. In *24th AIAA Fluid Dynamics Conference*. AERODYNAMICS, pp. 1–21.

[35] Menter, F. R. (1994). Two-equation eddy-viscosity turbulence models for engineering applications applications. *AIAA Journal*, volume 32, pp. 1598–1605.

[36] Menter, F. R. and Esch, T. (2001). Elements of industrial heat transfer prediction. In *16th Brazilian Congress Of Mechanical Engineering*, COBEM. Invited Lectures, pp. 117–127.

[37] Menter, F. R., Kuntz, M. and Langtry, R. (2003). *Ten Years of Industrial Experience with the SST Turbulence Model*, 4th edition. Begell House, Inc.

[38] Miao, X., Lucas, D., Ren, Z., Eckert, S. and Gerbeth, G. (2008). Numerical modeling of bubble-driven liquid metal flows with external static magnetic field. *International Journal of Multiphase Flow*, volume 33, pp. 3668–3675.

[39] MIT (Accessed 09-15-2016). Chapter 7: Basics of turbulent flows. Online course at `http://www.mit.edu/course/1/1.061/OldFiles/www/dream/SEVEN/SEVENTHEORY.PDF`.

[40] Nava, J., Butrón, E. and González, I. (2008). Importance of hydrodynamic conditions on the electrochemical incineration of cresols, indigo textile dye and vinasses present in industrial wastewater using a filter-press-type fm01-lc reactor with bdd electrodes. *J. Environ. Eng. Manage.*, volume 18, pp. 221–230.

[41] Nava, J., Núnez, F. and González, I. (2007). Electrochemical incineration of p-cresol and o-cresol in the filter-press-type fm01-lc electrochemical cell using bdd electrodes in sulfate media at ph 0. *Electrochim. Acta*, volume 52, pp. 3229–3235.

[42] Newman, J. and E., T.-A. K. (2004). Electrochemical systems, third edition. *John Wiley and Sons*, volume New Jersey.

[43] Nguyen, T., Walton, C. and R.E., W. (1986). Parallel-plate electrochemical reactor model: A methode for determining the time-dependent behaviour and the effects of axial diffusion and axial migration. *J. Electrochem. Soc: Electrochemical science and technology*, volume 133, pp. 81–87.

[44] Oliaii, E., Désilets, M. and Lantagne, G. (2017). Numerical analysis of the effect of structural and operational parameters on electric and concentration fields of a lithium electrolysis cell. *J.of Appl. Electrochem.*, volume 47, pp. 711–726.

[45] Oliveira, P. and Issa, R. (2001). An improved piso algorithm for the computation of buoyancy-driven flows. *Numerical Heat Transfer*, volume 40, pp. 473–493.

[46] OpenFOAM (2014). The open source cfd toolbox. *User Guide*.

[47] Pope, S. (2000). *Turbulent Flows*. Cambridge University Press, Lancaster, New Jersey.

[48] Pope, S. B. (2004). Ten questions concerning the large-eddy simulation of turbulent flows. *New Journal of Physics*, volume 6, pp. 1–24.

[49] Press, W., Teukolsky, S., Vetterlings, W. and Flannery, B. (2007). *Numerical Recipes in C. The art of Scientific Computing*, 3rd edition. Cambridge University Press.

[50] Reddy, T. B. and Linden, D. (2011). *Linden's Handbook of Batteries, fourth edition*, 4th edition. Mc Graw Hill.

[51] Richardson, L. (1911). The approximate arithmetical solution by finite differences of physical problems involving differential equations, with an application to the stresses in a masonry dam. *Philosophical Transactions of the royal society A, Mathematical, Physical and Engineering Sciences*, volume 210, pp. 307–357.

[52] Rivera, F., Ponce de León, C., Nava, J. and Walsh, F. (2015). The filter-press fm01-lc laboratory flow reactor and its applications. *Electrochimica Acta*, volume 163, pp. 338–354.

[53] Rivero, E., Cruz-Díaz, M. and Almazán-Ruiz, F. (2015). Modeling the effect of non-ideal flow pattern on tertiary current distribution in a filter-press-type electrochemical reactor for copper recovery. *Chemical Engineering Research and Design*, volume 100, pp. 422–433.

[54] Rivero, E., Gonzalez, I., Rivera, F. and Cruz-Díaz, M. (2010). Analysis and implementation of residence time distribution experimental curve in fm01-lc reactor using axial dispersion and plug dispersion exchange models with closed-closed boundary conditions. *Electrochimica Acta*, volume 56, pp. 361–371.

[55] Roache, P. (1998). *Verification and Validation in Computational Science and Engineering*. Hermosa Publishers, Albuquerque - New Mexico.

[56] Robinson, D. (1991). *Electrosynthesis from Laboratory, To Pilot, To Production*. The Electrosynthesis C. Inc, Lancaster, New Jersey.

[57] Rosales, M. and Nava, J. (2017). Simulations of turbulent flow, mass transport, and tertiary current distribution on the cathode of a rotating cylinder electrode reactor in

continuous operation mode during silver deposition. *Journal of The Electrochemical Society*, volume 164, pp. 3345–3353.

[58] Rusche, H. (2002). *Computational fluid dynamics of dispersed two-phase flows at high phase fractions*. PhD Thesis. Imperial College of Science, Technology and Medicine.

[59] Schiller, L. and Naumaan, Z. (1935). A drag coefficient correlation. *V.D.I Zeitung*, volume 77, p. 138.

[60] Schlichting, H. and Gersten, K. (2017). Boundary-layer theory, 9th edition. *Springer*.

[61] Slater, J. (Accessed 04-20-2015). Examining spatial (grid) convergence. Available at `http://www.grc.nasa.gov/WWW/wind/valid/tutorial/spatconv.html`.

[62] Tennekes, H. and Lumley., J. L. (1999). A first course in turbulence. *Massachusetts Institute of Technology*.

[63] Trinidad, P. and Walsh, F. (1996). Hydrodynamic behavior of the fm01-lc reactor. *Electrochimica Acta*, volume 41, pp. 493–502.

[64] Versteeg, H. K. and Malalasekera, W. (2007). *An introduction to Computational Fluid Dynamics, the finite volume method, 2*. Pearson Education Limited, Harlow, England.

[65] Vogt, H. and Balzer, R. J. (2005). The bubble coverage of gas-evolving electrodes in stagnant electrolytes. *Electrochimica Acta*, volume 50, pp. 2073–2079.

[66] Walsh, F. (1993). A first course in electrochemica engineering. *The Electrochemical Consultancy*.

[67] Walsh, F., Griffiths, M. and Ponce de Léon, C. (2005). Mass transport in the rectangular channel of a filter-press electrolyzer (the fm01-lc reactor). *American Institute of Chemical Engineers Journal*, volume 51, pp. 682–687.

[68] Walsh, F. and Robinson, D. (1998). Electrochemical filter-press reactor technology designed for versatility and efficiency. *Electrochem. Soc. Interface*, volume 7, p. 40.

[69] Walsh, F. and Trinidad, P. (1999). Batch oxidation of cerous ions in a divided fm01-lc filter-press reacto. In *Institution of Chemical Engineerng Symposium Series*, Electrochemical Engineering 5, ICHEME. Number 145, pp. 281–289.

[70] White, R., Boin, M. and Raible, M. (1983). *Parallel Plate Electrochemical Reactor Model* (Technical report). University of South Carolina, Chemical Engineering Department.

[71] Wilcox, D. (1993). *Turbulence Modeling for CFD*. DCW Industries, Inc., La Canada, United States.

[72] Wilke, C. R. and Fairbanks, D. F. (1950). Diffusion coefficients in multicomponent gas mixtures. *Industrial and engineering chemistry*, volume 42, pp. 471–475.

[73] Wu, B.-H., Wan, C.-C. and Wang, Y.-Y. (2003). Modeling of acid copper anisotropic deposition based on detailed calculation of the electrolyte composition. *Journal of The Electrochemical Society*, volume 150, pp. C7–C15.

[74] Zhiyin, Y. (2015). Large-eddy simulation: Past, present and the future. *Chinese Journal of Aeronautics*, volume 28, pp. 11–24.